DEVELOPING POPULATION-SPECIFIC BRAIN ATLASES AND

MONITORING REPETITIVE HEAD IMPACTS FOR

EARLY-TO-MIDDLE ADOLESCENT COLLISION-SPORT ATHLETES

A Dissertation

Submitted to the Faculty

of

Purdue University

by

Yukai Zou

In Partial Fulfillment of the

Requirements for the Degree

of

Doctor of Philosophy

August 2020

Purdue University

West Lafayette, Indiana

THE PURDUE UNIVERSITY GRADUATE SCHOOL
STATEMENT OF DISSERTATION APPROVAL

Dr. Joseph V. Rispoli, Chair
      Weldon School of Biomedical Engineering
Dr. Riyi Shi
      Department of Basic Medical Sciences
Dr. Thomas M. Talavage
      Weldon School of Biomedical Engineering
Dr. Yunjie Tong
      Weldon School of Biomedical Engineering

Approved by:
      Dr. George R. Wodicka
         Dane A. Miller Head of the Weldon School of Biomedical Engineering

To my parents

ACKNOWLEDGMENTS

TABLE OF CONTENTS

LIST OF TABLES

LIST OF FIGURES

ABBREVIATIONS

AD	Axial diffusivity
ADC	Apparent diffusion coefficient
ABCD	Adolescent Brain Cognitive Development
ADHD	Attention-deficit/hyperactivity disorder
CT	Computed tomography
ComBat	Combined association test
ConvNets	Convolutional neural networks
CovBat	Correcting covariance batch effects
DBM	Deformation-based morphometry
DKE	Diffusion kurtosis estimator
DKI	Diffusion kurtosis imaging
DTI	Diffusion tensor imaging
DWI	Diffusion-weighted imaging
EMA	Early-to-Middle adolescent
FA	Fractional anisotropy
fMRI	Functional magnetic resonance imaging
GAM	Generalized Additive Model
HAE	Head acceleration event
MD	Mean diffusivity
MNI	Montreal Neurological Institute
MRI	Magnetic resonance imaging
MRS	Magnetic resonance spectroscopy
mTBI	Mild traumatic brain injury
NF	Neurofilament
OSG	Open Science Grid
PNG	Purdue Neurotrauma Group
PTA	Peak Translational Acceleration
RD	Radial diffusivity
RF	Radiofrequency
ROI	Region-of-interest
RISH	Rotation invariant spherical harmonics
RTISD	Reaction time individual standard deviation
SHM	Structural health monitoring
TBI	Traumatic brain injury
TBSS	Tract-based spatial statistics
TE	Echo time
YoE	Years of high-school experience
WM	White matter

ABSTRACT

Adolescent collision-sport athletes may be exposed to repetitive head impacts over years of practices and competitions without immediately observable symptoms. Despite the growing concerns, these athletes often continue play while at risk. Concrete objective measurements are desired to inform prompt and effective preventative strategies for this vulnerable population. However, adolescent brains are rapidly developing and the accrual of brain injury is often subtle. Prospective screening with sensitive biomarkers is challenging and requires advanced technologies, rigorous data processing, and the interdisciplinary expertise of engineering, neurobiology, and cognitive sciences.

To address the challenge, we first developed population-specific brain atlases to facilitate reproducible and meaningful statistical analyses. The atlases better characterized the neuroanatomy of early-to-middle adolescent (ages 13-19) collision-sport athletes, reduced deformation introduced during spatial normalization, and exhibited higher sensitivity in image analysis compared to standardized adult or age-appropriate brain templates. The atlases can be further applied to monitor the neuroanatomical trajectory and can serve as a coordinate reference system to retrospectively harmonize data collected from different sites and imaging acquisition parameters, facilitating group analysis at large scale.

Next, to assess whether the changes of white matter microstructure can be attributed to repetitive head impacts and are reflected by cognitive performance, we analysed the diffusion tensor imaging (DTI) data of high school mens football and women's soccer across a single season, with accompanying data from head impact sensors and neurocognitive assessments. Within multiple brain regions, we observed significantly altered DTI metrics, both transiently over a season and chronically with more years of high school experience. For the football players, hits with peak translational acceleration over 37 g were sufficient to alter the distributions of DTI changes, and deficits in white matter microstructure correlated with poorer performance of anti-saccade task at one month post-season, suggesting increased vulnerability for inhibitory control. Monitoring repetitive head impacts thus provides a temporal profile for identifying at-risk individuals during the competitive season, informing prompt interventional strategies, therefore protecting the brain and cognitive health of early-to-middle adolescent collision-sport athletes in the long run.

1. INTRODUCTION

1.1 Mild Traumatic Brain Injury

Traumatic brain injury (TBI) is a public health challenge and a leading factor of disability and death around the world [1,2]. According to Glasgow Coma Scale [3], TBI can be divided into mild ($\geq$13), moderate (9-12), severe (3-8), and vegetative ($<$3) states. About 80 percent of all treated TBIs are mild [4,5]. In the United States, the reported incidence of mTBI is around 500/100,000 [6], notwithstanding many milder and untreated brain injuries were not counted [7,8]. The term "mild" does not imply that the impacts of mTBI are mild on the costs of economy, health care resources, and societal productivity [1]; greater efforts must be warranted among scientists, engineers, and clinicians to perform high-quality research, develop protective and preventive approaches, and provide prompt diagnosis and interventions. We ignore mTBI at our peril.

This thesis concerns mTBI in adolescent athletes who participate in collision sports (American football and soccer), a population vulnerable to brain injury [9, 10]. In this section, two population-specific risks of mTBI will be introduced, namely concussion and subconcussive trauma due to repetitive head impacts. Potential fluidic and imaging-based biomarkers of mTBI will also be described.

Concussion and Subconcussive Trauma

Concussion is a biomechanically induced brain injury [11] and is interchangably referred to mTBI in the sports literature [12]. In the United States, there are about 3,800,000 cases of sport related concussion (or severer forms of TBI) every year [8,13]. Adolescent athletes bear a higher rate of head injury and prolonged recovery than the adults [9, 14]; from 2005 to 2010, over 700,000 cases of concussions were reported for high school athletes, and the true number of injuries may be underreported [15–19].

According to the consensus statement at the 5th International Conference on Concussion in Sport [20], the following features may be employed to clinically define sport related concussion:

- "Sport related concussion may be caused either by a direct blow to the head, face, neck or elsewhere on the body with an impulsive force transmitted to the head."

- "Sport related concussion typically results in the rapid onset of short-lived impairment of neurological function that resolves spontaneously. However, in some cases, signs and symptoms evolve over a number of minutes to hours."

- "Sport related concussion may result in neuropathological changes, but the acute clinical signs and symptoms largely reflect a functional disturbance rather than a structural injury and, as such, no abnormality is seen on standard structural neuroimaging studies."

- "Sport related concussion results in a range of clinical signs and symptoms that may or may not involve loss of consciousness. Resolution of the clinical and cognitive features typically follows a sequential course. However, in some cases symptoms may be prolonged."

In general, the majority of the symptoms of concussion usually resolve within two to seven days [21], and all the symptoms can fully resolve within three months post injury. According to *International Statistical Classification of Disease and Related Health Problems, 10th Revision* (ICD-10) [22], postconcussion syndrome "occurs following head trauma (usually sufficiently severe to result in loss of consciousness)," and "there must be at least 3 symptoms present for more than 4 weeks after injury to be diagnosed as postconcussion syndrome, which include headache, dizziness, fatigue, irritability, difficulty in concentration and performing mental tasks, impairment of memory, insomnia, and reduced tolerance to stress, emotional excitement, or alcohol. Additional symptoms of postconcussion syndrome involve anxiety, depression, fatigue, nausea, balance abnormalities, disturbances in vision and sleep, and hypersensitivity to light and noise [21,23–25]. In addition, a period of "physiological vulnerability" may present after the clinical symptoms are resolved, but currently the return-to-play decision is still largely based on clinical recovery and lacks evidence from physiology [26].

However, there has been long debate over diagnosis of postconcussion syndrome [1], mainly due to the diverse and nonspecific nature of the symptoms of concussion. ICD-10 failed to accurately classify mTBI patients potentially having prolonged postconcussion syndrome [27] and is biased reflecting the true incidence rate [1]. Considering the nonspecificity of the symptoms and the large discrepancies in the clinical community, *Diagnostic and Statistical Manual of Mental Disorders* (DSM-V) has dropped the diagnostic criteria and added a category "Major or Mild Neurocognitive Disorder due to Traumatic Brain Injury" [28]. According to DSM-V, "neurocognitive symptoms associated with mTBI are noted to resolve within days to weeks after the injury with complete resolution by three months."

Trauma can evolve from the accumulation of repetitive head impacts, a.k.a. head acceleration events (HAEs) [29,30], and this is a critical aspect often ignored in collision sports due to several reasons. First, a single HAE would not necessarily induce injury or immediate symptoms of concussion [31,32]. Second, "risk compensation [33] of wearing helmet. Athletes may believe helmets can sufficiently keep them from getting injured, and therefore hit more aggressively; since the introduction of more protective helmets in American football in 1959, the use of the head as primary contact was increased [29,33,34]. Third, false-negative outcomes from conventional neuroimaging. To detect potential structural injury (e.g. hemorrhagic lesions) that requires neurosurgical intervention, a Computed Tomography (CT) scan of head is typically performed in the emergency management of mTBI; however, CT has poor sensitivity in detecting underlying abnormalities associated with milder forms of brain injury [1].

Fluidic and Imaging-based Biomarkers

Biomarker is "a characteristic that is objectively measured and evaluated as an indicator of normal biological processes, pathogenic processes, or pharmacological responses to a therapeutic intervention [35]." Potential biomarkers for mTBI are divided into two categories: fluidic (i.e. from blood or cerebrospinal fluid) [36] and imaging-based [37]. Both categories of biomarkers will be covered in this section, but later chapters of the thesis will focus exclusively on imaging-based biomarkers.

The complex interplays among the physical, biological, and physiological underpinnings of mTBI provide a rich pool for identifying potential biomarkers. A thorough review of the mechanisms can be found in [38] and [39]. First, primary injury in neuronal cells occurs in the form of mechanical damages, including axonal stretching, swelling, and irreversible disconnection [40, 41]. Usually, immediate primary injury is not observed from single subconcussive HAE. Secondary injury occurs after the mechanical damages, which involves neurometabolic cascades such as microglial activation, neuroinflammation, and release of free radicals [39, 42]; contrary to primary injury, secondary injury is non-mechanical and often lasts from several days to months. Secondary injury also provides potential targets, such as proteins, microRNAs, and nucleic acids, for developing fluidic biomarkers [43].

Many candidate fluidic biomarkers have been identified in acute ($\leq$ hours) and severer forms of TBI. Examples include 1) *Glial fibrillary acidic protein*, which reflects astrocytosis and axonal injury [44–46]; 2) *UCH-L1* (a ubiquitin carboxyl-terminal hydrolase), which indicates neuronal cell damage [45–47]; 3) *S100B* (a calcium-binding protein in astrocyte), whose increase indicates activation of inflammatory response [48]; 4) *Myelin basic protein*, whose proteolysis occurs following neurotrauma [49]; 5) *Neurofilament (NF)*, in which the NF-heavy and NF-light proteins demonstrated potentials to link head impacts with axonal injury and early neurodegeneration [50–53]; 6) *Tau* (an axonal structural protein), in which the levels of phosphorylated and total proteins may be used to diagnose mTBI [54, 55].

Evidence for the diagnostic potentials and clinical utilities of candidate fluidic biomarkers was still limited [43, 56]. For instance, one study did not suggest glial fibrillary acidic protein and UCH-L1 were specific for distinguishing mTBI that were CT-negative [57]. Combining multiple fluidic biomarkers present a promising methodology that leverages the strengths of single biomarker; a proof of concept analysis of the TRACK-TBI Pilot study integrated a multivariate proteomic panel as an "ensembled biomarker" for TBI [58], and a recent study from the NCAA-DoD CARE Consortium has shown slight (but not significant) improvement in diagnostic certainty for acute sport related concussion [46].

On the other hand, the advancement of different neuroimaging modalities has enabled progresses in searching imaging-based biomarkers for concussion and/or subconcussive trauma, which is previously not possible with conventional approaches. Back in 2008, McCrea [1] summarized the findings in mTBI with regard to different imaging modalities, ranging from conventional approaches such as CT, structural MRI, magnetic resonance spectroscopy (MRS), all the way to the more advanced diffusion tensor imaging (DTI) and blood-oxygen-level dependent (BOLD) functional MRI (fMRI) at that time. Over the past decade, many imaging-based biomarkers have been proposed [37], quantifying 1) white matter microstructure, such as fractional anisotropy and mean diffusivity from DTI [59–61]; 2) neurometabolic alterations, including choline, N-acetyl aspartate, and glutamate/glutamine from MRS [60, 62, 63]; 3) functional connectivity, based on correlations of BOLD time series

from fMRI [64, 65]; 4) Cerebral blood flow, estimated from arterial spin labeling, a non-invasive perfusion MRI technique [66]. Potential biomarkers from other MRI techniques or imaging modalities are summarized in [37].

Ideally, a biomarker of mTBI should be:

1) sensitive to neurobiological changes resulted from the head injury and the treatment;

2) reproducible with minimal adverse impacts from adjustments in, e.g., acquisition and/or processing;

3) easily assessed with minimal discomfort introduced to the subjects.

To date, a sensitive and reliable biomarker for concussion or subconcussive trauma is not available. As an objective probe for diagnosis and measuring recovery, biomarker fails to bring benefits when the target population do not get the healthcare services that they should. It is of equal importance to make biomarkers available and accessible. Fluidic biomarkers, upon successful validation, are easily accessible in a clinical setting, and are more likely to be covered by healthcare insurance provider than imaging-based biomarkers. However, although largely serve as research tools, imaging-based biomarkers have great potential to provide scientific evidences that raise awareness among the general public, drive technological development (e.g. protective equipment), and guide preventative strategies that require minimal or even no cost to implement.

1.2 Structural Health Monitoring Framework

To tackle the challenge of prospective screening with sensitive biomarkers, this thesis has a central theme: **we constantly demand advanced technologies that reveal new insights of brain, rigorous processing pipelines for the acquired data, and the interdisciplinary expertise of engineering, neurobiology, and cognitive sciences.** This section will present the interdisciplinary framework of Purdue Neurotrauma Group (PNG), which is essentially an engineering solution that integrate techniques from three disciplines to monitor brain health of adolescent collision-sport athletes.

Under a SHM framework, failure of a physical structure is assumed to be the consequence of the history of its internally experienced damage. Therefore, SHM incorporates proactive strategies, such as: prospectively acquiring, processing, and interpreting signals for monitoring, self-diagnostics and prognostics, etc., so that prompt maintenance can take place to avoid irrecoverable failure [32]. SHM has been widely adapted in many disciplines of engineering, and one of the common scenarios is the maintenance of bridges, which experience stress and strain every day. Built in 1936 to connect West Lafayette and Lafayette, Indiana, the Sagamore Parkway eastbound bridge was demolished in 2016, and the old deck of westbound was replaced in the Summer of 2019 [67]. In Hong Kong, SHM has been well established to monitor the impact of strong wind and severe weather conditions to bridges, including the Hong Kong-Zhuhai-Macau sea crossing bridge built in 2018 [68].

The statement by Gross [69] back in 1950s motivated understanding mTBI beyond clinics and through the lenses of engineering dynamics. In essence, clinics and engineering are just like two sides of the same coin. What is so-called "Shàng Yī Zhì Wèi Bìng (the best doctor provides preventive treatment)" is a principal practice in traditional Chinese

Medicine [70] and was documented in *Huang Di Nei Jing Su Wen* back in the late Warring States period [71]. Therefore, in the domain of mTBI, SHM can be applied to prospectively monitor single (concussive) or accumulated (subconcussive) HAEs [32].

At PNG, we monitor brain health of adolescent collision-sport athletes through integrating MRI, biomechanical, and cognitive assessments at multiple sessions across a competition season (Fig. 1.1). Each of the assessments will be described below in detail.
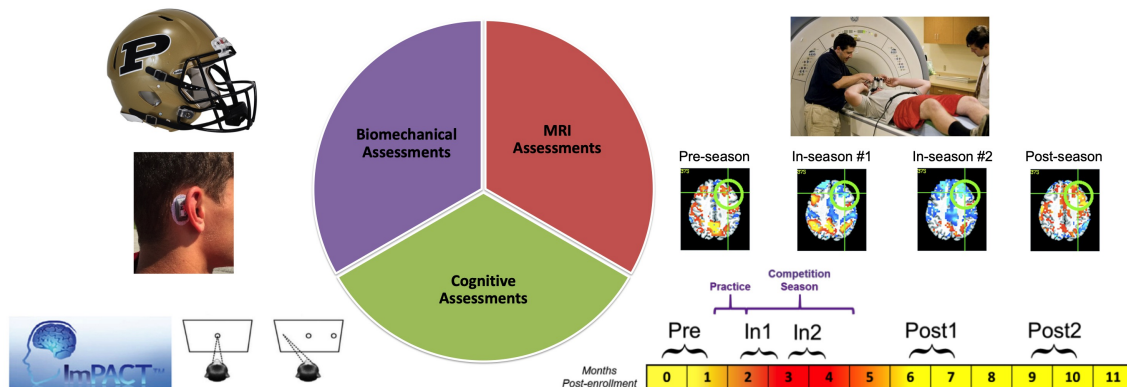
Fig. 1.1. Structural health monitoring framework of Purdue Neurotrauma Group, partially adapted from [32] and [64].

Magnetic Resonance Imaging (MRI) Assessments

MRI can non-invasively monitor the physiological processes of body under health and disease conditions, based on the interaction of the applied magnetic field with mostly the water components of tissues [72]. With the presence of a main magnetic field, the nuclear spins exhibit resonance at an equilibrium state. By applying a radiofrequency (RF) magnetic pulse tuned to the resonance frequency of the spins, the spins absorb energy from the RF pulse, being excited out of equilibrium, and undergo relaxation back to equilibrium once the RF pulse is off. T1 relaxation is the time constant characterizing the return of the magnetization vector along the longitudinal axis, whereas T2 relaxation is the time constant characterizing the decay of the vector component in the transverse plane [73]. The magnetic flux during the relaxation induces an electromagnetic field, generates a voltage in the receiver coil, which contributes to the signal and ultimately the image that distinguishes tissues with different T1 and T2 properties. Typically, water has long T1 and T2, therefore it appears darker in T1 images and brighter in T2 images.

To date, PNG has acquired in total over 1,800 cases of MRI datasets from more than 550 sport athletes over the past ten years. Each dataset is composed of structural (T1-weighted) MRI, fMRI, diffusion MRI (b=1000 and b=2000), and MRS scans. Since 2018, arterial spin labeling, a perfusion MRI sequence, was added into the scanning protocol. Analyses on the datasets have yielded rich insights about how concussion and subconcussive HAEs may alter brain function, structure, and chemistry [32, 62, 63, 65, 74–78].

Biomechanical Assessments

An HAE is an acceleration-deceleration or rotation that causes sudden head movement, either indirectly (from the body, a.k.a. "slosh" effect) or directly [79–81]. In biomechanical assessments, characterizing HAEs involves quantification of peak translational (linear) and angular (rotational) accelerations (in unit of g, force of gravity), as well as tracking the number of HAEs [30]. In general, most of the HAEs occur at 60-120g, and the number of HAEs decay monotonically at 20-120g [82]. Currently, given the sometimes substantial measurement error of specific magnitudes and locations [83, 84], caution must be made when processing and analyzing these measures. In addition, it is still in debate whether a threshold exists for causing concussion and/or concussion-related symptoms [30,85]. Despite the discrepancies and debates, these measures well suit a SHM framework and may be used in the future to guide the development of protective equipment and preventive strategies [32].

At PNG, two telemetry-based sensor systems have been employed to estimate the accumulated exposure to HAEs. The first one is the Head Impact Telemetry System (HITS$^{\text{TM}}$, Simbex LLC), which is helmet-based and provides six uniaxial accelerometers. HITS, however, was previously shown to have limitations in its accuracy [83]. The other (and more reliable) one is the xPatch system (X2Biosystems, Inc.), which is head-based and provides triaxial accelerometer and triaxial gyroscope. Using data from xPatch, our recent work in adolescent collision-sport athletes showed that neurometabolic disturbance was significantly associated with HAEs exceeding 50g [63], and prolonged exposure to subconcussive HAEs may alter cerebrovascular reactivity [76] and produce greater damage in white matter [78].

Cognitive Assessments

Under the SHM framework (Fig. 1.1), an important question is whether the neuroimaging or biomechanical measures can predict cognitive outcomes. For adolescent athletes with concussion or prolonged exposure to subconcussive HAEs, cognitive assessments can assist evaluating recovery and making return-to-play decisions [86].

In athletic training community, one of the widely-administered assessments is Immediate Post-concussion Assessment and Cognitive Test (ImPACT$^{\text{TM}}$) [87,88], a computerized test battery that allows longitudinal monitoring of athlete's verbal memory, visual memory, visual motor speed, reaction time, and impulse control. Studies have shown ImPACT has relatively high false positive rates [74,89], variable reliability [90,91], and therefore warrant caution when interpreting these outcomes.

Besides ImPACT, several assessments of working memory are also administered, including 1) Running memory span [92]; 2) Antisaccade task [93], which assesses attention and inhibitory control; 3) Go/No-go task [94], which evaluates inhibitory control.

1.3 Diffusion Tensor Imaging

Diffusion is the random walks (a.k.a. Brownian motion) of molecules in a medium due to heat. DTI is a quantitative MRI technique that provide signal representations of water diffusion, which can be used to probe the tissue microstructure of white matter [95]. In

this section, the physical principles of MRI and DTI will be introduced, the advantages and technical barriers of DTI will be summarized at the end.

MRI can non-invasively monitor the physiological processes of body under health and disease conditions, based on the interaction of the applied magnetic field with mostly the water components of tissues. With the presence of a main magnetic field, the nuclear spins exhibit resonance at an equilibrium state. By applying a radiofrequency (RF) magnetic pulse tuned to the resonance frequency of the spins, the spins absorb energy from the RF pulse, being excited out of equilibrium, and undergo relaxation back to equilibrium once the RF pulse is off. T1 relaxation is the time constant characterizing the return of the magnetization vector along the longitudinal axis, whereas T2 relaxation is the time constant characterizing the decay of the vector component in the transverse plane. The magnetic flux during the relaxation induces an electromagnetic field, generates a voltage in the receiver coil, which contributes to the signal and ultimately the image that distinguishes tissues with different T1 and T2 properties. Typically, water has long T1 and T2, therefore it appears darker in T1-weighted images and brighter in T2-weighted images.

In MRI, water diffusion can be characterized by a T2-weighted spin-echo sequence with a Stejskal-Tanner diffusion encoding [96], where a pair of diffusion-sensitizing gradients is applied along the same direction, one before and one after the 180° refocusing pulse (Fig. 1.2).
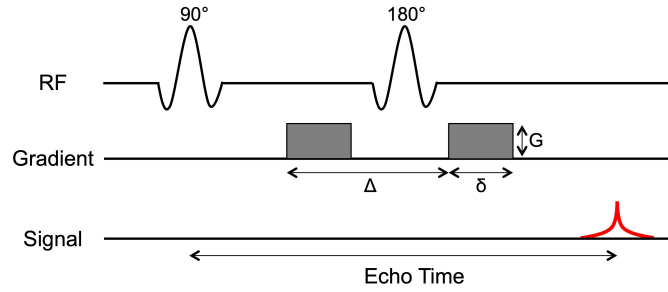
Fig. 1.2. Diagram of a spin-echo pulse sequence with Stejskal-Tanner diffusion encoding [96]. G: gradient amplitude. Δ: the time between the onset of the gradients. δ: gradient duration. Modified from [97].

For a certain diffusion direction vector $\mathbf{n}$ and diffusion weighting b, the diffusion-weighted signal $S(\mathbf{n}, b)$ can be represented as a signal attenuation equation:

$$S = S_0 e^{-bD(\mathbf{n})}$$

where S_0 is the signal intensity at $b=0$, and $D(\mathbf{n})$ is the apparent diffusion coefficient along vector $\mathbf{n}$. b is a diffusion-weighting factor that is determined by:

$$b = \gamma^2 \delta^2 G^2 (\Delta - \delta/3)$$

where γ is the gyromagnetic ratio (42.577 MHz/T), δ is the gradient duration, G is the gradient amplitude, Δ is the time between the onset of the gradients. To estimate $D(\mathbf{n})$, there must be at least one non-zero b value.

In DTI, the white matter microstructural integrity is measured through estimating a symmetric 3-dimension rank-2 Cartesian tensor $\mathbf{D}$ [97]. At least 6 distinct gradient directions are required to estimate $\mathbf{D}$. The three eigenvectors of $\mathbf{D}$ characterizes the primary, secondary, and tertiary directions of water diffusion [98], whereas the three corresponding eigenvalues, λ_1, λ_2, and λ_3, represent the magnitude of water diffusion along each direction. Therefore, $\lambda_1 > \lambda_2 > \lambda_3$. Based on the eigenvalues, two commonly interpreted DTI metrics can be computed:

$$\text{Mean Diffusivity (MD)} = \frac{\lambda_1 + \lambda_2 + \lambda_3}{3}$$

$$\text{Fractional Anisotropy (FA)} = \sqrt{\frac{3}{2}} \times \sqrt{\frac{(\lambda_1 - \text{MD})^2 + (\lambda_2 - \text{MD})^2 + (\lambda_3 - \text{MD})^2}{\lambda_1^2 + \lambda_2^2 + \lambda_3^2}}$$

MD, a.k.a. apparent diffusion coefficient (ADC), represents cellular density and extracellular volume, whereas FA is a scalar value ranging from 0 (isotropic) to 1 (anisotropic) representing the diameter, density and the complexity of the axonal network [95]. Voxels with low FA and high MD values indicate less directionality of water diffusion, which may be due to demyelination or disorganized axonal structures [99].

Additionally, axial (AD) and radial (RD) diffusivity are also commonly reported in DTI literature. They can be calculated from the three eigenvalues for each voxel of the diffusion image:

$$\text{Axial Diffusivity (AD)} = \lambda_1$$

$$\text{Radial Diffusivity (RD)} = \frac{\lambda_2 + \lambda_3}{2}$$

Tract-Based Spatial Statistics (TBSS) is one of the standard voxel-based techniques for diffusion MRI data analysis [100, 101]. TBSS has two distinct characteristics: first, instead of affine image registration, FA maps are *nonlinearly transformed* so that distortion effects are circumvented. Second, instead of running voxel-wise statistical analysis for the entire image volume, neighboring FA voxels are averaged and localized to generate a *skeleton*. The skeleton represents major white matter fiber bundles of the brain, and individual FA data are projected onto the skeleton. Such dimension reduction effectively minimizes partial volume effects and boosted statistical power [100], allowing comparisons of microstructural integrity of white matter at group level [101].

There are several advantages for diffusion MRI, compared to other neuroimaging modalities:

1) Compared to conventional (T1 and T2) MRI techniques, diffusion imaging shows more detailed information of the brain, including white matter microstructure, which cannot be achieved under the spatial resolution of conventional MRI. These information can assist doctors to evaluate the recovery time of patients from brain injury, as well as allow researchers to better understand mechanisms of complex neuropathological disorders, such as sport related concussion and mTBI.

2) Compared to invasive histological methods, diffusion imaging is noninvasive, allowing reconstruction of neuronal pathways without the need of sacrificing subjects or any chemical staining.

3) Compared to CT, there is no radiation associated with diffusion MRI, which allows subjects to be monitored at multiple time points without the concern of tissue damage from too much radiation exposure.

Currently, the limitations of diffusion MRI are:

1) The spatial resolution is relatively low. To investigate an anatomical region or map a specific neuronal pathway, diffusion images and fiber tracts often needs to combine with anatomical MR scans at higher resolution. In order to achieve higher spatial resolution and resolve white matter tracts that are relatively small, the acquisition time needs to be longer, which is a technical barrier in signal sampling [102].

2) Diffusion MRI is prone to the assumptions in tensor modeling to characterize axonal pathways. Crossing fibers violates the assumption of simple tensor model and cannot be resolved [103]. To overcome this technical barrier, advanced diffusion imaging techniques, such as high angular resolution diffusion imaging [104], have been developed to better delineate orientations of crossing fiber [105].

3) The estimation of diffusion MRI parameters is confounded by differences in acquisition parameters, coil designs and configurations, and scanner-specific effects [106,107]. For instance, increasing echo time causes faster decay of the raw signal and changes in DTI parameters [108–110]. Different harmonization methods have been proposed to facilitate joint analysis of diffusion MRI data at large scale [111–114].

Overall, it is important to be aware of the limitations and technical barriers of DTI, as unawareness or ignorance can lead to systematic errors, complicated interpretations, or even false discoveries.

1.4   Brain Atlas

What have not been addressed so far are the questions of *how*: how can DTI detect small changes in the adolescent brain due to repetitive head impacts? How can DTI delineate the relationship between brain health and cognitive performance? Before diving into these questions, it's essential to recognize that imaging-based biomarkers should objectively characterize the statistics of a population, so that interpreting underlying physiology becomes possible. This raises the priority of choosing appropriate brain atlas in image processing.

Brain atlas is a stereotaxic 3D coordinate frame for mapping individual brain images, so that analyses can be performed at group scale [115]. Consists of templates (representative spatial maps) and labels (parcellated brain regions), brain atlas serves as a coordinate reference system that allows automated processing and analyses, without the necessity of being an expert in neuroanatomy. A brain atlas may be employed bidirectionally, i.e. individual brain images can be registered and spatially normalized to the atlas space while retaining the anatomical identities (e.g. shape) as much as possible, or alternatively, referenced from the atlas to retrieve different types of information. Some examples are: segmenting brain volumes [116], estimating cortical thickness and surface area [115], performing voxel-based analyses [117]. To date, there is no population-specific brain atlas for adolescent collision-sport athletes, and the next chapter will describe the efforts of filling this critical gap.

2. DEVELOP POPULATION-SPECIFIC BRAIN ATLASES FOR EARLY-TO-MIDDLE ADOLESCENT COLLISION-SPORT ATHLETES

2.1 Abstract

Human brains develop across the life span and largely vary in morphology. Adolescent collision-sport athletes undergo repetitive head impacts over years of practices and competitions, and therefore may exhibit a neuroanatomical trajectory different from healthy adolescents in general. However, an unbiased brain atlas targeting these individuals does not exist. Although standardized brain atlases facilitate spatial normalization and voxel-wise analysis at the group level, when the underlying neuroanatomy does not represent the study population, greater biases and errors can be introduced during spatial normalization, confounding subsequent voxel-wise analysis and statistical findings. In this work, targeting early-to-middle adolescent (EMA, ages 13-19) collision-sport athletes, we developed population-specific brain atlases that include templates (T1-weighted and diffusion tensor magnetic resonance imaging) and semantic labels (cortical and white matter parcellations). Compared to standardized adult or age-appropriate templates, our templates better characterized the neuroanatomy of the EMA collision-sport athletes, reduced deformation introduced during spatial normalization, and exhibited higher sensitivity in diffusion tensor imaging analysis. In summary, these results suggest the population-specific brain atlases are more appropriate towards reproducible and meaningful statistical results, which better clarify mechanisms of traumatic brain injury and monitor brain health for EMA collision-sport athletes.

2.2 Keywords

Atlas Template; Adolescents; Traumatic Brain Injury; Magnetic Resonance Imaging; Spatial Normalization

2.3 Introduction

Adolescent collision-sport (e.g., American football and soccer) athletes bear high risk of mild traumatic brain injury (mTBI), a complex pathophysiological process that can arise from either single (concussive) or accumulated (subconcussive) head acceleration events [29, 30, 118, 119]. The lack of sensitive biomarkers hinders the development of preventive strategies, allowing this vulnerable population to continue participating at greater risk. Multi-modal magnetic resonance imaging (MRI) can non-invasively characterize the structure and function of the human brain in healthy and disease states, thus showing promise for prospective screening and early detection of mTBI in adolescent athletes. Nevertheless, one of the critical steps in MRI processing is to spatially normalize brain images to a stereotaxic atlas, i.e., a coordinate reference system for neuroimaging studies. When the

spatial normalization onto an atlas has poor accuracy, voxel-based analysis exhibits low sensitivity in detecting differences at group level [117, 120]. Therefore, it is vital to ensure most of the anatomical identities pertinent to adolescent athletes are retained during spatial normalization.

In general, human brain atlases are either standardized or population-specific; each comes with a set of templates (representative spatial maps) and labels (parcellated regions). The two standardized brain atlases long established and well known by the neuroimaging community come from Talairach and the Montreal Neurological Institute [121]. Talairach atlas is derived from the dissection of one hemisphere of the brain from a 60-year-old French woman [122], whereas the ICBM152 template is derived from T1 scans of 152 subjects aged 18.5-43.5, averaged together after high-dimensional linear and nonlinear registration into the Talairach space [123]. In the same space as ICBM152, FMRIB58 is a standardized diffusion tensor imaging (DTI) template derived from 58 high-resolution volumes of fractional anisotropy (FA) from healthy male and female adults aged 2050 (FMRIB, Oxford, UK). Other popular standardized human brain atlases include Brainnetome [124], IIT [125], SRI24 [126], etc. Recently, two systematic evaluations of DTI templates showed that the IIT standard template outperformed population-specific DTI templates [125, 127], but the findings were based on healthy adults and may not generalize in younger populations. Many literature pointed out the age-related changes in volumes of gray and white matter [116, 128–132]. Although there are several age-specific atlases for adolescents [133–138], the number is limited compared to adult atlases [128].

The existing brain atlases are handy tools for various types of neuroimaging analyses, but considering the various pathological conditions and the developing nature of human brain, they do not always suit the best for studying specific populations. In a multiple sclerosis population, Van Hecke et al. [139] showed that choosing a non-specific template can negatively impact the final results of tract-based spatial statistics (TBSS) [100], one of the standard approaches for DTI analysis [117, 140]. Using both simulated and real DTI data, Van Hecke et al. observed that a population-specific DTI template resulted in more reliable voxel-based analysis, as well as higher sensitivity and specificity of detecting DTI changes, compared to the standardized template [139]. However, developing a study-specific template from a large population is time consuming, computationally inefficient [140], and may result in suboptimal quality [125, 139], making the use of existing brain atlases a more pragmatic option for the time being.

To date, an unbiased brain atlas targeting adolescent collision-sport athletes does not exist, to the best of our knowledge. DTI literature of sports-related mTBI and subconcussive trauma in adolescents either manually defined their own ROIs [141–143], or more often did not employ a population-specific template to spatially normalize each individual brain image, see Table 2.1 for a summary. Variability introduced during spatial normalization may confound statistical analyses and contribute to varied DTI findings that make it difficult to interpret axonal pathology [144]. It is critical for studies of mTBI and subconcussive trauma, especially for adolescent collision-sport athletes, to minimize bias and errors in every pre-processing stages, because the magnitudes of changes are often subtle, and brains of this age bracket are rapidly growing [145–148]. Such studies may benefit from using an unbiased brain atlas created from their study cohort, as opposed to normalizing brains of adolescent collision-sport athletes to an atlas generated from adults or healthy adolescents.

Table 2.1.

Original studies of human diffusion magnetic resonance imaging in adolescent collision-sport athletes with repetitive head impacts (up to July 2020; sorted by last names of first authors, then by year of publication).

Author (Year)	Study Population (N)	Age [range]	Atlas	Approach		Main Findings
Babcock et al. (2015) [149]	mTBI patients (N=23)	13.2 ± 1.8 [11, 16]	MNI	Voxel-based analysis		mTBI showed ↑ FA/AD and ↓ MD/RD in several WM regions
Bartnik-Olson et al. (2014) [141]	Concussed athletes (N=15)	14.8 ± 2.8 [8, 17]	N/A	Manual delineation		↑ ADC of the genu in concussed subjects with behavioral complaints vs. those without complaints and the controls
Bazarian et al. (2012) [150]	Hockey/football athletes (N=9)	17.0 ± 0.7 [16, 18]	Type II JHU WMPA [151]	Wild bootstrapping [152]		Higher pre-post FA and MD change in concussed subjects vs. subjects with subconcussive head blows
Borich et al. (2013) [153]	Concussed hockey athletes (N=12)	15.5 ± 1.2 [13, 17]	MNI	ROI-based analysis voxel-based TBSS	and	↓ AD and a trend towards ↓ MD/RD in concussed athletes
Chun et al. (2015) [75]	Football athletes (N=28)	15.9 ± 1.4 [15, 18]	JHU ICBM-DTI-81 [154]	ROI-based analysis voxel-based TBSS	and	Significant pre-post FA ↑ and ↓ in several WM regions; ↑ variance of FA changes with more hits
Davenport et al. (2014) [155]	Football athletes (N=24)	16.9 ± 0.6	MNI	Voxel-based analysis		Significant association between risk-weighted cumulative exposure and changes of the DTI metrics
Davenport et al. (2016) [156]	Football athletes (N=24)	16.9 ± 0.6	MNI	Voxel-based analysis		Significant association between risk-weighted cumulative exposure and DKI-derived metrics and white matter modeling parameters
Foss et al. (2019) [157]	Football athletes, Youth (N=12) and HS (N=21)	13.1 ± 0.6 (Youth); 17.3 ± 0.7 (HS)	Not reported	ROI-based analysis voxel-based TBSS	and	Significant pre-post ↓ AD in Youth athletes; ↓ MD, AD, and/or RD in High school athletes
Jang et al. (2019) [78]	Football athletes (N=61)	16.6 ± 0.9 [14, 18]	FMRIB58_FA	ROI-based analysis voxel-based TBSS	and	Hit events correlated with ↓ FA and ↑ MD
Kuzminski et al. (2018) [158]	Football athletes (N=17)	16.0 ± 0.7 [15, 17]	FMRIB58_FA	ROI-based analysis voxel-based TBSS	and	No significant FA change across the season; ↓ FA in several WM regions correlated with higher number of impacts
Maugans et al. (2012) [142]	Concussed patients (N=12)	13.4 ± 1.2 [14, 17]	N/A	Manual delineation		No significant DTI change
Mayer et al. (2012) [159]	Pediatric mTBI (N=15)	13.5 ± 2.1 [10, 17]	FMRIB58_FA	ROI-based analysis voxel-based TBSS	and	mTBI showed ↑ FA in several WM regions
Myer et al. (2016a) [160]	Hockey athletes (N=15)	16.3 ± 1.2	MNI	Voxel-based TBSS		Significant ↑ MD and RD from pre-season to mid-season in Non-collar group; no significant change in Collar group
Myer et al. (2016b) [161]	Football athletes (N=21)	17.1 ± 0.7	MNI	ROI-based analysis voxel-based TBSS	and	Significant pre-post ↓ MD, AD, and/or RD in Non-collar group; no significant change in Collar group
Myer et al. (2019) [162]	Soccer athletes, Collar (N=11) and Non-collar (N=11)	13.1 ± 0.6 (Collar); 17.3 ± 0.7 (Non-collar)	MNI	ROI-based analysis voxel-based TBSS	and	Significant pre-season to post-season ↓ of MD, AD, and/or RD in Non-collar group, followed by post-season to off-season ↑; no significant change in Collar group
Nilsson et al. (2019) [143]	Football athletes (N=35)	[8, 12]	N/A	Manual delineation		No significant FA change across the season; Total magnitude of hits correlated with ↑ FA in one WM region
Satchell et al. (2019) [163]	Concussed athletes (N=17)	13.4 ± 2.3	Not reported	Voxel-based TBSS leave-one-out analyses		No significant DTI change
Virji-Babul et al. (2013) [164]	Concussed athletes (N=12)	15.5 ± 1.2 [14, 17]	MNI	ROI-based analysis	and	Significant ↑ FA and ↓ MD in concussed athletes vs. controls
Yuan et al. (2018) [165]	Football athletes (N=21)	[16.5, 18.9] (Collar); [17.2, 19.7] (Non-collar)	MNI	Voxel-based TBSS		Significant pre-post ↓ MD, AD, and/or RD in non-collar group, partial ↑ at off-season; no significant change in Collar group

Note: HS = High school

Therefore, the purpose of this work is to develop population-specific brain atlases for early-to-middle adolescent (EMA) collision-sport athletes. Based on the Purdue Neurotrauma Group (PNG) longitudinal MRI database [32], we aim to develop:

1) one T1 template, based on the images from 215 EMA collision-sport athletes,

2) T1-based semantic labels of cortical and white matter parcellations, and

3) one DTI template, based on 64 EMA football athletes in a single competition season [166, 167].

To evaluate the templates, our hypothesis is that compared to using a non-specific template, the PNG templates can reduce deformation when normalizing brain images of local adolescent athletes and improve statistical power in detecting small differences in population studies using local datasets. The evaluation includes voxel-based morphometry that characterized the extent of shape changes of the T1 images during spatial normalization, and sensitivity of detecting longitudinal DTI changes in high school football athletes over a single season, which has been reported in previous work [166,167] that utilized the standardized FMRIB58 template. The brain atlases have been made available for download [168], and a user manual is provided at Appendix A.

2.4 Methods

2.4.1 Participants and Data Collection

This study used data collected by PNG in their ongoing longitudinal study of adolescent athletes [32], which has been approved by the Biomedical IRB of Purdue's Human Research Protection Program and was carried out in accordance with the Declaration of Helsinki. These data include athletes participating in the collision sports of American football (all males) and soccer (all females), plus data from peer non-collision-sport athletes. For collision-sport athletes, data were acquired across multiple sessions, including one approx. one month before contact practices began (*Pre*), one or more within competition season (*In*), and one or more after the season ended (*Post*). These data were grouped into different datasets to construct or evaluate the population-specific T1 or DTI templates. See Table 2.2 for the total number of participants and relevant details for each dataset.

Note that during the period of study, no participant was diagnosed by their athletic trainer or team physician as being concussed.

2.4.2 MR Imaging

All data were acquired using a 3 T General Electric Signa HDx (Waukesha, WI) with a 16-channel brain array (Nova Medical; Wilmington, MA).

Table 2.2.
Summary of the datasets for constructing and evaluating the population-specific T1 and DTI templates, based on Purdue Neurotrauma Group (PNG) longitudinal MRI database [32].

	Task	Season	Session	n Participants	Sport* (n)	Age (years)
PNG T1 template						
	Construction	2011–2017	Pre-, In-, Post-Season	215	Football (175), Soccer (40)	13–19
	Evaluation	2018–2019	Pre-Season	12	Football (12)	14–19
PNG DTI template						
	Construction	2016–2017	Pre-Season	64	Football (64)	14–18
	Evaluation	2016–2017	Pre-, In-Season	64	Football (64)	14–18

* All football athletes are male participants, and all soccer athletes are female participants.

T1-weighted imaging data

Anatomical T1 scans were acquired using a 3D fast spoiled gradient-echo sequence (TR/TE = 5.7/2.0 ms, flip angle = 73°, 1 mm isotropic resolution). Longitudinal volumetric data from 227 athletes (187 males; 40 females) were used for construction and evaluation of the template.

Diffusion-weighted imaging data

Diffusion-weighted imaging (DWI) data were acquired using a spin-echo echo-planar imaging sequence (TR/TE = 12,500/100 ms, 40 slices with 2.5 mm thickness), FOV of 24×24 cm^2, a 96×96 acquisition matrix, in-plane resolution of 2.5×2.5 mm^2, with 30 diffusion-encoding directions at b = 1000 s/mm^2 and one at b = 0 s/mm^2, and an upsampled isotropic resolution of 1 mm. Longitudinal data from sixty-four male football athletes that participated in one competition season. All participants completed three MRI sessions: one scan at *Pre* and two In-Season scans, with one in the first (*In1*) and one in the second (*In2*) 5-week halves of the season.

2.4.3 Atlas Construction

To accelerate the computation time, we established a workflow integrating a high-throughput (Open Science Grid) [169, 170] and a high-performance (Purdue Community Clusters) computing platform. Specifically, Open Science Grid integrates the computing and storage elements from over 100 individual sites spanning the United States and provides a distributed fabric of high-throughput computational services, allowing numerous individual, small, and independent tasks to run concurrently on different CPU cores. Purdue Community Clusters consists of Dell compute nodes with 1624 cores of Intel Xeon Gold Sky Lake processors per node, at least 192 GB of RAM, and 100 Gbps InfiniBand interconnects, which processes single, large, and interdependent tasks at its fastest speed. The

workflow was implemented to construct the population-specific T1 template and one of the two population-specific DTI templates, and the schematic diagrams were shown in Fig. 2.1.

Population-specific T1 template and labels

The workflow was summarized in Fig. 2.1A. T1 preprocessing included denoising [172], bias correction, skull-stripping, and intensity normalization [173], followed by the first visual quality assessment where preprocessed T1 images with low signals, cutoff of brain regions, motion, or observable artifacts were excluded; this resulted in 782 T1 images from 235 participants, where 547 were repeated scans from 168 participants.

We applied the Advanced Normalization Tools (ANTs) [171,174], a top-performing registration tools, to construct T1 template. ANTs employs symmetric groupwise normalization that has been shown to retain accurate anatomical details [175]. Using *buildtemplateparallel.sh* in ANTs, an individual template was created per participant on Open Science Grid, followed by the second visual quality assessment, which mainly focused on resemblance of neuroanatomy pertinent to each individual; this resulted in individual templates from 215 participants with good quality. Using Purdue Community Clusters, the final population-specific template (PNG T1) was created from the individual templates.

Based on the final template, the semantic labels were created using the *recon-all* pipeline of FreeSurfer [176] (Fig. 2.3). Three labeling protocols were employed by the pipeline: Desikan-Killiany protocol [177], Desikan-Killiany-Tourville classifier protocol [178], and Destrieux protocol [179]. The template and the labels created by Desikan-Killiany protocol have been made available at Purdue University Research Repository [168].

Population-specific DTI templates

We applied two top-performing registration tools, namely ANTs [171] and DTI-TK [180], to construct DTI templates. DTI-TK incorporates explicit optimization of tensor orientation with piecewise affine registration (for algorithm, see Zhang et al. [180]), which demonstrated accurate spatial normalization [120].

Before constructing the templates, raw DWI data were first preprocessed using FSL (FMRIB 5.0, Oxford, U.K.), including corrections for motion and eddy currents (*eddy_correct*), followed by the extraction of aliasing-corrected brains (*BET*). DTI metrics, including FA, mean diffusivity (MD), axial diffusivity (AD), and radial diffusivity (RD), were estimated for each individual (*DTIFit*), and all passed the first visual quality assessment for presence of motion artifact or geometrical distortion.

The workflow of constructing the PNG (ANTs) template is summarized in Fig. 2.1B. Based on the quality assessments when constructing the population-specific T1 template, 33 of the 64 football players had a qualified T1 image at *Pre*. Only the corresponding DWI images at *Pre* were used, considering that DTI changes were observed at *In*1 and *In*2 [166,167]. For each subject, the b_0 image served as the reference image to warp the FA image to the corresponding T1 image, and subsequently to the PNG T1 template space. All warping processes were carried out by running *antsIntermodalityIntrasubject.sh*. All the warped FA images passed the second visual quality assessment for inspecting whether they were normalized to the same space of the template. Then, an average map of the
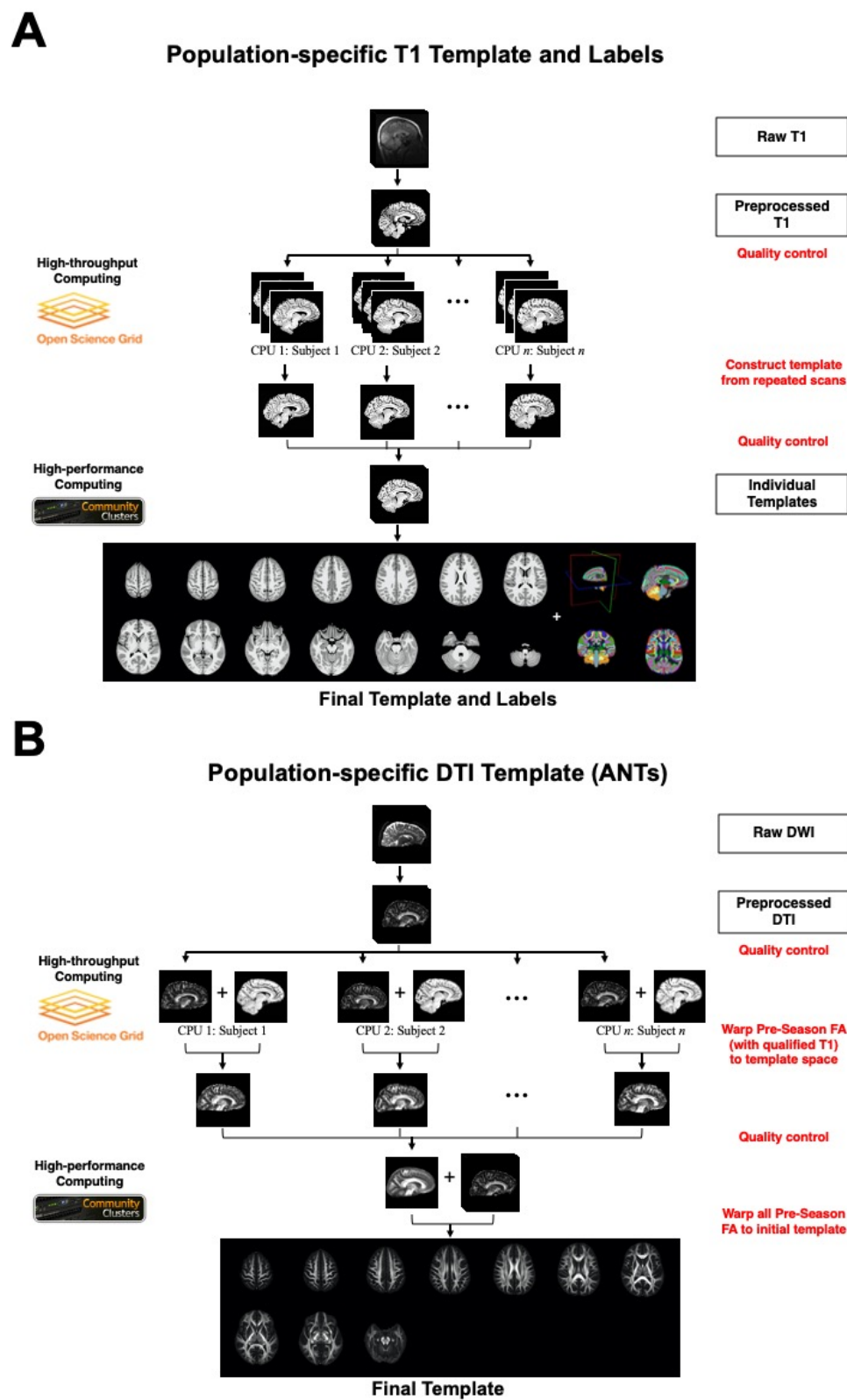
Fig. 2.1. High-throughput high-performance computing workflow, for constructing (**A**) the population-specific T1 template and labels, and (**B**) the population-specific DTI template using Advanced Normalization Tools (ANTs) [171].

warped FA images was computed to serve as the initial reference image to register to, and the population-specific DTI template was constructed based on the 64 football players at *Pre* (*antsMultivariateTemplateConstruction.sh*), and has been made available at Purdue University Research Repository [168]. The second DTI template was constructed using DTI-TK [180] as a comparison to the PNG (ANTs) template, where the diffusion tensors in the native space of 64 subjects were used.

2.4.4   Evaluations

Population-specific T1 template

Deformation-based morphometry analyses were performed to evaluate potential bias of using different T1 templates. Newly acquired T1 scans of 12 high school varsity football athletes (ages: 14-19) prior to the 2018-2019 competition season were normalized (via *antsRegistrationSyN*) to ICBM152 template, an age-appropriate template (NIHPD$_{13.0-18.5}$ [134], IITv3.0 [125], and the population-specific T1 template (PNG); this yielded $4 \times 12 = 48$ maps of deformation field. The logarithm of Jacobian determinant ($\log J$, representing local volume difference) was estimated (via *ANTSJacobian*) for each map. The maps of absolute $\log J$ were computed and transformed to the standard space of ICBM152 (1 mm spatial resolution) via *antsApplyTransforms*. In the standard space, voxel-wise permutation-based t-statistics were computed with 5,000 permutations with a repeated ANOVA design, using the FSL Randomise program [181], with threshold-free cluster enhancement [182] and family wise error (FWE) of 5% used to control for type-I error.

Population-specific DTI template

All individual FA images were first aligned through a nonlinear transformation algorithm (*fnirt*) to four DTI templates, including two standardized templates: FMRIB58 (FMRIB, Oxford, UK) and IITv3.0 [125], and the two PNG population-specific templates constructed by ANTs and DTI-TK respectively.

Similar to evaluating the T1 templates, deformation-based morphometry analyses were performed to evaluate potential bias of using different DTI templates. At each session (*Pre*, *In*1, *In*2), $4 \times 64 = 256$ maps of absolute $\log J$ were yielded, and all were transformed to the standard space of FMRIB58 (same as ICBM152). Using the same design as evaluating the T1 templates, voxel-wise permutation-based t-statistics were computed for each session.

In the standard space of ICBM152, a skeleton representing the common white matter tracts across all the subjects was created from thinning the mean FA map that was averaged from all the aligned FA images. The skeleton was thresholded at FA>0.2 to reduce partial volume effects between borders of different tissues. Regional maximal FA values were projected onto the skeleton according to a distance map [100]. Based on the mean FA skeleton, skeletons of MD, AD, and RD were obtained by projecting the corresponding DTI values onto the FA skeleton (*tbss_non_FA*). The processing procedure guaranteed that the variations of the TBSS results were only related to the template selection.

The resulting DTI skeletons of each subject were fed into voxel-wise permutation-based statistics with a repeated ANOVA design and with 5,000 permutations among *Pre*, *In*1 and

*In*2, using the FSL Randomise program [181]. The type-I error was controlled by threshold-free cluster enhancement [182] and FWE of 5%. For the purpose of demonstrating the effect of template selection on subsequent statistical findings, only the contrasts comparing *Pre* and *In*2 were presented. Among all the selected contrasts of each template, the ones showing significant voxels at $p < 0.05$ (FA and AD: *Pre* ¿ *In*2; MD and RD: *Pre* < *In*2) were further segmented into ROIs defined by the JHU-ICBM-DTI-81 WM label atlas [183], and the corresponding voxel counts and DTI values were extracted via the FSL Cluster program.

Within each ROI overlaid on the TBSS skeletons, we counted

$$V_t = \text{The number of voxels on the skeleton},$$

and

$$V_s = \text{The number of significant voxels from the permutation} - \text{based statistics}.$$

First, non-parametric Friedman test was performed to test whether V_t correlated with template selection, with V_t as the response variable, template as the predictor, and ROI as the blocking variable.

Then, logistic regression was performed to test whether V_s/V_t correlated with template selection:

$$\log \frac{p_{ij}}{1 - p_{ij}} = \beta_0 + \beta_1 \times \text{Template}_i + \beta_2 \times \text{ROI}_j$$

where p_{ij} referred to the V_s/V_t ratio from the ith template, with regard to the TBSS skeleton within the jth ROI. 4 models were established with respect to the V_s/V_t ratio of each DTI metric (FA, MD, AD and RD). ROIs with no voxel on the TBSS skeletons were excluded from the analyses. The analyses were performed using SAS 9.4 (SAS Institute, Cary NC).

To investigate the sensitivity of different templates to the short-term changes of white matter microstructure in high-school football players [166, 167], linear mixed regression analyses were performed, where timepoint and age were the fixed variables, and subject was the random variable. Models were fitted within each ROI and for each DTI metrics. Akaike information criterion (AIC) was used to evaluate model fit, and t and p values for timepoint were compared across the four templates. FDR was applied to correct for comparisons in multiple ROIs. ROIs with no voxel on the skeleton, and ROIs rejected by the Shapiro-Wilks normality test were excluded from the analyses. The analyses were performed using R version 3.5.2 [184].

2.5 Results

2.5.1 Atlas Construction

The total computation time for constructing the PNG T1 template was about 28.5 hours, where ~6.5 hours were accounted for creating each individual template at Open Science Grid, and 22 hours for creating the final T1 template when fully using one node (24 cores) of the high-performance computing clusters. The comparison of shape and size between the standardized and PNG T1 template was shown in Fig. 2.2A.

The total computation time of constructing the PNG (ANTs) DTI template was about 12.5 hours; warping each of the *Pre* FA images ($N = 33$, with qualified T1) to the space of PNG T1 template took ˜2 minutes at Open Science Grid, and the majority of time were spent on constructing the final DTI template when fully using one node (24 cores). The comparison of shape and size between the standardized and PNG DTI templates were shown in Fig. 2.2B.
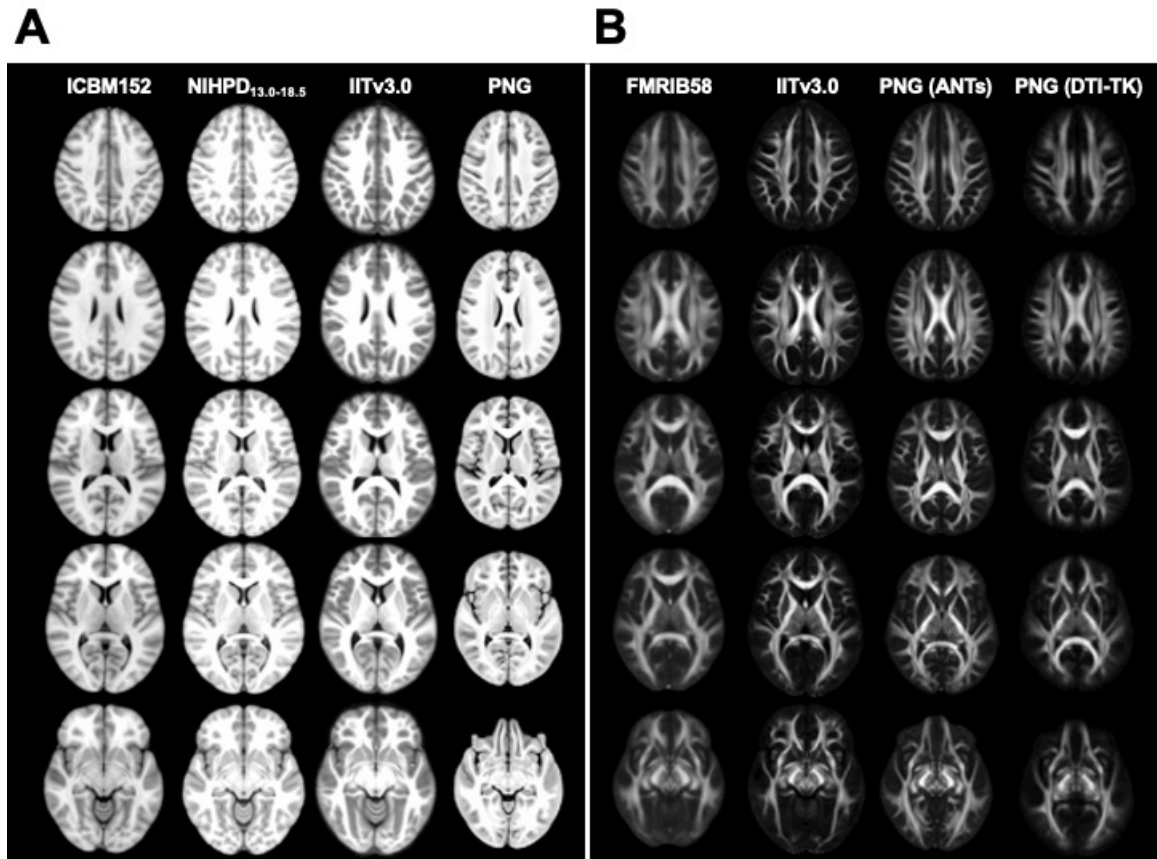
Fig. 2.2.   (**A**) Standardized T1 templates, including ICBM152 [123], NIHPD$_{13.0-18.5}$ [134], IITv3.0 [125], and the population-specific T1 template. (**B**) Standardized FMRIB58 (FMRIB, Oxford, UK), IITv3.0 [125], and the population-specific DTI templates constructed by ANTs [171] and DTI-TK [180].
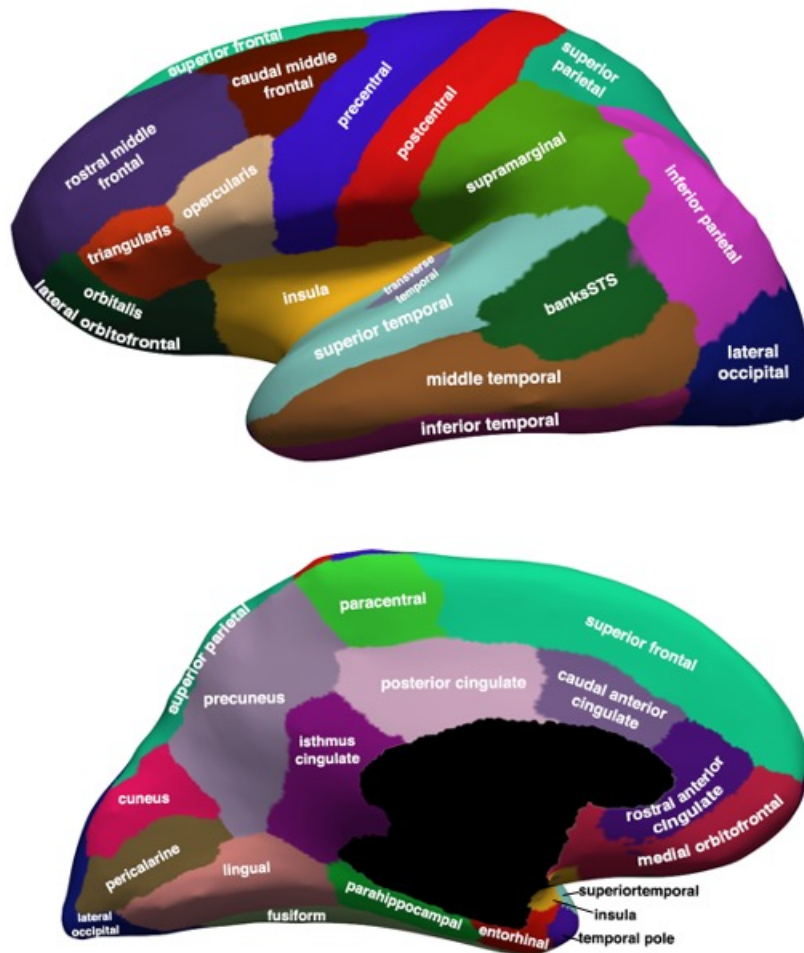
Fig. 2.3. Lateral (top) and medial (bottom) views of PNG Desikan-Killiany Grey Matter Atlas. banksSTS: banks of the superior temporal sulcus.

2.5.2 Evaluation of population-specific T1 template

The results of deformation-based morphometry analyses are shown in Fig. 2.4. Compared to ICBM152 (Fig. 2.4A) or NIHPD$_{13.0-18.5}$ template (Fig. 2.4B), no significantly larger log$J$ was produced from using PNG template for the spatial normalization. Compared to IITv3.0 (Fig. 2.4C), fewer voxels showed significantly larger log$J$ when using PNG template (IITv3.0: 334,811 voxels; PNG: 109,189 voxels).
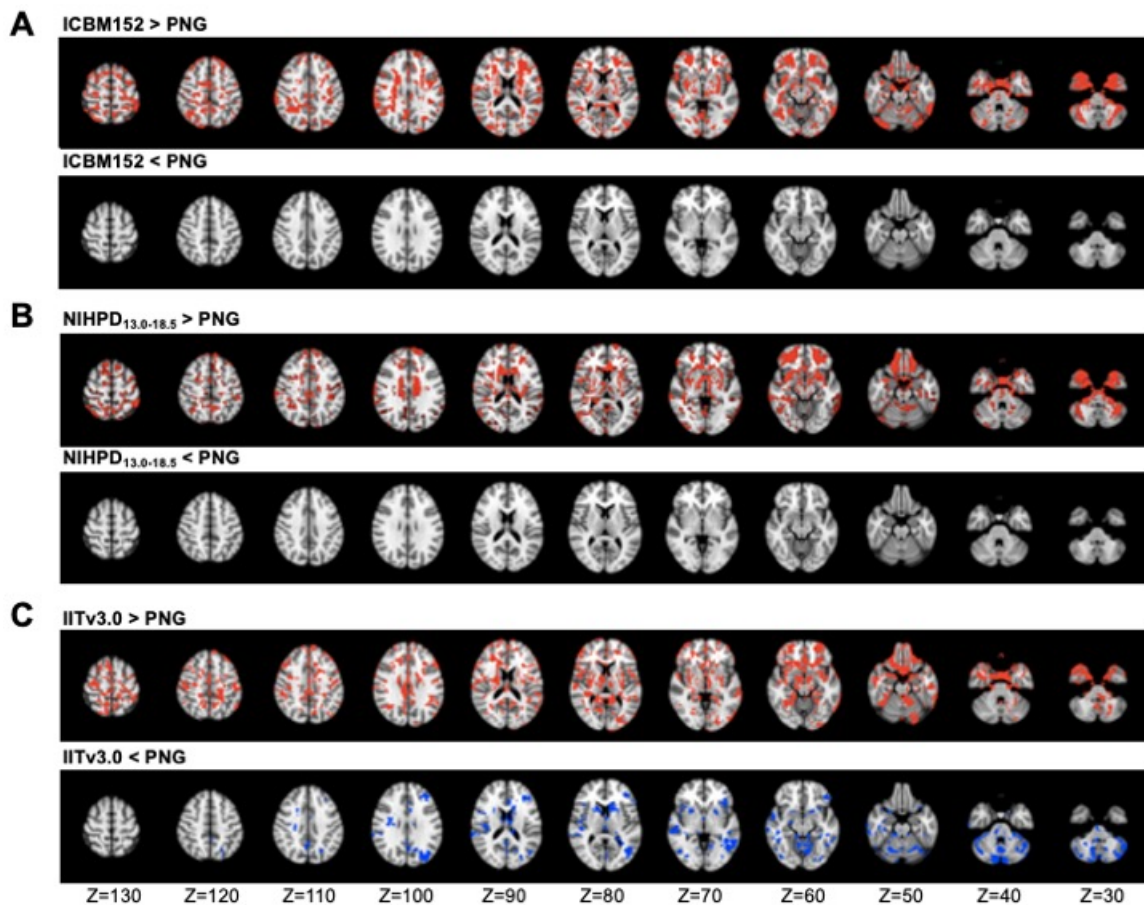
Fig. 2.4. Voxel-wise t-statistical maps ($p < 0.05$, FWE corrected) of potential bias between our PNG T1 template and (**A**) ICBM152 [123], (**B**) NIHPD$_{13.0-18.5}$ [134], and (**C**) IITv3.0 [125], represented in axial view in ICBM152 space. Red/blue indicates significantly larger/smaller deformation during spatial normalization, compared to using PNG template.

2.5.3 Evaluation of study-specific DTI template

Similar to the deformation-based morphometry findings for T1 templates, at all the sessions (*Pre*, *In*1, *In*2), fewer voxels showed significantly larger log$J$ when using the PNG (ANTs) template compared to the high-quality standardized DTI templates (FMRIB58 and IITv3.0) (Table 2.3). Using the PNG (ANTs) template also exhibited fewer voxels of significantly larger log$J$ than the PNG (DTI-TK) template (Table 2.3). Illustrations of the voxel-wise t-statistical maps were provided in Fig. 2.5.

Table 2.3.

Number of statistically significant ($p < 0.05$, FWE corrected) voxels of potential bias when normalizing the FA maps of 64 high school varsity football athletes to PNG (ANTs) DTI template and to the other templates. Comparisons at multiple sessions (*Pre*, *In*1, *In*2) were presented.

Contrast	*Pre*	*In*1	*In*2
FMRIB58 > PNG (ANTs)	588,188	594,116	591,845
FMRIB58 < PNG (ANTs)	126,667	85,782	153,490
IITv3.0 > PNG (ANTs)	597,688	598,457	608,754
IITv3.0 < PNG (ANTs)	69,359	49,774	81,651
PNG (DTI-TK) > PNG (ANTs)	481,365	464,482	445,434
PNG (DTI-TK) < PNG (ANTs)	172,137	181,668	189,488
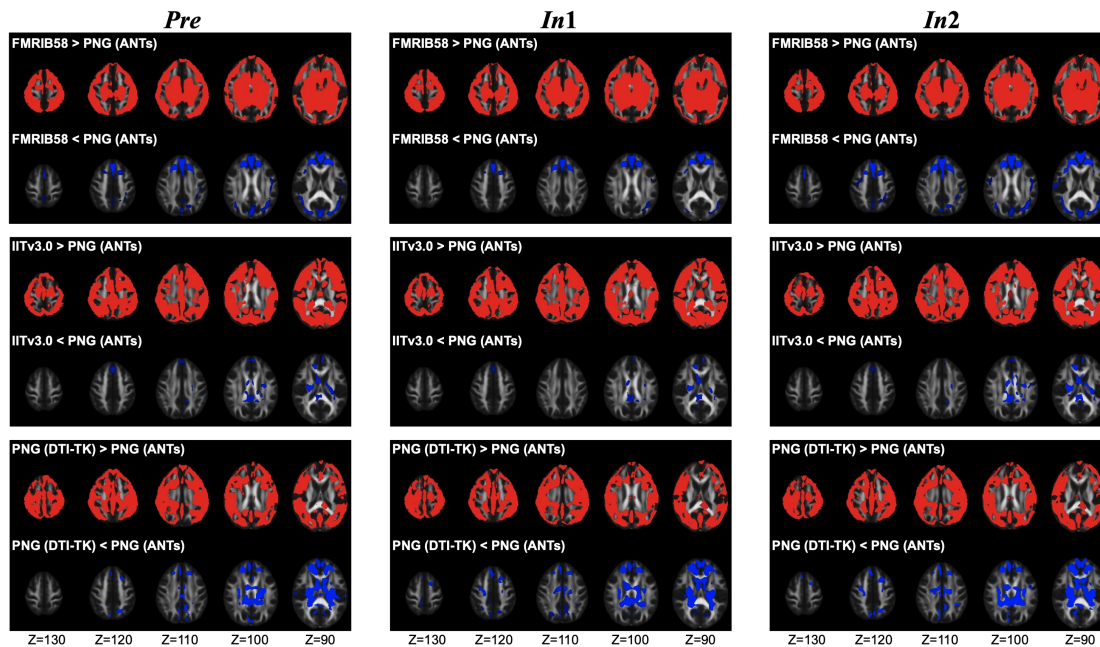
Fig. 2.5. Voxel-wise t-statistical maps ($p < 0.05$, corrected) of potential bias, comparing PNG (ANTs) template to high-quality standardized DTI templates (FMRIB58 and IITv3.0), and to PNG (DTI-TK) template, represented in axial view in ICBM152 space. Red/blue indicates significantly larger/smaller deformation during spatial normalization, compared to using PNG (ANTs) template.

Table 2.4 summarized the number of statistically significant voxels of DTI metrics (FA, MD, AD, RD) and the total number of voxels on TBSS skeleton. Non-parametric Friedman test did not suggest covariate template as a significant factor (χ^2=2.370, df=3, p=0.499) for V_t.

Table 2.4.
Summary of the ratios of the number of statistically significant voxels of DTI metrics (FA, MD, AD, RD) and the total number of voxels on TBSS skeleton.

DTI	Contrast	Total Significant Voxels/Total Voxels			
		FMRIB58	IITv3.0	PNG (ANTs)	PNG (DTI-TK)
FA	$Pre > In2$	16885/30017	16040/29481	16785/29740	15864/29888
MD	$Pre < In2$	7544/30017	6791/29481	6838/29740	6675/29888
AD	$Pre > In2$	888/30017	0/29481	571/29740	100/29888
RD	$Pre < In2$	12235/30017	11598/29481	12093/29740	11889/29888

Hosmer Lemeshow Goodness-of-Fit test showed a good fit for the logistic regression models of FA, MD, and AD (all $p > 0.05$), except RD ($p < 0.05$) (Table 2.5). However, in all 4 models, covariate template was a significant factor ($p < 0.05$, Wald Chi-square test) for the V_s/V_t ratios (Table 2.5). Therefore, there were some evidence to indicate a strong correlation between the V_s/V_t ratios and template selection.

Table 2.5.
Summary of Hosmer Lemeshow Goodness-of-Fit test and logistic analysis for the effect of the selected template on the ratio of the number of significant voxels (from the permutation-based t-statistical maps) and total number of voxels on the TBSS skeleton within the ROI.

DTI	Contrast	Goodness-of-Fit Test			Wald Test		
		χ^2	df	p	χ^2_{template}	df_{template}	p_{template}
FA	$Pre > In2$	11.478	8	0.176	9.759	3	0.020
MD	$Pre < In2$	7.516	7	0.377	12.249	3	0.007
AD	$Pre > In2$	1.725	1	0.189	299.374	3	<0.001
RD	$Pre < In2$	52.032	8	<0.001	20.680	3	<0.001

Within most of the white matter tracts, the number of significant voxels exhibiting decreased FA at *In2* vs. *Pre* was similar across the four templates (Fig. 2.6). For the PNG (ANTs) template, the significant voxels in fornix were 99 mm^3, much larger compared to FMRIB58 (14 mm^3), IITv3.0 (5 mm^3), and the PNG (DTI-TK) templates (13 mm^3) (Fig. 2.6A). For the PNG (DTI-TK) template, the significant voxels in bilateral cingula

were much smaller compared to the other three templates (Fig. 2.6B). In bilateral cingula (hippocampi), neither IITv3.0 or PNG (DTI-TK) template exhibited significant voxel of FA difference (Fig. 2.6B&C). Similarly, no significant voxel of FA difference was observed in left tapetum for FMRIB58 template.

Figs. 2.7, 2.8, and 2.9 provide illustrations of the t-statistical maps for significant differences of MD, AD, and RD, at *In2* vs. *Pre*. Detailed summary of the significant voxels exhibiting differences of FA, MD, AD, and RD can be found at Tables 2.6, 2.7, 2.8, and 2.9.

According to the linear mixed-effect regression analyses for the longitudinal changes of FA (Table 2.10), model fits were similar among the regions commonly identified across the 4 templates. FMRIB58 exhibited the highest model fit (i.e., lowest AIC) in most of the white matter tracts, including the left cerebral peduncle, left posterior corona radiata, right superior corona radiata, right external capsule, left anterior internal capsule, right posterior internal capsule, left inferior longitudinal/fronto-occipital fasciculus, and left stria terminalis. For IITv3.0, the highest fits were observed in the right cingulum, right anterior corona radiata, and right anterior internal capsule. For the PNG (ANTs) population-specific template, higher fits were observed in the bilateral superior fronto-occipital fasciculus and right superior longitudinal fasciculus. whereas the PNG (DTI-TK) template exhibited the highest fit in the right anterior corona radiata and left superior corona radiata.

Tables 2.11 and 2.12 summarized the linear mixed-effect regression analyses for the longitudinal changes, for MD and RD respectively. Similar to FA, model fits were similar among the commonly identified regions. No table was shown for AD, since there was no voxel exhibited the significant difference when IITv3.0 DTI template was used (see Table 2.4 and Fig. 2.8).
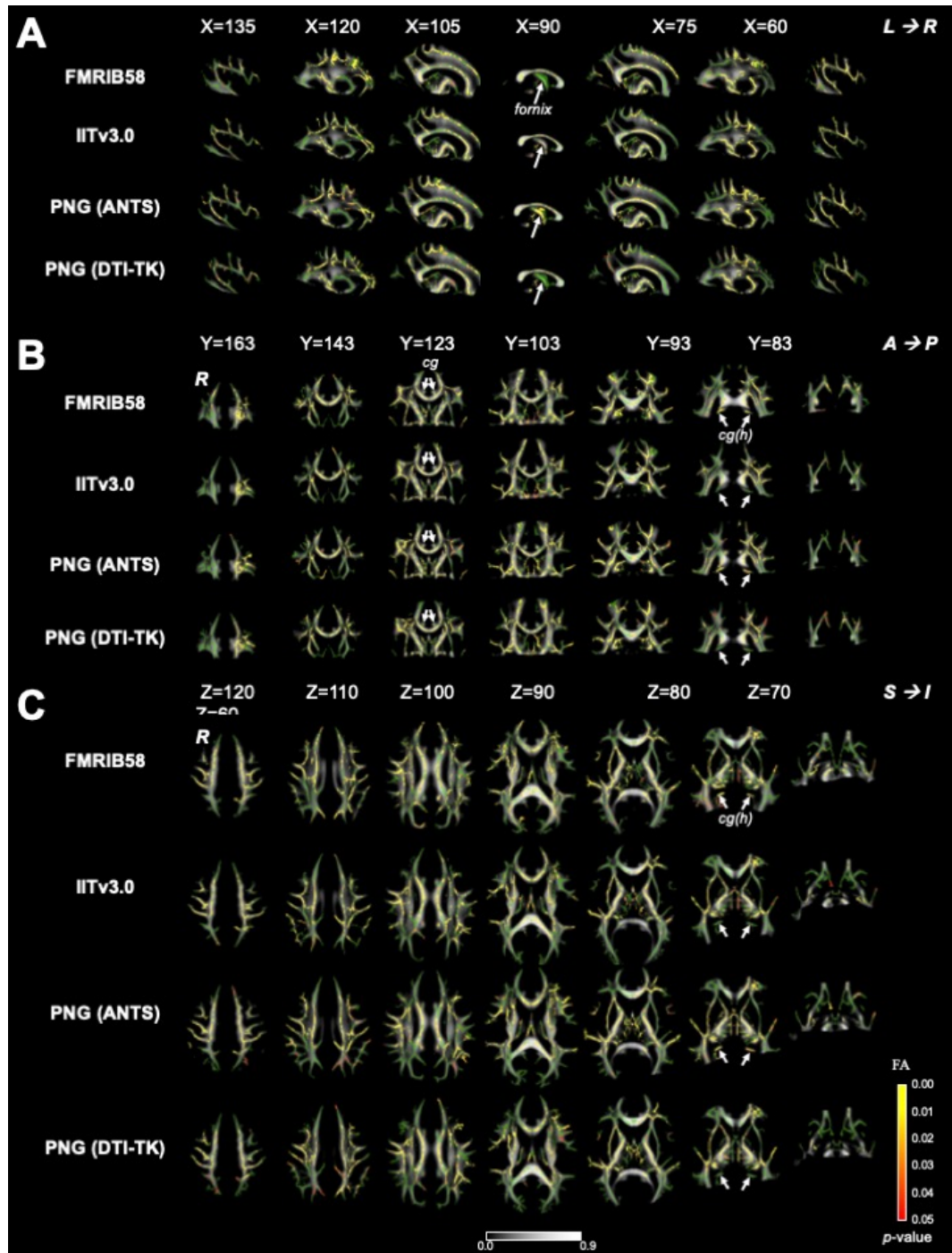
Fig. 2.6. Illustrations of t-statistical maps (red-yellow, FWE corrected, $p < 0.05$) showing decreased FA at *In2* vs. *Pre* in (**A**) sagittal, (**B**) coronal, and (**C**) axial views, overlaid on TBSS skeleton (green) and mean FA image derived from FMRIB58 (FMRIB, Oxford, UK), IITv3.0 [125], PNG (ANTs), and PNG (DTI-TK) DTI templates respectively. Major white matter tracts showing different sensitivity across the templates for detecting FA changes are highlighted in arrows. *cg*: cingula. *cg(h)*: cingula (hippocampi). *L/R*: left/right hemisphere. *A/P*: anterior/posterior. *S/I*: superior/inferior.

27
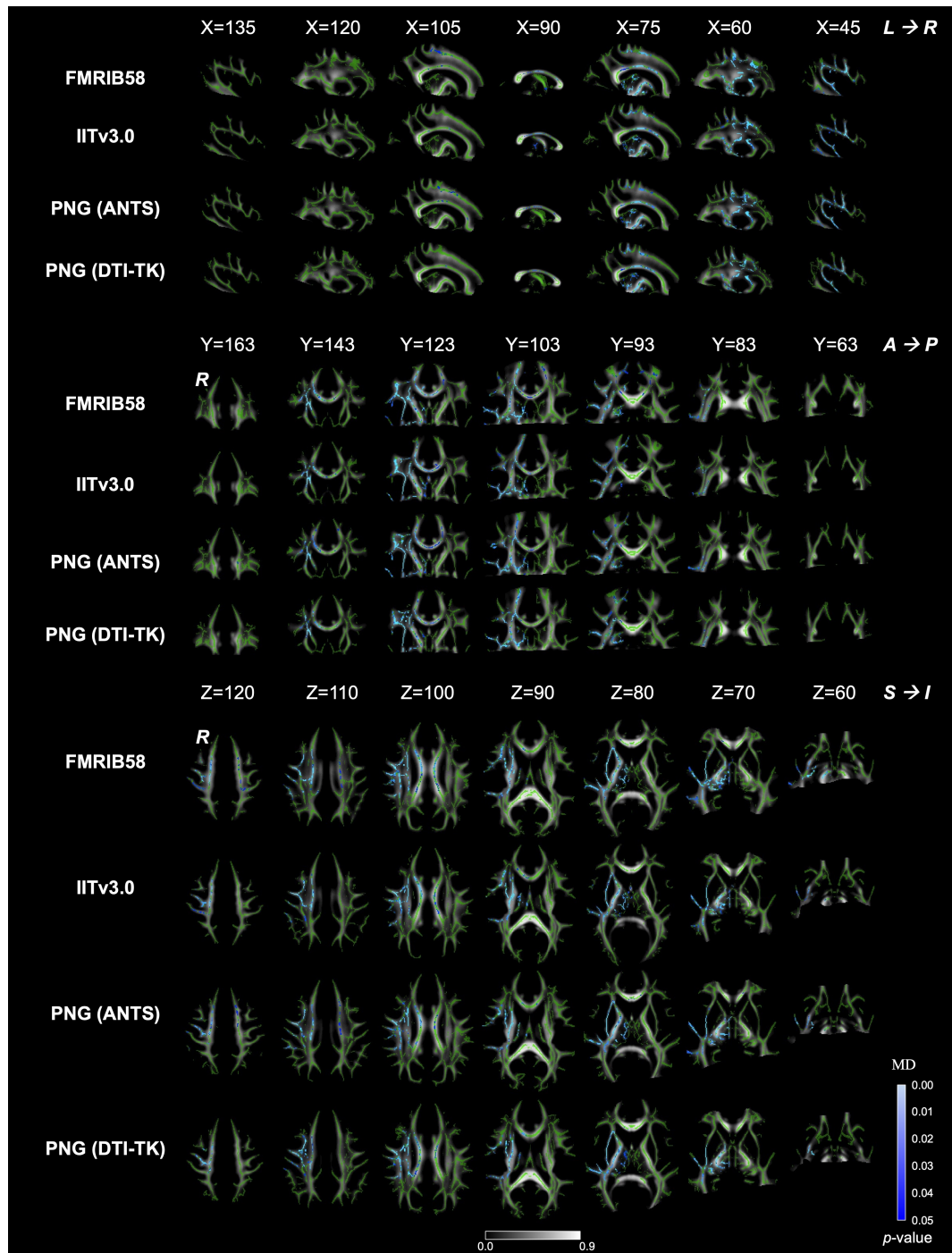
Fig. 2.7. Illustrations of t-statistical maps (blue-lightblue, FWE corrected, $p < 0.05$) showing increased MD at *In2* vs. *Pre* in sagittal, coronal, and axial views, overlaid on TBSS skeleton (green) and mean FA image derived from FMRIB58, IITv3.0, PNG (ANTs), and PNG (DTI-TK) DTI templates respectively. *L/R*: left/right hemisphere. *A/P*: anterior/posterior. *S/I*: superior/inferior.
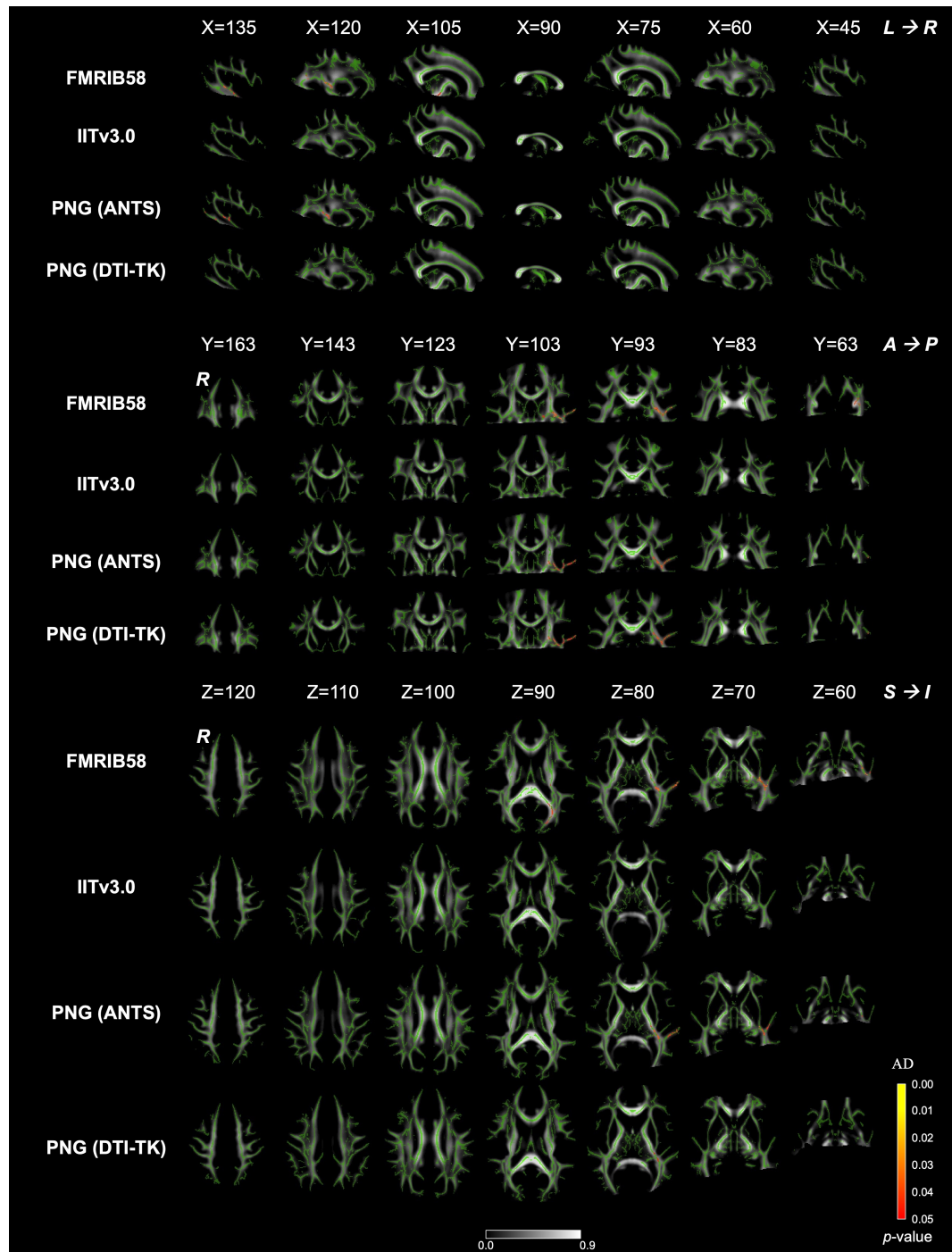
Fig. 2.8. Illustrations of t-statistical maps (red-yellow, FWE corrected, $p < 0.05$) showing decreased AD at $In2$ vs. Pre in sagittal, coronal, and axial views, overlaid on TBSS skeleton (green) and mean FA image derived from FMRIB58, IITv3.0, PNG (ANTs), and PNG (DTI-TK) DTI templates respectively. L/R: left/right hemisphere. A/P: anterior/posterior. S/I: superior/inferior.
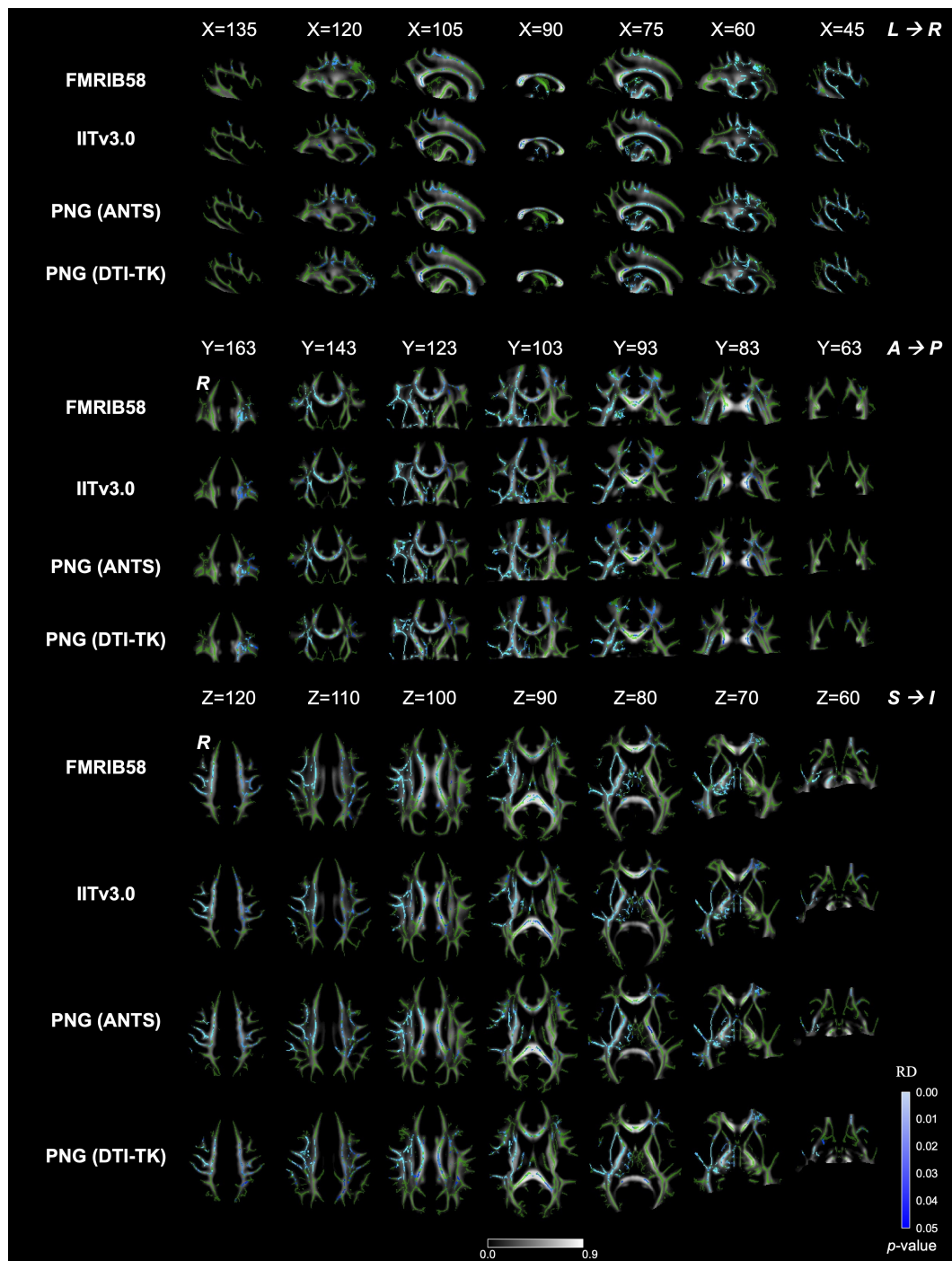
Fig. 2.9. Illustrations of t-statistical maps (blue-lightblue, FWE corrected, $p < 0.05$) showing increased RD at $In2$ vs. Pre in sagittal, coronal, and axial views, overlaid on TBSS skeleton (green) and mean FA image derived from FMRIB58, IITv3.0, PNG (ANTs), and PNG (DTI-TK) DTI templates respectively. L/R: left/right hemisphere. A/P: anterior/posterior. S/I: superior/inferior.

Table 2.6.

Summary of the number of statistically significant voxels that exhibit lower FA at *In2* vs. *Pre* (numerator), with respect to the corresponding total number of voxels within each ROI (denominator), for the standardized and population-specific DTI templates. L/R: Left/right hemisphere.

ROI	FMRIB58	IITv3.0	PNG (ANTs)	PNG (DTI-TK)
Cereral peduncle L (cpL)	188/247	178/230	199/244	185/240
Cereral peduncle R (cpR)	230/283	189/249	229/271	205/253
Cingulum (cingulate gyrus) L (cgL)	221/487	126/278	116/320	5/213
Cingulum (cingulate gyrus) R (cgR)	32/422	106/252	108/251	6/111
Superior corona radiata L (scrL)	841/1234	892/1318	932/1370	946/1345
Superior corona radiata R (scrR)	1182/1323	1225/1369	1260/1387	1200/1363
Anterior corona radiata L (acrL)	874/1546	868/1583	828/1583	836/1589
Anterior corona radiata R (acrR)	499/1504	414/1628	374/1635	368/1633
Posterior corona radiata L (pcrL)	425/741	381/695	319/683	285/687
Posterior corona radiata R (pcrR)	324/818	292/820	278/859	257/819
Body of corpus callosum (bcc)	2057/3142	2180/3182	2256/3295	2188/3360
Genu of corpus callosum (bcc)	907/1743	935/1823	933/1696	878/1786
Splenium of corpus callosum (bcc)	1717/2528	1389/2278	1383/2397	1321/2397
External capsule L (ecL)	166/1353	123/1351	93/1287	102/1340
External capsule R (ecR)	858/1239	809/1240	850/1162	818/1244
Fornix (fx)	14/162	88/142	99/162	13/168
Cingulum (hippocampus) L [cg(h)L]	25/60	2/14	24/42	0/53
Cingulum (hippocampus) R [cg(h)R]	86/110	0/44	63/77	0/81
Ilf/Ifof L	96/241	75/183	91/185	87/205
Ilf/Ifof R	270/334	186/279	205/258	161/225
Anterior limb of internal capsule L (alicL)	381/776	355/703	337/729	345/735
Anterior limb of internal capsule R (alicR)	550/786	554/771	509/725	536/760
Posterior limb of internal capsule L (plicL)	576/859	641/853	650/857	703/862
Posterior limb of internal capsule R (plicR)	690/858	659/835	713/855	744/872
Retrolenticular part of internal capsule L (rlicL)	468/782	421/796	525/795	525/793
Retrolenticular part of internal capsule R (rlicR)	615/767	611/774	664/768	639/759
Posterior thalamic radiation L (ptrL)	265/991	182/881	174/755	152/763
Posterior thalamic radiation R (ptrR)	484/1101	192/969	309/912	155/872
Fornix (cres)/stria terminalis L (fx/stL)	221/316	133/174	185/249	177/239
Fornix (cres)/stria terminalis R (fx/stR)	274/288	129/132	221/227	216/223
Superior fronto-occipital fasciculus L (sfofL)	28/93	57/114	52/117	52/112
Superior fronto-occipital fasciculus R (sfofR)	62/98	83/112	88/113	95/112
Superior longitudinal fasciculus L (slfL)	478/1332	714/1694	640/1662	716/1769
Superior longitudinal fasciculus R (slfR)	765/1402	833/1640	1030/1702	892/1760
Tapetum L (ttL)	0/2	10/15	20/29	30/54
Tapetum R (ttR)	5/20	3/22	15/54	19/78
Uncinate fasciculus L (ufL)	0/16	0/28	0/10	0/6
Uncinate fasciculus R (ufR)	11/13	5/10	13/17	7/7
Total	16885/30017	16040/29481	16785/29740	15864/29888

Table 2.7.

Summary of the number of statistically significant voxels that exhibit higher MD at *In2* vs. *Pre* (numerator), with respect to the corresponding total number of voxels within each ROI (denominator), for the standardized and population-specific DTI templates. L/R: Left/right hemisphere.

ROI	FMRIB58	IITv3.0	PNG (ANTs)	PNG (DTI-TK)
Cereral peduncle L (cpL)	0/247	0/230	0/244	0/240
Cereral peduncle R (cpR)	185/283	135/249	168/271	143/253
Cingulum (cingulate gyrus) L (cgL)	0/487	22/278	0/320	0/213
Cingulum (cingulate gyrus) R (cgR)	216/422	99/252	0/251	0/111
Superior corona radiata L (scrL)	137/1234	5/1318	107/1370	5/1345
Superior corona radiata R (scrR)	1014/1323	1089/1369	1072/1387	1098/1363
Anterior corona radiata L (acrL)	0/1546	0/1583	7/1583	0/1589
Anterior corona radiata R (acrR)	309/1504	322/1628	294/1635	290/1633
Posterior corona radiata L (pcrL)	8/741	0/695	0/683	0/687
Posterior corona radiata R (pcrR)	204/818	170/820	168/859	186/819
Body of corpus callosum (bcc)	1225/3142	1104/3182	955/3295	1025/3360
Genu of corpus callosum (bcc)	312/1743	154/1823	324/1696	186/1786
Splenium of corpus callosum (bcc)	73/2528	22/2278	53/2397	52/2397
External capsule L (ecL)	0/1353	0/1351	0/1287	0/1340
External capsule R (ecR)	843/1239	842/1240	821/1162	805/1244
Fornix (fx)	0/162	44/142	2/162	0/168
Cingulum (hippocampus) L [cg(h)L]	0/60	0/14	0/42	0/53
Cingulum (hippocampus) R [cg(h)R]	0/110	0/44	0/77	0/81
Ilf/Ifof L	0/241	0/183	0/185	0/205
Ilf/Ifof R	229/334	169/279	178/258	152/225
Anterior limb of internal capsule L (alicL)	0/776	0/703	0/729	0/735
Anterior limb of internal capsule R (alicR)	518/786	465/771	460/725	473/760
Posterior limb of internal capsule L (plicL)	0/859	0/853	0/857	0/862
Posterior limb of internal capsule R (plicR)	703/858	669/835	680/855	725/872
Retrolenticular part of internal capsule L (rlicL)	0/782	0/796	0/795	0/793
Retrolenticular part of internal capsule R (rlicR)	409/767	385/774	376/768	362/759
Posterior thalamic radiation L (ptrL)	0/991	0/881	0/755	0/763
Posterior thalamic radiation R (ptrR)	123/1101	103/969	93/912	99/872
Fornix (cres)/stria terminalis L (fx/stL)	0/316	0/174	0/249	0/239
Fornix (cres)/stria terminalis R (fx/stR)	180/288	63/132	136/227	130/223
Superior fronto-occipital fasciculus L (sfofL)	0/93	0/114	0/117	0/112
Superior fronto-occipital fasciculus R (sfofR)	78/98	99/112	93/113	76/112
Superior longitudinal fasciculus L (slfL)	0/1332	0/1694	0/1662	0/1769
Superior longitudinal fasciculus R (slfR)	762/1402	821/1640	834/1702	861/1760
Tapetum L (ttL)	0/2	0/15	0/29	0/54
Tapetum R (ttR)	3/20	0/22	0/54	0/78
Uncinate fasciculus L (ufL)	0/16	0/28	0/10	0/6
Uncinate fasciculus R (ufR)	13/13	9/10	17/17	7/7
Total	7544/30017	6791/29481	6838/29740	6675/29888

Table 2.8.

Summary of the number of statistically significant voxels that exhibit lower AD at *In2* vs. *Pre* (numerator), with respect to the corresponding total number of voxels within each ROI (denominator), for the standardized and population-specific DTI templates. L/R: Left/right hemisphere.

ROI	FMRIB58	IITv3.0	PNG (ANTs)	PNG (DTI-TK)
Cereral peduncle L (cpL)	109/247	0/230	0/244	0/240
Cereral peduncle R (cpR)	0/283	0/249	0/271	0/253
Cingulum (cingulate gyrus) L (cgL)	0/487	0/278	0/320	0/213
Cingulum (cingulate gyrus) R (cgR)	0/422	0/252	0/251	0/111
Superior corona radiata L (scrL)	0/1234	0/1318	0/1370	0/1345
Superior corona radiata R (scrR)	0/1323	0/1369	0/1387	0/1363
Anterior corona radiata L (acrL)	0/1546	0/1583	0/1583	0/1589
Anterior corona radiata R (acrR)	0/1504	0/1628	0/1635	0/1633
Posterior corona radiata L (pcrL)	35/741	0/695	0/683	0/687
Posterior corona radiata R (pcrR)	0/818	0/820	0/859	0/819
Body of corpus callosum (bcc)	0/3142	0/3182	0/3295	0/3360
Genu of corpus callosum (bcc)	0/1743	0/1823	0/1696	0/1786
Splenium of corpus callosum (bcc)	67/2528	0/2278	0/2397	0/2397
External capsule L (ecL)	63/1353	0/1351	40/1287	0/1340
External capsule R (ecR)	0/1239	0/1240	0/1162	0/1244
Fornix (fx)	0/162	0/142	0/162	0/168
Cingulum (hippocampus) L [cg(h)L]	0/60	0/14	0/42	0/53
Cingulum (hippocampus) R [cg(h)R]	0/110	0/44	0/77	0/81
Ilf/Ifof L	57/241	0/183	75/185	0/205
Ilf/Ifof R	0/334	0/279	0/258	0/225
Anterior limb of internal capsule L (alicL)	0/776	0/703	0/729	0/735
Anterior limb of internal capsule R (alicR)	0/786	0/771	0/725	0/760
Posterior limb of internal capsule L (plicL)	48/859	0/853	23/857	0/862
Posterior limb of internal capsule R (plicR)	0/858	0/835	0/855	0/872
Retrolenticular part of internal capsule L (rlicL)	389/782	0/796	402/795	95/793
Retrolenticular part of internal capsule R (rlicR)	0/767	0/774	0/768	0/759
Posterior thalamic radiation L (ptrL)	100/991	0/881	26/755	5/763
Posterior thalamic radiation R (ptrR)	0/1101	0/969	0/912	0/872
Fornix (cres)/stria terminalis L (fx/stL)	16/316	0/174	5/249	0/239
Fornix (cres)/stria terminalis R (fx/stR)	0/288	0/132	0/227	0/223
Superior fronto-occipital fasciculus L (sfofL)	0/93	0/114	0/117	0/112
Superior fronto-occipital fasciculus R (sfofR)	0/98	0/112	0/113	0/112
Superior longitudinal fasciculus L (slfL)	0/1332	0/1694	0/1662	0/1769
Superior longitudinal fasciculus R (slfR)	0/1402	0/1640	0/1702	0/1760
Tapetum L (ttL)	0/2	0/15	0/29	0/54
Tapetum R (ttR)	0/20	0/22	0/54	0/78
Uncinate fasciculus L (ufL)	4/16	0/28	0/10	0/6
Uncinate fasciculus R (ufR)	0/13	0/10	0/17	0/7
Total	888/30017	0/29481	571/29740	100/29888

Table 2.9.
Summary of the number of statistically significant voxels that exhibit higher RD at *In2* vs. *Pre* (numerator), with respect to the corresponding total number of voxels within each ROI (denominator), for the standardized and population-specific DTI templates. L/R: Left/right hemisphere.

ROI	FMRIB58	IITv3.0	PNG (ANTs)	PNG (DTI-TK)
Cereral peduncle L (cpL)	0/247	0/230	0/244	0/240
Cereral peduncle R (cpR)	237/283	185/249	223/271	192/253
Cingulum (cingulate gyrus) L (cgL)	229/487	121/278	139/320	52/213
Cingulum (cingulate gyrus) R (cgR)	227/422	112/252	125/251	4/111
Superior corona radiata L (scrL)	569/1546	513/1583	445/1583	597/1589
Superior corona radiata R (scrR)	419/1504	391/1628	404/1635	407/1633
Anterior corona radiata L (acrL)	122/741	105/695	127/683	111/687
Anterior corona radiata R (acrR)	236/818	260/820	256/859	244/819
Posterior corona radiata L (pcrL)	373/1234	457/1318	302/1370	511/1345
Posterior corona radiata R (pcrR)	1206/1323	1285/1369	1296/1387	1249/1363
Body of corpus callosum (bcc)	1792/3142	1804/3182	1873/3295	1901/3360
Genu of corpus callosum (bcc)	690/1743	702/1823	677/1696	689/1786
Splenium of corpus callosum (bcc)	1227/2528	1024/2278	1099/2397	1017/2397
External capsule L (ecL)	39/1353	34/1351	0/1287	22/1340
External capsule R (ecR)	933/1239	943/1240	929/1162	959/1244
Fornix (fx)	19/162	75/142	7/162	0/168
Cingulum (hippocampus) L [cg(h)L]	0/60	0/14	0/42	0/53
Cingulum (hippocampus) R [cg(h)R]	0/110	0/44	0/77	0/81
Ilf/Ifof L	0/241	0/183	0/185	0/205
Ilf/Ifof R	282/334	204/279	205/258	175/225
Anterior limb of internal capsule L (alicL)	0/776	0/703	0/729	0/735
Anterior limb of internal capsule R (alicR)	583/786	563/771	532/725	539/760
Posterior limb of internal capsule L (plicL)	0/859	80/853	111/857	0/862
Posterior limb of internal capsule R (plicR)	719/858	707/835	727/855	773/872
Retrolenticular part of internal capsule L (rlicL)	67/782	0/796	124/795	2/793
Retrolenticular part of internal capsule R (rlicR)	584/767	571/774	622/768	600/759
Posterior thalamic radiation L (ptrL)	112/991	53/881	64/755	3/763
Posterior thalamic radiation R (ptrR)	197/1101	220/969	157/912	214/872
Fornix (cres)/stria terminalis L (fx/stL)	0/316	0/174	0/249	0/239
Fornix (cres)/stria terminalis R (fx/stR)	260/288	118/132	209/227	199/223
Superior fronto-occipital fasciculus L (sfofL)	0/93	0/114	0/117	0/112
Superior fronto-occipital fasciculus R (sfofR)	87/98	107/112	105/113	99/112
Superior longitudinal fasciculus L (slfL)	169/1332	69/1694	250/1662	295/1769
Superior longitudinal fasciculus R (slfR)	840/1402	877/1640	1046/1702	1001/1760
Tapetum L (ttL)	0/2	5/15	9/29	11/54
Tapetum R (ttR)	4/20	3/22	13/54	16/78
Uncinate fasciculus L (ufL)	0/16	0/28	0/10	0/6
Uncinate fasciculus R (ufR)	13/13	10/10	17/17	7/7
Total	12235/30017	11598/29481	12093/29740	11889/29888

Table 2.10.

Summary of linear mixed-effect regression analyses of the longitudinal FA changes during a single season. L/R: Left/right hemisphere.

ROI	Template	AIC	$t_{\text{Timepoint}}$	$p_{\text{Timepoint}}$	ROI	Template	AIC	$t_{\text{Timepoint}}$	$p_{\text{Timepoint}}$
Cerebral peduncle L	FMRIB58	-999.006	-3.933	<0.001	Internal capsule - anterior R	FMRIB58	-893.710	-3.600	<0.001
Cerebral peduncle L	IITv3.0	-965.835	-4.022	<0.001	Internal capsule - anterior R	IITv3.0	-897.371	-4.006	<0.001
Cerebral peduncle L	PNG (ANTs)	-973.708	-3.951	<0.001	Internal capsule - anterior R	PNG (ANTs)	-890.680	-3.790	<0.001
Cerebral peduncle L	PNG (DTI-TK)	-957.593	-3.832	<0.001	Internal capsule - anterior R	PNG (DTI-TK)	-888.374	-3.921	<0.001
Cingulum R	FMRIB58	-700.252	-2.424	0.017	Internal capsule - posterior R	FMRIB58	-963.365	-3.631	<0.001
Cingulum R	IITv3.0	-842.960	-3.613	<0.001	Internal capsule - posterior R	IITv3.0	-940.976	-3.519	0.001
Cingulum R	PNG (ANTs)	-807.769	-3.089	0.002	Internal capsule - posterior R	PNG (ANTs)	-936.896	-3.512	0.001
Cingulum R	PNG (DTI-TK)	-503.286	-1.590	0.114	Internal capsule - posterior R	PNG (DTI-TK)	-934.373	-3.565	0.001
Corona radiata - anterior L	FMRIB58	-949.874	-5.608	<0.001	Ilf/Ifof L	FMRIB58	-803.620	-3.122	0.002
Corona radiata - anterior L	IITv3.0	-965.638	-5.730	<0.001	Ilf/Ifof L	IITv3.0	-756.940	-2.823	0.006
Corona radiata - anterior L	PNG (ANTs)	-950.563	-5.427	<0.001	Ilf/Ifof L	PNG (ANTs)	-782.879	-2.949	0.004
Corona radiata - anterior L	PNG (DTI-TK)	-938.728	-5.380	<0.001	Ilf/Ifof L	PNG (DTI-TK)	-773.210	-2.870	0.005
Corona radiata - anterior R	FMRIB58	-909.229	-4.273	<0.001	Stria terminalis L	FMRIB58	-762.923	-2.749	0.007
Corona radiata - anterior R	IITv3.0	-910.472	-4.359	<0.001	Stria terminalis L	IITv3.0	-779.923	-3.256	0.001
Corona radiata - anterior R	PNG (ANTs)	-885.240	-3.761	<0.001	Stria terminalis L	PNG (ANTs)	-770.464	-2.895	0.004
Corona radiata - anterior R	PNG (DTI-TK)	-915.480	-3.729	<0.001	Stria terminalis L	PNG (DTI-TK)	-758.315	-2.880	0.005
Corona radiata - posterior L	FMRIB58	-984.764	-3.561	0.001	Superior fronto-occipital fasciculus R	FMRIB58	-815.550	-2.341	0.021
Corona radiata - posterior L	IITv3.0	-936.434	-3.208	0.002	Superior fronto-occipital fasciculus R	IITv3.0	-828.499	-2.756	0.007
Corona radiata - posterior L	PNG (ANTs)	-949.140	-2.919	0.004	Superior fronto-occipital fasciculus R	PNG (ANTs)	-857.783	-2.601	0.010
Corona radiata - posterior L	PNG (DTI-TK)	-948.283	-3.060	0.003	Superior fronto-occipital fasciculus R	PNG (DTI-TK)	-800.028	-2.527	0.013
Corona radiata - superior L	FMRIB58	-1001.893	-3.744	<0.001	Superior fronto-occipital fasciculus L	FMRIB58	-867.900	-2.153	0.033
Corona radiata - superior L	IITv3.0	-1006.359	-3.888	<0.001	Superior fronto-occipital fasciculus L	IITv3.0	-875.889	-2.657	0.009
Corona radiata - superior L	PNG (ANTs)	-1015.911	-4.134	<0.001	Superior fronto-occipital fasciculus L	PNG (ANTs)	-900.604	-2.504	0.014
Corona radiata - superior L	PNG (DTI-TK)	-1016.414	-4.144	<0.001	Superior fronto-occipital fasciculus L	PNG (DTI-TK)	-854.079	-2.480	0.014
Corona radiata - superior R	FMRIB58	-976.167	-4.211	<0.001	Superior longitudinal fasciculus L	FMRIB58	-971.099	-3.546	0.001
Corona radiata - superior R	IITv3.0	-974.193	-4.117	<0.001	Superior longitudinal fasciculus L	IITv3.0	-996.790	-4.505	<0.001
Corona radiata - superior R	PNG (ANTs)	-976.064	-4.314	<0.001	Superior longitudinal fasciculus L	PNG (ANTs)	-980.142	-4.146	<0.001
Corona radiata - superior R	PNG (DTI-TK)	-966.943	-4.117	<0.001	Superior longitudinal fasciculus L	PNG (DTI-TK)	-1004.102	-4.592	<0.001
External capsule R	FMRIB58	-978.784	-3.761	<0.001	Superior longitudinal fasciculus R	FMRIB58	-902.519	-3.357	0.001
External capsule R	IITv3.0	-966.536	-3.966	<0.001	Superior longitudinal fasciculus R	IITv3.0	-882.844	-3.333	0.001
External capsule R	PNG (ANTs)	-973.989	-3.771	<0.001	Superior longitudinal fasciculus R	PNG (ANTs)	-904.064	-3.397	0.001
External capsule R	PNG (DTI-TK)	-959.332	-3.905	<0.001	Superior longitudinal fasciculus R	PNG (DTI-TK)	-892.056	-3.408	0.001
Internal capsule - anterior L	FMRIB58	-997.917	-4.395	<0.001					
Internal capsule - anterior L	IITv3.0	-983.458	-4.613	<0.001					
Internal capsule - anterior L	PNG (ANTs)	-969.372	-4.228	<0.001					
Internal capsule - anterior L	PNG (DTI-TK)	-975.600	-4.363	<0.001					
	(cont.)								

Table 2.11.

Summary of linear mixed-effect regression analyses of the longitudinal MD changes during a single season. L/R: Left/right hemisphere.

ROI	Template	AIC	$t_{\text{Timepoint}}$	$p_{\text{Timepoint}}$
Corona radiata - superior L	FMRIB58	-3540.243	2.901	0.004
Corona radiata - superior L	IITv3.0	-3397.201	1.620	0.108
Corona radiata - superior L	PNG (ANTs)	-3531.498	2.907	0.004
Corona radiata - superior L	PNG (DTI-TK)	-3379.134	1.812	0.072
Corona radiata - posterior R	FMRIB58	-3519.733	3.933	<0.001
Corona radiata - posterior R	IITv3.0	-3513.535	4.119	<0.001
Corona radiata - posterior R	PNG (ANTs)	-3516.493	3.991	<0.001
Corona radiata - posterior R	PNG (DTI-TK)	-3526.663	4.227	<0.001
External capsule R	FMRIB58	-3442.098	3.672	<0.001
External capsule R	IITv3.0	-3432.47	3.605	<0.001
External capsule R	PNG (ANTs)	-3434.88	3.625	<0.001
External capsule R	PNG (DTI-TK)	-3427.17	3.626	<0.001
Internal capsule - anterior R	FMRIB58	-3486.412	4.128	<0.001
Internal capsule - anterior R	IITv3.0	-3490.873	4.339	<0.001
Internal capsule - anterior R	PNG (ANTs)	-3489.208	4.291	<0.001
Internal capsule - anterior R	PNG (DTI-TK)	-3481.104	4.353	<0.001
Internal capsule - retrolenticular R	FMRIB58	-3496.76	3.524	0.001
Internal capsule - retrolenticular R	IITv3.0	-3483.141	3.648	<0.001
Internal capsule - retrolenticular R	PNG (ANTs)	-3497.656	3.622	<0.001
Internal capsule - retrolenticular R	PNG (DTI-TK)	-3491.496	3.481	0.001
Posterior thalamic radiation R	FMRIB58	-3292.574	3.475	0.001
Posterior thalamic radiation R	IITv3.0	-3286.593	3.504	0.001
Posterior thalamic radiation R	PNG (ANTs)	-3289.02	3.581	<0.001
Posterior thalamic radiation R	PNG (DTI-TK)	-3289.954	3.432	0.001
Stria terminalis R	FMRIB58	-3400.108	3.900	<0.001
Stria terminalis R	IITv3.0	-3360.821	4.016	<0.001
Stria terminalis R	PNG (ANTs)	-3391.484	4.221	<0.001
Stria terminalis R	PNG (DTI-TK)	-3393.781	4.121	<0.001

Table 2.12.

Summary of linear mixed-effect regression analyses of the longitudinal RD changes during a single season. L/R: Left/right hemisphere.

ROI	Template	AIC	$t_{\text{Timepoint}}$	$p_{\text{Timepoint}}$
Corona radiata - anterior L	FMRIB58	-3428.679	3.485	0.001
Corona radiata - anterior L	IITv3.0	-3425.700	3.424	0.001
Corona radiata - anterior L	PNG (ANTs)	-3423.187	3.378	0.001
Corona radiata - anterior L	PNG (DTI-TK)	-3445.185	3.519	0.001
Corona radiata - posterior L	FMRIB58	-3504.331	3.278	0.001
Corona radiata - posterior L	IITv3.0	-3534.104	3.353	0.001
Corona radiata - posterior L	PNG (ANTs)	-3524.536	2.962	0.004
Corona radiata - posterior L	PNG (DTI-TK)	-3521.961	3.226	0.002
Corona radiata - posterior R	FMRIB58	-3458.142	3.595	¡0.001
Corona radiata - posterior R	IITv3.0	-3491.897	3.634	¡0.001
Corona radiata - posterior R	PNG (ANTs)	-3478.747	3.543	0.001
Corona radiata - posterior R	PNG (DTI-TK)	-3478.698	3.678	¡0.001
Corona radiata - superior L	FMRIB58	-3541.785	3.433	0.001
Corona radiata - superior L	IITv3.0	-3557.260	3.209	0.002
Corona radiata - superior L	PNG (ANTs)	-3527.164	3.132	0.002
Corona radiata - superior L	PNG (DTI-TK)	-3573.729	3.386	0.001
Corona radiata - superior R	FMRIB58	-3530.146	3.637	¡0.001
Corona radiata - superior R	IITv3.0	-3525.039	3.624	¡0.001
Corona radiata - superior R	PNG (ANTs)	-3520.918	3.709	¡0.001
Corona radiata - superior R	PNG (DTI-TK)	-3510.795	3.691	¡0.001
Cingulum R	FMRIB58	-3418.196	3.696	¡0.001
Cingulum R	IITv3.0	-3449.840	4.119	¡0.001
Cingulum R	PNG (ANTs)	-3409.712	3.802	¡0.001
Cingulum R	PNG (DTI-TK)	-3076.682	2.334	0.021
External capsule R	FMRIB58	-3441.819	3.673	¡0.001
External capsule R	IITv3.0	-3430.025	3.626	¡0.001
External capsule R	PNG (ANTs)	-3435.033	3.640	¡0.001
External capsule R	PNG (DTI-TK)	-3438.866	3.679	¡0.001
Internal capsule - posterior R	FMRIB58	-3523.569	3.928	¡0.001
Internal capsule - posterior R	IITv3.0	-3505.418	3.850	¡0.001
Internal capsule - posterior R	PNG (ANTs)	-3492.866	3.860	¡0.001
Internal capsule - posterior R	PNG (DTI-TK)	-3490.177	3.804	¡0.001
Internal capsule - retrolenticular R	FMRIB58	-3448.227	3.659	¡0.001
Internal capsule - retrolenticular R	IITv3.0	-3444.532	3.594	¡0.001
Internal capsule - retrolenticular R	PNG (ANTs)	-3454.165	3.501	0.001
Internal capsule - retrolenticular R	PNG (DTI-TK)	-3439.085	3.285	0.001
Superior longitudinal fasciculus L	FMRIB58	-3546.147	3.125	0.002
Superior longitudinal fasciculus L	IITv3.0	-3506.088	3.064	0.003
Superior longitudinal fasciculus L	PNG (ANTs)	-3535.539	2.973	0.004
Superior longitudinal fasciculus L	PNG (DTI-TK)	-3561.371	3.435	0.001

2.6 Discussion

Due to repetitive head impacts experienced during practices and games, EMA collision-sport athletes may exhibit a distinct neurological trajectory that is different from those typical at the same age. Bias may be introduced when modeling the neurological consequences using the existing standardized human brain atlases based on healthy adult or adolescent populations, leading to confounding (sometimes even contradictory) findings. In this work, population-specific brain atlases were developed for EMA collision-sport athletes in the PNG longitudinal database. Compared to the standardized adult or other age-appropriate T1 templates (Fig. 2.2), significantly fewer biases were introduced in spatial normalization using PNG T1 template (Fig. 2.4). The PNG (ANTs) DTI template resulted in minimal biases compared to the standardized or PNG (DTI-TK) DTI templates (Table 2.3, Fig. 2.5), and the selection contributed to different sensitivity of detecting DTI changes in TBSS (Tables 2.5 2.6, 2.7, 2.8, and 2.9; Figs. 2.6, 2.7, 2.8, and 2.9), whereas the sensitivity of detecting longitudinal change of DTI metrics from ROI-based regression analyses was relatively comparable (Tables 2.10, 2.11, and 2.12). In summary, the main findings suggested that the brain atlases better characterized the neuroanatomy of EMA collision-sport athletes, reduced biases introduced during spatial normalization, and exhibited higher sensitivity in detecting regional DTI differences. As template selection is a critical strategic step towards robust and rigorous statistical findings, we expect neuroimaging and clinical researchers will benefit from the proposed atlases to better clarify mechanisms of mTBI and monitor brain health of EMA collision-sport athletes.

The strengths and limitations between standardized and population-specific brain atlas have been discussed [117, 120]. Being a pragmatic option for computational efficiency, a standardized brain atlas often comes with a comprehensive set of templates and semantic labels, facilitating the processing and analysis of brain images acquired from multiple sites or studies [120]. However, when the underlying neuroanatomy of the study population is different, mis-registration can lead to greater bias and errors in voxel-wise and ROI-based statistical analysis. On the other hand, the registration errors of using a population-specific template are unbiased towards the study population; however, the template usually lacks semantic labels [117]; therefore, subsequent transformation to a standard space (e.g., ICBM152) is required for interpreting the statistical maps [185]. In addition, suboptimal data quality can lead to a poorly constructed template and lowers spatial normalization accuracy [120, 125, 186], so a nontrivial amount of diligence is demanded in constructing population-specific templates. The selection strategy largely depends on the specific study, including research questions to address, participants of the study, as well as the number, type, and quality of data [117]. Neuroimaging researchers working on clinical populations should carefully leverage these aspects to ensure rigorous and robust neuroimaging findings are reported in clinical literature and be cautious when reporting voxel-wise statistical findings based off of non-specific brain atlas.

This work clarified the advantages and limitations of constructing population-specific DTI templates (Fig. 2.2B) using scalar-based (ANTs) and tensor-based (DTI-TK) registrations. Conventionally, spatial normalization of diffusion tensor fields is achieved by aligning the b_0 image to the anatomical T1 image [187], and our evaluation showed that this approach introduced minimal biases in spatial normalization (Table 2.3, Fig. 2.5). ANTs is a diffeomorphic registration that uses cross-correlation metrics to optimize the shape and

appearance during template construction, with the underlying assumption that possibly different shapes of the same structures exist in both images [171]; as a result, the PNG (ANTs) template has a sharp appearance that can discern adjacent white matter tracts. Unlike ANTs, DTI-TK utilizes the six tensor components and does not include such template update procedures, and the PNG (DTI-TK) template was computed as the average of the co-registered dataset. Although the appearance was more blurred than the PNG (ANTs) template, adjacent white matter tracts can be discerned. While it is commonly believed that tensor-based registration algorithms improve the registration quality of DTI [185,188–190], the estimates of tensor in certain biological structures (e.g., the fornix) can be not very accurate, which may adversely affect the quality of the constructed template. A combination of tensor information with a scalar-based registration method can potentially improve the quality of a population-specific template [191].

According to the voxel-based morphometric analyses (Fig. 2.4), using the PNG T1 template introduced minimal bias during spatial normalization of the T1 images from the EMA collision-sport athletes, even compared to the $NIHPD_{13.0-18.5}$ template (Fig. 2.4B). Given that the NIHPD template was constructed based on healthy adolescents of similar age range, one explanation is that the trajectory of subcortical volumes in adolescent collision-sport athletes may be different from healthy adolescents of similar ages. Previously, Narvacan et al. [116] reported in a lifespan study of healthy adolescents that at age 13-17, non-linear decrease of subcortical volumes was observed within certain regions for the male participants. It would then comprise a meaningful exploration to see whether the trajectory of subcortical volumes can be driven by sports-related concussion and subconcussive trauma. Notably, future work is needed to validate the T1-based semantic labels (Fig. 2.1A), which may be applied to investigate the regional volumetric trajectory.

The selection of DTI templates did not lead to significantly different TBSS skeleton but was a significant covariate for the voxel-wise statistical analyses (Table 2.4, 2.5, Tables 2.6, 2.7, 2.8, and 2.9). Previously, utilizing the standardized FMRIB58 template in TBSS processing, abnormal DTI changes in 64 adolescent football athletes from *Pre* to *In*2 was observed, including decreased FA, decreased AD, increased MD, and increased RD [166,167]. In this work, compared to FMRIB58, the PNG (ANTs) template resulted in consistent but more sensitive detection of FA decrease within the fornix and bilateral cingula (hippocampi), whereas on the skeletons of IITv3.0 and PNG (DTI-TK), such difference was either detected with fewer voxels or not statistically significant (Fig. 2.6). Fornix and hippocampus are major parts of the limbic system. Surrounded by cerebrospinal fluids, the main body of the fornix is located in the midline of the brain, with neuronal projections to bilateral cingula (hippocampi) in medial temporal lobes. Fornix is critical for normal cognitive functioning; literature reported atrophy in fornix for neurological disorders [192]. The hippocampus consists of gray matter, with a thin layer of white matter on its ventricular surface [193]. Atrophy of hippocampus a common neuropathology in chronic traumatic encephalopathy [194,195]. The volume of bilateral cingula (hippocampi) correlated with FA in the fornix [196], and reduced fornix and hippocampal volumes reported in morphometric study of TBI [197] (for review, see Shenton et al. [198]). Both structures are relatively small and prone to mis-registration in DWI, due to low spatial resolution, geometric distortions from eddy current, and partial volume effects [199–202]. The PNG (ANTs) template potentially provided DTI insights that complemented the volumetric findings and were likely due to subconcussive trauma, to the best of our knowledge, in white matter tracts not pre-

viously observed for this vulnerable population. Consistent with Cabeen et al. [127] that the study template resulted in significantly larger number of voxels in the fornix, the higher sensitivity within these areas was perhaps attributable to the better anatomical alignment in PNG T1 template, which is unbiased towards the study population and better captured anatomical structure than the standardized templates (Fig. 2.2).

This work has several limitations. Considering that our recruited participants were exclusively male football or female soccer players (Table 2.2), we constructed brain atlases only for the combined collision-sport population and not for each sport, but sex differences may exist and warrant future investigation to determine the necessity of having sex-specific brain atlases for collision sports. Subjective bias from observer during the visual quality assessments may negatively impact the quality of the final templates; in the future, quality assessments should be automated, with specific and objective guideline (e.g., in Jang et al. [78]). Template selection is only one out of many aspects in image processing pipeline that contributes to the inconsistent DTI findings reported in mTBI literature; to achieve reproducible and meaningful results, variability in study design, scanning parameters, and analytic techniques should also be considered [144, 203, 204]. The PNG T1 template was constructed using *buildtemplateparallel.sh*, which was found to have an issue of rigid-only registration and later superseded by *antsMultivariateTemplateConstruction.sh*. This could have an impact on the quality of individual templates based on repeated scans (Fig. 2.1A). There are several limitations when using ANTs for template construction [117]: first, due to the differences in acquisition protocols, DWI data often have artifacts such as distortions due to eddy currents, so that mis-registration can occur between b_0 and T1-weighted images. Second, since white matter has rather homogeneous intensity on a T1 image, using the warping of T1 images to guide DTI alignment may lead to mismatch of white matter alignment. This work evaluated the proposed DTI templates using real data and compared to previous findings based on standardized template [166, 167], but a more robust scheme of evaluation is to employ simulated data, with a priori knowledge of the pathology as a ground truth [205]; such a scheme is robust for modeling pathology like multiple sclerosis, where white matter degeneration is well characterized by the corresponding FA reduction [206, 207], but is difficult for sports-related mTBI and subconcussive trauma in adolescents, given the conflicting DTI characterization for axonal pathology in literature [144].

2.7 Conclusion

In summary, we demonstrated that template selection is a critical strategic step towards robust and rigorous findings in voxel-wise analysis. In this work, utilizing a high-throughput high-performance computing workflow that shortened the computation time of template construction, population-specific brain atlases were constructed for EMA collision-sport athletes in the PNG longitudinal database. We compared two population-specific DTI templates constructed using scalar-based (ANTs) and tensor-based (DTI-TK) registration methods respectively. Evaluations of the T1 templates (ICBM152, NIHPD$_{13.0-18.5}$, IITv3.0, PNG T1) showed that during spatial normalization of the images from new participants, minimal changes in morphometry were introduced using the PNG T1 template. We further showed that selection of the DTI templates contributed to different sensitivity in detecting the abnormal DTI changes observed in high school football athletes over a single season; on the TBSS skeletons, voxels of significant FA decrease within the fornix and bilateral cingula

(hippocampi) were either missing or spurious on the standardized (FMRIB58, IITv3.0) and PNG (DTI-TK) templates. Applying the unbiased brain templates can better clarify mechanisms of mTBI and monitor brain health of EMA collision-sport athletes.

2.8   Acknowledgments

3. MONITOR REPETITIVE HEAD IMPACTS ON BRAIN HEALTH OF HIGH SCHOOL MEN'S FOOTBALL AND WOMEN'S SOCCER ACROSS A SINGLE SEASON

3.1 Abstract

Accrual of traumatic brain injury due to repetitive head acceleration events (HAEs) in collision sports has raised growing concerns, yet adolescent athletes continue to participate without prompt and effective preventative strategies. Using diffusion tensor imaging (DTI), we monitored changes of white matter microstructure in high school football (males, $N = 57$) and soccer (females, $N = 13$) athletes across a single season with accompanying head impact monitoring and neurocognitive assessment. Whole-brain tract-based spatial statistics showed widespread decrease of fractional anisotropy (FA) and axial diffusivity (AD), and increase of mean (MD) and radial diffusivity (RD), from preseason to ten weeks in-season. The deficits in FA, MD, and RD persisted to one month post-season, although AD did increase. ROI-based ANCOVA suggested typical white matter maturation as age increase, but individuals with more years of high school experience exhibited lower FA or higher MD than those that had participated for fewer years. For the football athletes, hits with peak translational acceleration over 37 g were sufficient to alter the distributions of DTI changes, and poorer performance of anti-saccade task at one month post-season was associated with higher MD and RD, suggesting that persistent deficits in white matter microstructure may increase vulnerability for inhibitory control. Monitoring HAE exposures in practices and games thus provides a temporal profile for identifying at-risk individuals during the competitive season, informing prompt interventional strategies, therefore preventing persistence of deficits into post-season and preventing the brain and cognitive health of adolescent collision-sport athletes in the long run.

3.2 Keywords

Magnetic Resonance Imaging; Diffusion Tensor Imaging; Subconcussive Trauma; Adolescence; Cognition

3.3 Introduction

In the United States, about 3.8 million cases of sport-related concussion or other forms of traumatic brain injury (TBI) are reported every year [8, 13], with many more milder and untreated brain injuries unaccounted for [7]. One critical aspect of collision sports [208] is the exposure to subconcussive head acceleration events (HAEs) [29], which induce sudden head movement through direct acceleration-deceleration or rotation of the head (a.k.a. slosh effect) that do not necessarily result in easily observable clinical symptoms

[79–81]. Reported head accelerations for American football can exceed 250g and the number of head impacts experienced in a season may range from 200-1900 [82, 208–210].

Adolescent athletes bear a higher rate of head injury and prolonged recovery than the adults [9, 14] and are particularly vulnerable to injury from subconcussive HAEs, because during adolescence, brain and cognition are undergoing a critical period of development [211, 212], with increase in white matter (WM) volume [131, 213, 214] and myelination of axons [146, 215–220]. Over years of practices and competitions, subconcussive HAEs accumulate and may eventually result in cognitive impairments without symptom of concussion [61, 64, 221, 222]. To detect potential structural injury in the brain that requires neurosurgical intervention (e.g., hemorrhage), computed tomography and structural magnetic resonance imaging (MRI) typically are performed, but neither can capture the neurophysiological features of concussions or a milder form of TBI [223].

Diffusion tensor imaging (DTI) is an MRI technique that non-invasively evaluates the WM microstructural integrity [97, 105, 224, 225] and provide sensitivity profiles of water diffusion in pathology [110]. In DTI metrics, fractional anisotropy (FA) is sensitive to the myelination of axons, as well as the size and density of axonal network; mean diffusivity (MD) reflects the overall magnitude of water diffusion in extracellular volume [95, 225, 226]. Normal WM fibers have intact myelin layers and therefore exhibit high FA; lower FA, on the other hand, indicates less directional water diffusion that often suggests demyelination due to neurotrauma, and is typically associated with higher MD [227–229]. Additional DTI metrics include axial diffusivity (AD) and radial diffusivity (RD); evidence in animal studies suggest that AD and RD measures correspond to pathology in axon and myelin respectively [230, 231], where notable decrease of AD typically develops during the acute phase (within the first 2 weeks) of mild TBI (mTBI) [232]. As these metrics reflect fiber organization and myelin changes in the brain, DTI has been applied to detect damage to WM microstructure and provide evidence for TBI and concussion [150, 233–236].

DTI literature of collision-sport athletes mainly addressed adult population [198, 237, 238] and engaged various analytic approaches [144]. For those studied adolescents and utilized voxel-wise or region of interest (ROI) analysis, conflicting differences or changes of DTI metrics were reported. Borich et al. found higher FA and lower diffusivity (MD, AD, and RD) primarily in frontal WM during subacute phase of concussed adolescent athletes, compared to healthy controls [153]. Reduced diffusivity can sustain from subacute to chronic phase for concussed athletes [239, 240], and was observed in healthy athletes across a single football season as well, within widespread WM tracts [157]. On the contrary, Kuzminski et al. did not observe significant voxel of FA changes over a single season of high school football, but the ROI analysis showed decreased FA within the limbic WM tracts [158]. Chun et al. observed increase of the variances of FA changes in several WM tracts over two seasons of high school football, and such increase correlated with subconcussive HAEs [75]. Jang et al. found that for high school football players, more voxels exhibited changes (both increases and decreases) of FA and MD compared to the non-collision sport controls, yet the prolonged exposure to subconcussive HAEs correlated only with the FA decrease and MD increase [78].

Monitoring and characterizing subconcussive impacts to the brain provide a basis for effective preventive strategies [30, 119]. Neuroimaging studies of adolescent athletes who sustained repeated HAEs found structural or functional abnormalities that were related to the total number of HAEs [64, 74, 78] or those events whose peak translational acceleration

(PTA) were at high loads (typically ¿50 g) [63,76,241], and the directionality of DTI changes may depend on whether the exposure was relatively recent (within two weeks) or remote (earlier or throughout the competitive season) [242]. Currently, the preventive strategies being proposed focus on either limiting head impacts [31], such as modifying rules (e.g. stance of the offensive line in American football) and reducing full-contact practice activities [243], or developing helmets better at absorbing energy [31, 244–247]. Although these strategies can effectively lower the amount or magnitude of HAEs, they do not preclude HAEs from accumulating across the season and over years of practices. It is important to recognize that each individual athlete possesses a unique temporal profile of HAE exposure and pertinent impacts to the brain, yet current literature have not addressed when brain injury (or abnormalities) may occur during the season, i.e., when and to what extent shall intervention be imposed to effectively prevent brain injury. Therefore, the purpose of this work is to address how monitoring the brain and behavior of early-to-middle adolescent athletes during the season may inform strategies for preventing post-season deficits. By retrospectively analyzing a DTI dataset in a prospective longitudinal study of high school American football and soccer athletes in the Purdue Neurotrauma Group (PNG) longitudinal MRI database [32], we investigated the DTI changes from preseason to one month after the season ended, a critical time point where the athletes undergo a dynamic process of WM repair after experiencing repetitive HAEs during the competition season [78]. We hypothesized that participants would experience white matter abnormalities during the season, and that the abnormalities would largely persist to one month post-season. Our analyses addressed how the alterations of WM microstructure are associated with the exposure to HAEs and cognitive performance. We postulated the concept of cumulative HAE threshold, such that the white matter health can be monitored during the season on an individual basis, which may benefit at-risk individuals to prevent post-season deficits.

3.4 Methods

3.4.1 Study Population

High school collision-sport athletes, including 57 football (FB) and 13 soccer (SOC) players, participated in PNG longitudinal studies approved by the Biomedical IRB of Purdue's Human Research Protection Program and was carried out in accordance with the Declaration of Helsinki. Before enrolling in the study, written informed consent was obtained from each participant, and subject assent and parental consent were obtained for participants under the age of 18. Demographic information collected from the participants include age, years of high-school experience (YoE), concussion history, status of attention deficit hyperactivity disorder (ADHD), and the racial and ethnic categories (Table 3.1). All participants completed four MRI sessions: one scan up to one month before contact practices began (*Pre*), one scan in the first half of the season (*In*1), one scan in the second half of the season (*In*2), and one scan approx. one month after the end of their competition season (*Post*; Fig. 3.1).

During the period of study, no participant was diagnosed by athletic trainers or team physicians as being concussed. Subject information such as varsity levels, history of concussion, years of experience (YoE), and ethnicity were collected as a part of the study (Table 3.1).
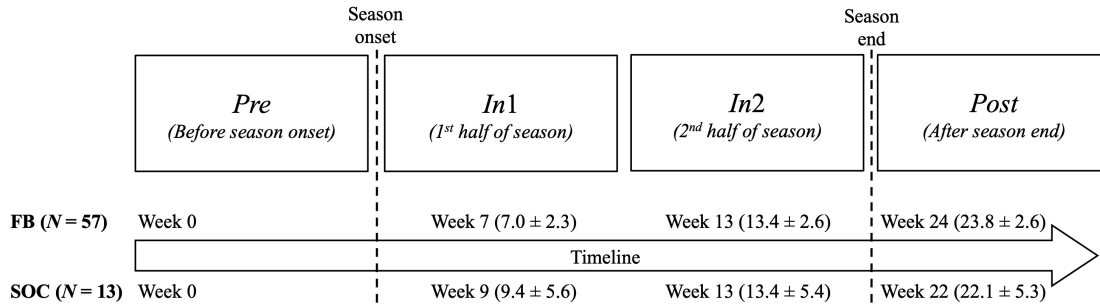
Fig. 3.1. Imaging schedule for high school football (FB) and soccer (SOC) athletes. The average intervals (± standard deviation, in weeks) between the preseason scanning session (*Pre*) and the follow-up sessions (*In*1, *In*2, *Post*) are reported.

Table 3.1.

Demographics of early-to-middle adolescent football (FB) and soccer (SOC) players with complete set of imaging data.

Group	American Football (FB) [$N = 57$]	Soccer (SOC) [$N = 13$]
Competition season	2016-2017	2015-2016
Gender	Male	Female
Age (range)	16.1 ± 1.0 (14, 18)	16.2 ± 1.0 (14, 18)
Years of high-school experience (YoE)		
0 year	6	2
1 year	11	1
2 years	22	5
3 years	18	5
Concussion history		
No	40	9
Yes	17	4
ADHD*		
No	49	13
Yes	8	0
Racial and ethnic categories		
White	33	12
Black or African American	6	0
Hispanic or Latino	5	1
Native American	3	0
More than one	6	0
Unspecified	4	0

* ADHD: Attention deficit hyperactivity disorder.

3.4.2 Magnetic Resonance Imaging

A 3T General Electric Signa HDx was used for data acquisition, using a 16-channel brain array (Nova Medical, Wilmington, MA). Diffusion weighted image data were acquired for DTI analysis using a spin-echo echo-planar imaging sequence (TE = 100 ms, TR = 12,500 ms, 40 slices with 2.5 mm thickness), with 30 diffusion-encoding directions at $b = 1000$ s/mm^2 and one acquisition at $b = 0$ s/mm^2, an acquisition matrix of 96 $\times$ 96, with a FOV of 24 $\times$ 24 cm^2.

Raw DWI images were upsampled to a 256 $\times$ 256 matrix by the MRI system. The DWI data were preprocessed using FSL (FMRIB 5.0; Oxford, U.K.), including correction for eddy currents (*eddy_correct*), followed by the extraction of aliasing-corrected brains (*BET*). The DTI metrics (FA, MD, AD, RD) were estimated for each individual (*DTIFit*), and the quality of each DTI map was visually inspected to confirm no motion artifact or geometrical distortion was present.

Tract-based spatial statistics (TBSS) [100] were performed to process all DTI maps for voxel-wise group-level analysis. First, a study-specific DTI template was constructed using all the individual FA images, based on a population-specific T1 template for early-to-middle adolescent collision-sport athletes [168] and using a high-throughput high-performance computing framework [248]. Then, individual FA images were aligned through a nonlinear transformation algorithm to the study-specific DTI template (*tbss_2_reg -t*). All aligned FA images were then normalized to the Montreal Neurological Institute standard space (MNI152 T1, 1 mm spatial resolution) (*tbss_3_postreg*). A mean FA skeleton was created from thinning the mean FA image that was averaged from all FA images of the dataset, thus representing the common WM tracts across all the subjects (*tbss_4_prestats*). The skeleton was thresholded at FA > 0.2 to reduce partial volume effects between borders of different tissues; this yielded a skeleton of approx. 80,000 upsampled (1 mm isotropic) voxels. To further reduce partial volume effects, regional maximal FA values were projected onto the skeleton according to a distance map [100]. Based on the mean FA skeleton, skeletons of the other DTI metrics were obtained by projecting local DTI values onto the FA skeleton (*tbss_non_FA*).

3.4.3 Head Acceleration Events (HAE) Measurements

Forty-five of the FB participants, and all the SOC participants had HAEs recorded during all practices and games for the observed season. HAEs were recorded using xPatch sensors (X2 Biosystems; Seattle, WA). The xPatch was placed behind a players right ear via adhesive patch after the area was cleaned with rubbing alcohol [84, 208]. Sensors were used if a football session required full pads and in all sessions for soccer. The raw HAE measures include PTA and total number of hits.

A detailed protocol of processing the HAE data is documented in Bari et al [63]. To process the raw HAE measures, recorded data were downloaded after sessions. Only the recorded data that fell within the valid time window of a practice or game were considered for analysis; these data were then thresholded to only include those with a PTA greater than or equal to 20 g [84, 208].

Outliers were removed per xPatch session per player, according to the following criteria: if ≥ 5 HAEs occurred within a 10-second time window during a session, all the readings

in the time window were flagged. If the number of flagged HAEs in a session accounted for more than 50% of the impacts for that session, all the HAEs from that session were removed, because this was indicative of a faulty sensor. Sessions with ≥ 100 recorded HAEs were considered because all sessions were observed and athletes never approached this many HAEs in a single session. If a session with ≥ 100 HAEs had an impact rate of 1 impact per minute, the session was removed. If the session had more than double the number of HAEs than the session with the greatest number of hits less than 100, the session was removed. The sensors were power cycled before being deployed for the next session.

In some xPatch sessions, a player participated without an active sensor. To correct for this and account for the times that a player was active but not wearing a sensor, repair data was generated. For each PTA threshold, an impact rate was calculated for each player per session type by dividing a players HAEs for a session type by the total active participation time for that session type in a season. The impact rate was multiplied by the time in a session a player was playing without a sensor to determine the number of repair HAEs needed for that session. Outlier days were also replaced using the same method with the missed time equal to the total time for the session. The repair HAEs were then used to estimate the repair PTA per session. For example, the repair PTA for the ith player in the kth session of the jth session type can be estimated using the Equation:

$$Repair\ PTA_{jk}^i = Repair\ Data_{jk}^i \times aPTA_{j,i}$$

The cumulative PTA were calculated by summing up a player's recorded and repair PTA to the players specific scan date. The average PTA were calculated by dividing the cumulative PTA by the total number of HAEs up to the player specific scan date. The total number of HAEs prior to each of the sessions ($In1$, $In2$, $Post$) was calculated by adding a player's recorded number of HAEs and repair data that were occurred on the same or prior date to the scheduled scan.

3.4.4   Cognitive Measurements

Participants were assessed for neurocognitive function prior to each MRI session. FB participants completed tests of: 1) Running memory span task, which assessed working memory [92, 249]; 2) Anti-saccade task, which assessed attention control [93, 250–252], 3) Go/no-go task, which assessed inhibitory control with go response time individual standard deviations (RTISD) and no-go accuracy [94, 253]. The SOC participants completed a computer-based Immediate Post-concussion Assessment and Cognitive Test (ImPACT^{TM}; ImPACT Applications Inc.; Pittsburgh, PA), a widely-implemented test in the athletic training community to assist return-to-play decision after clinically-diagnosed concussion [87, 88]. Four components were evaluated with computed scores, including verbal recognition memory (verbal memory composite), spatial recognition memory (visual memory composite), processing speed (visual motor speed composite), and reaction time (reaction time composite).

3.4.5 Statistical Analyses

Voxel-wise, nonparametric statistical testing was conducted to compare DTI metrics (FA, MD, AD, RD) and test microstructural abnormalities among the MRI sessions (*Pre*, *In*1, *In*2, *Post*) in a whole-brain manner. The resulting skeletons for each subject were taken as inputs of the FSL Randomise program (Randomise v2.9) [181]. The testing was conducted with 5,000 permutations, using a repeated measures ANOVA design, on contrasts among pairs of the MRI sessions (*Pre*, *In*1, *In*2, and *Post*). Type I errors were controlled by threshold-free cluster enhancement [182] and family-wise error (FWE) corrections across space for the size of the skeleton.

To investigate relations of DTI metrics with years of experience (YoE), HAE exposure, and cognitive performance, we focused on the contrasts comparing *Pre* and *In*2 for downstream ROI-based analyses, given that significant voxels ($p < 0.05$, FWE corrected) were observed for all the DTI metrics (Fig. 3.2 and 3.3). Significant voxels in the contrasts of FA and AD showing $Pre > In2$ and in the contrasts of MD and RD showing $Pre < In2$ were extracted via the FSL cluster program, with the corresponding WM tracts identified by the 48 ROIs on the Johns Hopkins WM label atlas (JHU-ICBM-DTI-81) [183]. Ten of the 48 ROIs did not contain voxels from the skeleton, due to the DWI acquisition and the FA > 0.2 thresholding procedure, and therefore they were excluded from statistical analysis, resulting in a total of 38 ROIs (see Table 3.2).

A 3-way ANCOVA of sports (FB, SOC) $\times$ time (*Pre*, *In*1, *In*2, *Post*) $\times$ YoE was performed to investigate the interaction and the main effects of YoE for the FB and SOC participants across a single season, using age, concussion history, and status of attention deficit hyperactivity disorder (ADHD) as covariates. Models were excluded when the residuals failed Shapiro-Wilks normality tests. The corresponding p-values were corrected with false discovery rate (FDR) (adjusted $p = 0.025$).

For each FB participant, the change of DTI values from *Pre* to *In*2 ($\Delta\text{DTI} = \text{DTI}_{In2}$ DTI_{Pre}) was computed within each ROI. To assess whether the distribution of ΔDTI was dependent on HAE exposure, each participant was categorized as 1) exhibiting positive or negative ΔDTI, and 2) being above or below an imposed threshold for HAE metrics (the total number of HAEs, cumulative PTA, and the number of HAEs exceeding certain PTA values) in the preceding 1-to-6 weeks prior to *In*2 and from the time when the participants had the 1st HAE (approx. ten weeks prior to *In*2). For each metric, a series of thresholds were imposed, and Pearsons Chi-squared tests were performed for each set of categories, corrected with FDR for multiple comparisons (adjusted $p = 0.025$). Two scenarios were recorded: the threshold with maximum counts of significant findings (*most-cases* scenario), and the lowest threshold at which the 1st significant finding was observed (1st-*case* scenario). To be considered as either scenario, the findings must survived the FDR correction for multiple comparisons, and when equal counts of the findings occurred, the one with *lower* HAE threshold was chosen. For each scenario, linear regression was used to model the relation after logarithmic conversions, and visualized using log-log plots (Fig. 3.5). No ROI-based Chi-square test was performed for SOC, due to the relatively small sample size ($N = 13$). An interactive application was developed using the Shiny package [254], to display the large number of statistical tests and the log-log plots. The application is hosted at: `https://boilerkai.shinyapps.io/PNG_dMRI_xPatch/`.

For each session (*Pre*, *In*1, *In*2, *Post*), associations between the ROI-based DTI metrics and cognitive measures (FB: running-span, anti-saccade, no-go accuracy, and go RTISD; SOC: verbal memory, visual memory, reaction time, and visual motor speed composites) were investigated using Pearsons partial correlations with age as covariate. Observations of cognitive measures exceeding two standard deviations from the mean of the corresponding session were excluded from the analyses. All the findings were corrected for multiple comparisons using FWE (adjusted $p = 0.05 \div 38$ ROIs $= 0.0013$). R version 3.6.1 [184] was used to perform all statistical analyses.

3.5   Results

3.5.1   Whole-brain Voxel-wise TBSS

From *Pre* to *In*2, FA (Fig. 3.2A) and AD (Fig. 3.2B) were significantly decreased, whereas MD (Fig. 3.3A) and RD (FIG. 3B) were significantly increased. The voxels exhibiting altered FA, MD, and RD were found within widespread WM tracts (Table 3.2). Those with altered AD were primarily within the left cerebral peduncle, left internal capsule (anterior, posterior, and retrolenticular), and the left sagittal stratum (Table 3.2).

At *Post*, FA was still significantly lower than *Pre* (Fig. 3.2A) and statistically equivalent to *In*2; however, we observed significant increase of AD since *In*2 (Fig. 3.2B). For MD (Fig. 3.3A) and RD (Fig. 3.3B), both were significantly decreased since *In*2, with more voxels exhibiting lower RD (MD: 3,241; RD: 46,689); however, both metrics were still higher compared to *Pre*.

3.5.2   ROI-based ANCOVA

Fractional Anisotropy (Table 3.3)

The 3-way interaction among sports, time, and YoE was not significant for any of the ROIs. Age was a significant covariate within the genu of the corpus callosum ($\beta = 0.006$, $p = 0.026$), left cerebral peduncle ($\beta = 0.009$, $p < 0.001$), right anterior limb of internal capsule ($\beta = 0.010$, $p < 0.001$), right anterior corona radiata ($\beta = 0.008$, $p = 0.004$), right cingulum (cingulate gyrus; $\beta = 0.019$, $p = 0.024$), and left cingulum (hippocampus; $\beta = 0.019$, $p = 0.001$), where higher FA was observed for older participants. Significant interactions between sports and YoE were observed within the left retrolenticular part of internal capsule ($\beta = -0.018$, $p = 0.034$) and the left cingulum (hippocampus; $\beta = -0.039$, $p = 0.041$), where the SOC participants with more YoE exhibited lower FA (Fig. 3.4A and 3.4B). There were main effects of YoE within the genu of the corpus callosum ($\beta = -0.012$, $p = 0.009$) and right anterior corona radiata ($\beta = -0.014$, $p = 0.001$), where participants with more YoE exhibited lower FA (see Fig. 3.4C and 3.4D for SOC participants). Participants with concussion history exhibited lower FA within the right cingulum (cingulate gyrus) than those no previous concussion ($\beta = -0.021$, $p = 0.013$). Participants with ADHD exhibited lower FA within the right anterior corona radiata, compared to those without ADHD ($\beta = -0.014$, $p = 0.010$).

Mean Diffusivity (Table 3.3)

Similar to FA, the 3-way interaction was not significant for any of the ROIs. Age was a significant covariate within the right cingulum (cingulate gyrus; $\beta = -1.05 \times 10^{-6}$, $p = 0.002$), where lower MD was observed in participants at older age. There was no significant interaction between sports and YoE within any of the ROIs. The main effects of YoE were observed within the right cingulum (cingulate gyrus; $\beta = 1.20 \times 10^{-5}$, $p = 0.028$) and right anterior corona radiata ($\beta = 1.41 \times 10^{-5}$, $p = 0.002$), where the participants with more YoE exhibited higher MD (see Fig. 3.4E and 3.4F for SOC participants). Neither concussion history nor ADHD was a significant covariate.

Axial Diffusivity

There was only one significant 3-way ANCOVA model for the left posterior corona radiata [F(16,263) = 1.978, $p = 0.015$], however, it was likely a false-positive finding given the small volume (2 mm^3).

Radial Diffusivity

There was no significant 3-way ANCOVA model for any of the ROIs.
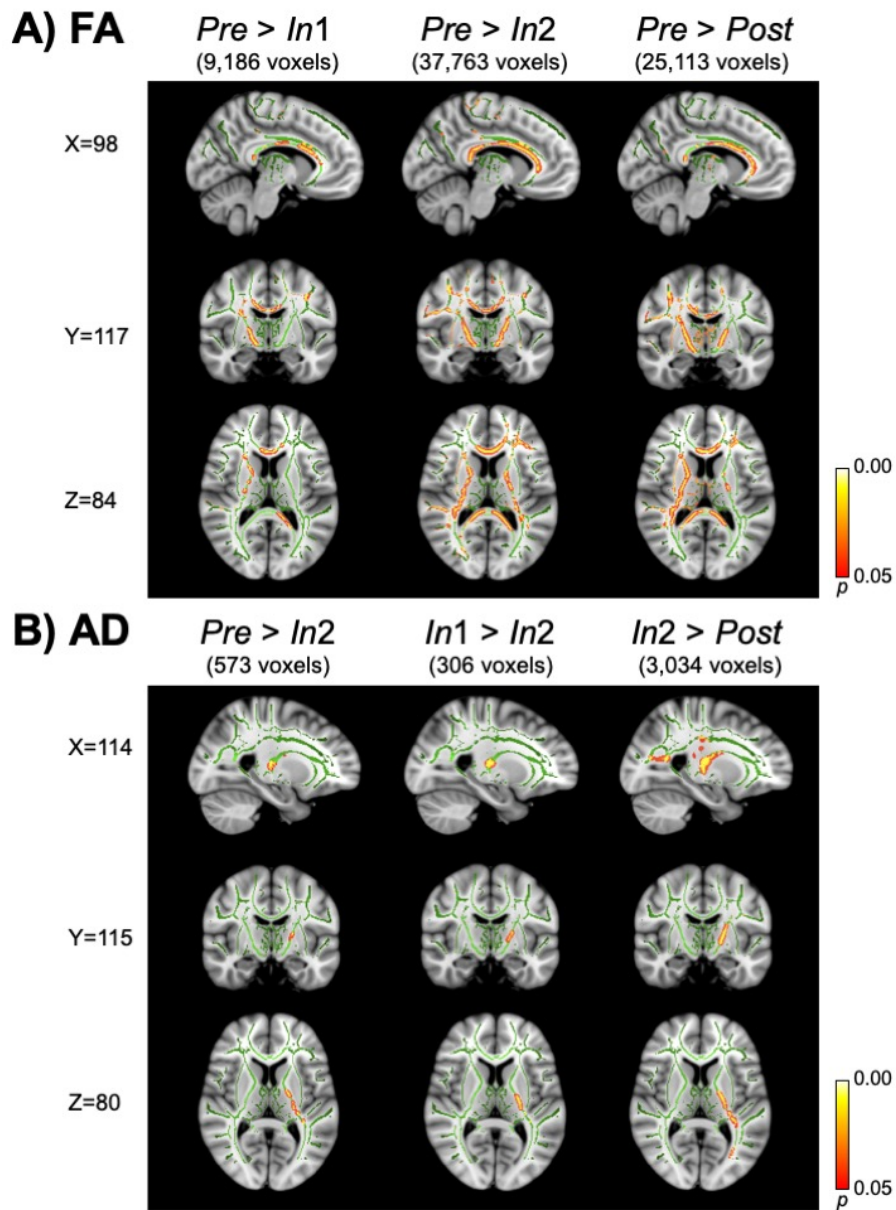
Fig. 3.2. Contrasts of whole-brain voxel-wise TBSS showing WM tracts with significant *Pre* to Post alterations of (**A**) fractional anisotropy (FA) and (**B**) axial diffusivity (AD) for the high school football and soccer athletes. From *Pre* to *Post*, there was a decrease of FA, whereas AD exhibited an in-season decrease followed by an increase at *Post*. All voxels were FWE corrected *t*-statistical maps ($p < 0.05$, red-yellow). The TBSS skeleton (green) is overlaid on the MNI template ($1.0 \times 1.0 \times 1.0$ mm^3) for visualization, displaying in sagittal, coronal, and axial views.
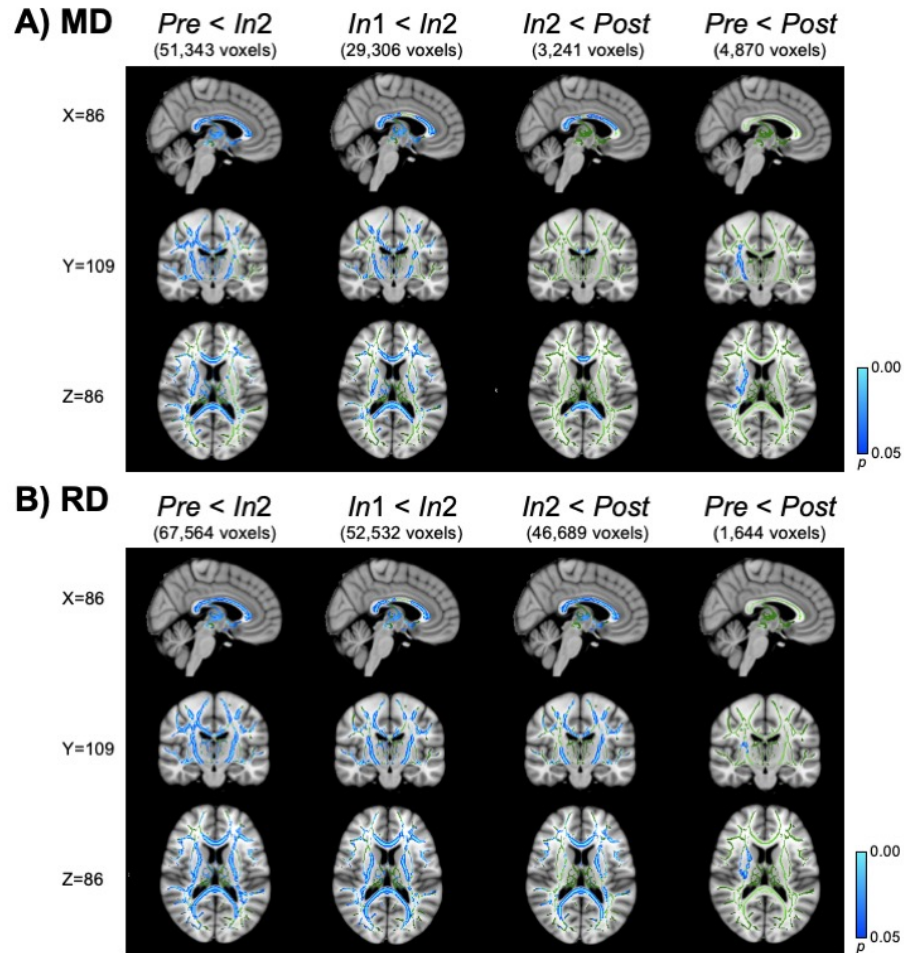
Fig. 3.3. Contrasts of whole-brain voxel-wise TBSS showing WM tracts with significant increase of (**A**) mean diffusivity (MD) and (**B**) radial diffusivity (RD) from *Pre* to *Post*, for the high school football and soccer athletes. All voxels were FWE corrected t-statistical maps ($p < 0.05$, blue-lightblue). The TBSS skeleton (green) is overlaid on the MNI template ($1.0 \times 1.0 \times 1.0$ mm^3) for visualization, displaying in sagittal, coronal, and axial views.

Table 3.2.

Number of statistically significant voxels with significant DTI changes from *Pre* to *In*2, within different WM tracts. All statistical significance was determined at FWE corrected $p < 0.05$. L/R: left/right hemisphere.

WM Tracts	# Voxels with significant *Pre* to *In*2 DTI changes			
	FA↓	MD↑	AD↓	RD↑
Genu of corpus callosum (gcc)	1212	1212	0	1606
Body of corpus callosum (bcc)	2057	2463	0	2986
Splenium of corpus callosum (scc)	1352	2195	0	2239
Fornix (fx)	0	71	0	86
Cerebral peduncle R (cpR)	192	273	0	272
Cerebral peduncle L (cpL)	159	183	61	244
Anterior limb of internal capsule R (alicR)	408	505	0	660
Anterior limb of internal capsule L (alicL)	411	174	84	558
Posterior limb of internal capsule R (plicR)	655	793	0	849
Posterior limb of internal capsule L (plicL)	577	552	149	833
Retrolenticular part of internal capsule R (rlicR)	620	575	0	742
Retrolenticular part of internal capsule L (rlicL)	426	129	181	586
Anterior corona radiata R (acrR)	439	784	0	1093
Anterior corona radiata L (acrL)	867	797	0	1274
Superior corona radiata R (scrR)	1003	1218	0	1307
Superior corona radiata L (scrL)	823	410	3	1063
Posterior corona radiata R (pcrR)	259	381	0	442
Posterior corona radiata L (pcrL)	289	207	2	282
Posterior thalamic radiation R (ptrR)	356	349	0	700
Posterior thalamic radiation L (ptrL)	184	113	2	361
Inferior longitudinal/fronto-occipital fasciculus R	191	240	0	278
Inferior longitudinal/fronto-occipital fasciculus L	119	59	36	128
External capsule R (ecR)	667	852	0	961
External capsule L (ecL)	137	369	0	751
Cingulum (cingulate gyrus) R (cgR)	30	182	0	154
Cingulum (cingulate gyrus) L (cgL)	81	234	0	272
Cingulum (hippocampus) R [cg(h)R]	83	55	0	82
Cingulum (hippocampus) L [cg(h)L]	24	17	0	36
Fornix (cres)/stria terminalis R (fx/stR)	236	181	0	230
Fornix (cres)/stria terminalis L (fx/stL)	186	134	0	211
Superior longitudinal fasciculus R (slfR)	1122	1371	0	1584
Superior longitudinal fasciculus L (slfL)	722	784	0	1216
Superior fronto-occipital fasciculus R (sfofR)	57	100	0	109
Superior fronto-occipital fasciculus L (sfofL)	38	3	3	79
Uncinate fasciculus R (ufR)	20	20	0	20
Uncinate fasciculus L (ufL)	0	0	0	13
Tapetum R (ttR)	37	62	0	67
Tapetum L (ttL)	23	38	0	40

Table 3.3.

ROI-based ANCOVA for regional FA and MD of adolescent collision-sport (FB and SOC) athletes with different years of high-school experience (YoE). All the reported models are significant after FDR correction (adjusted $p < 0.025$). Statistically significant β coefficients of the models are marked in bold ($p < 0.05$). L/R: left/right hemisphere.

Tract Name	Overall F	p	Age β	p	SOC×YoE β	p	YoE β	p
FA								
Genu of corpus callosum	F(16,263)=2.959	<0.001	**0.006**	**0.026**	-0.002	0.829	**-0.012**	**0.009**
Cerebral peduncle L	F(16,263)=2.337	0.003	**0.009**	**<0.001**	-0.006	0.418	-0.003	0.361
Anterior limb of internal capsule R	F(16,263)=2.395	0.002	**0.010**	**<0.001**	0.004	0.650	-0.004	0.338
Retrolenticular part of internal capsule L	F(16,263)=1.994	0.014	-0.002	0.525	**-0.018**	**0.034**	0.006	0.193
Anterior corona radiata R*	F(17,262)=3.013	<0.001	**0.008**	**0.004**	0.010	0.252	**-0.014**	**0.001**
Cingulum (cingulate gyrus) R#	F(17,262)=2.309	0.003	**0.019**	**0.024**	-0.019	0.319	0.003	0.770
Cingulum (hippocampus) L	F(16,263)=2.064	0.010	**0.019**	**0.001**	**-0.039**	**0.041**	-0.005	0.581
MD								
Anterior limb of internal capsule R	F(16,263)=2.190	0.006	-3.18×10^{-6}	0.237	-1.35×10^{-5}	0.106	5.39×10^{-6}	0.211
Anterior corona radiata R	F(16,263)=3.048	<0.001	-5.54×10^{-6}	0.054	-1.21×10^{-5}	0.176	$\mathbf{1.41 \times 10^{-5}}$	**0.002**
External capsule R	F(16,263)=2.374	0.003	-2.28×10^{-6}	0.439	-9.01×10^{-6}	0.324	4.31×10^{-6}	0.362
Cingulum (cingulate gyrus) R	F(16,263)=3.275	<0.001	$\mathbf{-1.05 \times 10^{-6}}$	**0.002**	1.95×10^{-6}	0.853	$\mathbf{1.20 \times 10^{-5}}$	**0.028**

* ADHD status was a significant covariate ($\beta = -0.014, p = 0.010$).

Concussion history was a significant covariate ($\beta = -0.021, p = 0.013$).
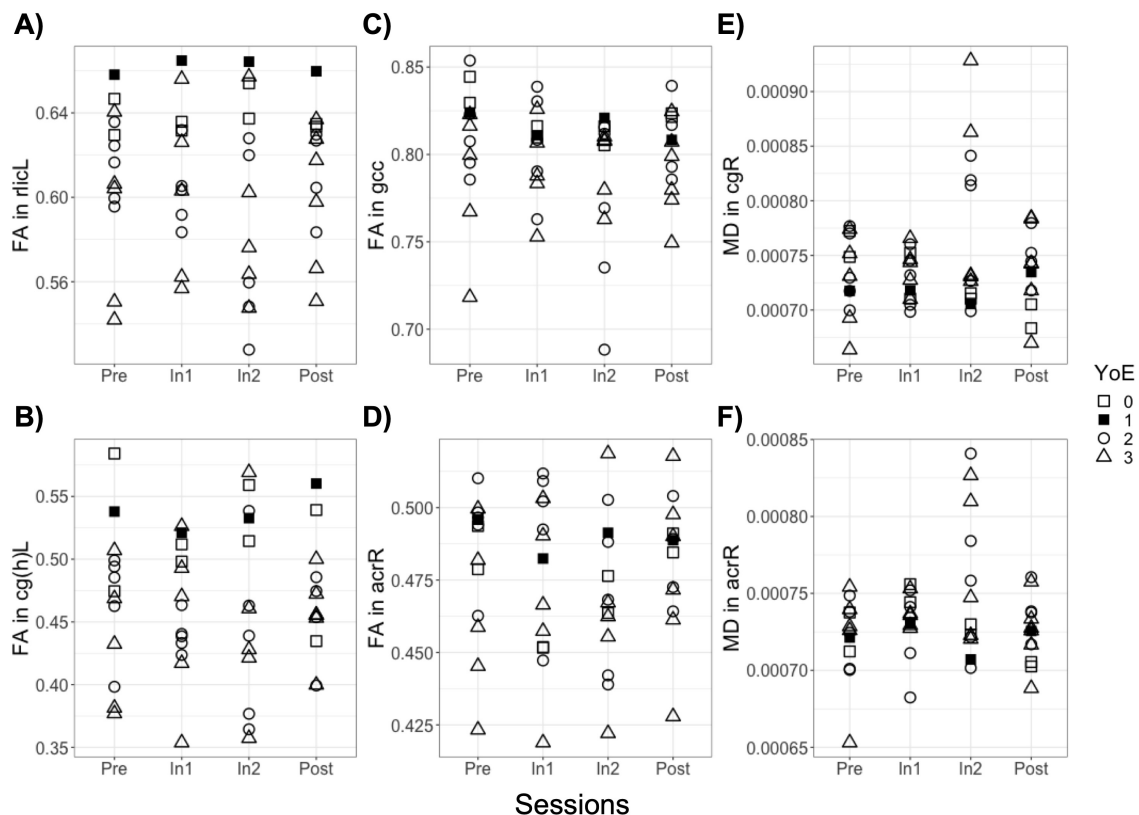
Fig. 3.4. Scatter plots of ROI-based ANCOVA (see Table 3.3) for the soccer athletes. There was typical segregation of FA/MD values by the years of high-school experience (YoE), with lower FA and higher MD observed for players with 3 YoE (△) than those participating for the first time (□). FA in the (**A**) left retrolenticular part of internal capsule (rlicL), (**B**) left cingulum (hippocampus) [cg(h)L], (**C**) genu of the corpus callosum (gcc) and (**D**) right anterior corona radiata (acrR), and MD in the (**E**) right cingulum (cingulate gyrus) (cgR) and (**F**) right anterior corona radiata (acrR), are shown at different sessions.

3.5.3 Dependence of regional DTI changes with HAE exposure

For the 45 FB participants with recorded HAE exposure, the 1st significant finding of altered distribution of ΔDTI (i.e. 1st-*case* scenario) was observed when the participants experienced 33 HAEs/week for the preceding week to $In2$, 18.5 HAEs/week for two weeks, 17.0 HAEs/week for three weeks, 14.0 HAEs/week for four weeks, 14.6 HAEs/week for five weeks, 15.0 HAEs/week for six weeks, and 19.4 HAEs/week since the 1st HAE (approx. ten weeks). Most of the significantly altered distributions of ΔDTI (i.e., *most-cases* scenario) were observed at 85.0 HAEs/week for the preceding week to $In2$, 45.5 HAEs/week for two weeks, 31.7 HAEs/week for three weeks, 35.0 HAEs/week for four weeks, 33.4 HAEs/week for five weeks, 29.2 HAEs/week for six weeks, and 28.8 HAEs/week since the 1st HAE (approx. ten weeks). For the *most-cases* scenario, the linear regression model after the logarithmic conversions was significant with negative slope (Fig. 3.5A).

For cumulative PTA, similar to the weekly HAE exposure, the 1st-*case* scenario was observed when the participants experienced 2468.0 g/week for the preceding week to $In2$, 775.5 g/week for two weeks, 599.3 g/week for three weeks, 557.0 g/week for four weeks, 574.4 g/week for five weeks, 554.7 g/week for six weeks, and 641.5 g/week since the 1st HAE. The *most-cases* scenario were observed when the participants experienced 2895.0 g/week for the preceding week to $In2$, 1388.5 g/week for two weeks, 1239.3 g/week for three weeks, 1224.2 g/week for four weeks, 1261.2 g/week for five weeks, 1095.2 g/week for six weeks, and 1237.6 g/week since the 1st HAE. For the *most-cases* scenario, the linear regression models after logarithmic conversions were significant with negative slope (Fig. 3.5B). The linear model for the 1st-*case* scenario was also significant (not shown in Fig. 3.5B).

Dividing the cumulative PTA by the total number of HAEs, the most-cases scenario were observed when PTA per hits exceeded 34.1 g/HAE for the preceding week to $In2$, 30.5 g/HAE for two weeks, 39.1 g/HAE for three weeks, 35.0 g/HAE for four weeks, 37.8 g/HAE for five weeks, 37.5 g/HAE for six weeks, and 43.0 g/HAE since the 1st HAE (approx. ten weeks). The linear regression after logarithmic conversions was not significant (figure not shown), which was equivalent to a horizontal line with y intercept at the mean (1.56 in log scale, 36.7 g/HAE in original scale).

A)

B)
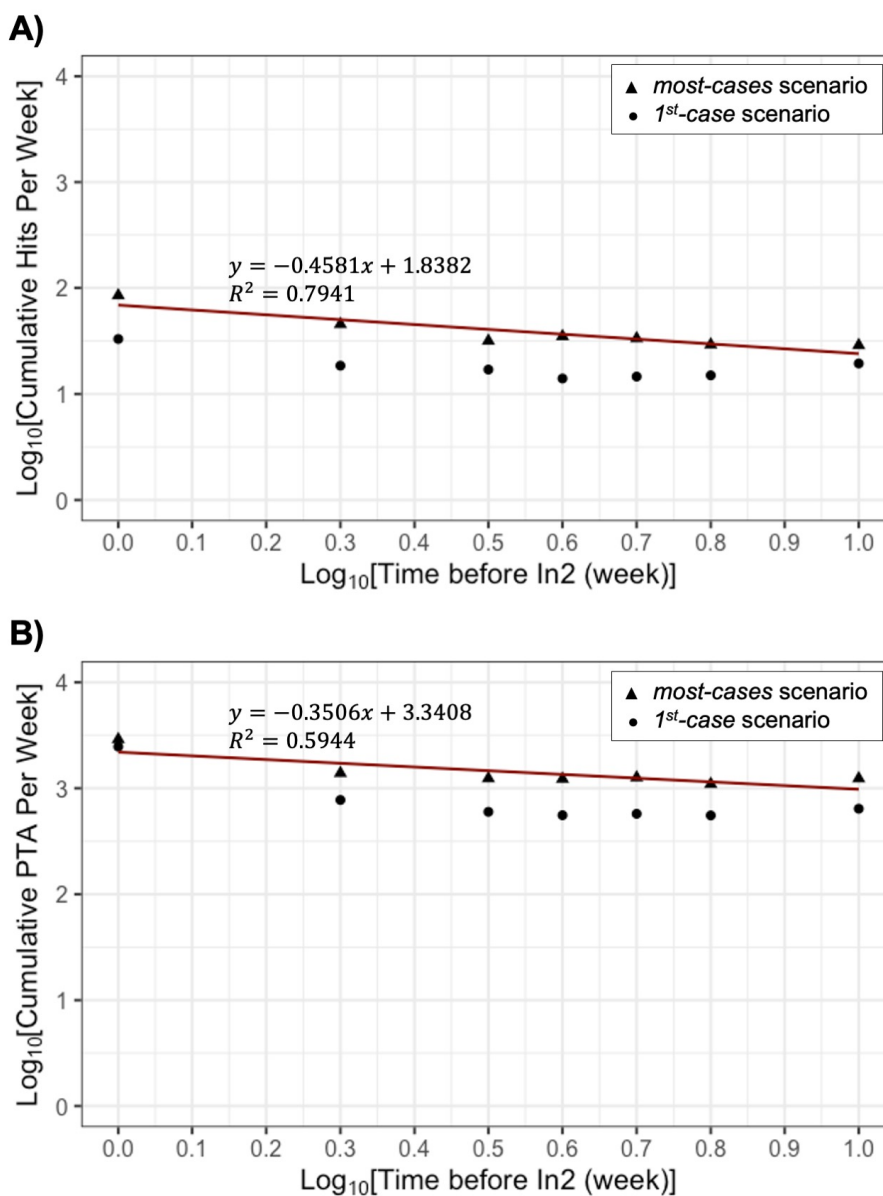
Fig. 3.5.   Log-log plots showing dependence of regional DTI changes with patterns of HAE exposure for the football athletes. Points indicate the observed thresholds of the maximum counts of significant findings (*most-cases* scenario, ▲), and the 1st count of significant finding (1*st-case* scenario, ●). Regression lines (dark red) indicate the predicted thresholds for the *most-cases* scenarios of (**A**) Cumulative hits/week and (**B**) cumulative PTA/week, with respect to the number of weeks prior to $In2$ scan. For detailed Chi-squared tests, visit the application at: `https://boilerkai.shinyapps.io/PNG_dMRI_xPatch/`.

3.5.4 Associations with Cognitive Measurements

For FB participants, lower Pc scores of anti-saccade task at Post correlated with higher MD and RD within the bilateral posterior corona radiata [right: MD (r = -0.510), RD (r = -0.531), both $p < 0.001$; left: MD (r = -0.440), RD (r = -0.447), both $p = 0.001$], and right posterior thalamic radiation [MD (r = -0.459), RD (r = -0.444), both $p = 0.001$]. Lower scores were also correlated with higher diffusivity metrics within the right cingulum (cingulate gyrus; MD: r = -0.450, $p = 0.001$) and right tapetum (RD: r = -0.435, $p = 0.001$) (Fig. 3.6). There was no significant association between other cognitive measures (running-span, no-go accuracy, go RTISD) and DTI metrics for any of the sessions.

For SOC participants, higher visual memory composites at Pre were correlated with higher AD within the left cerebral peduncle ($r = 0.908$, $p < 0.001$). There was no significant association between other cognitive measures (visual memory, reaction time, visual motor speed composites) and DTI metrics for any of the sessions.
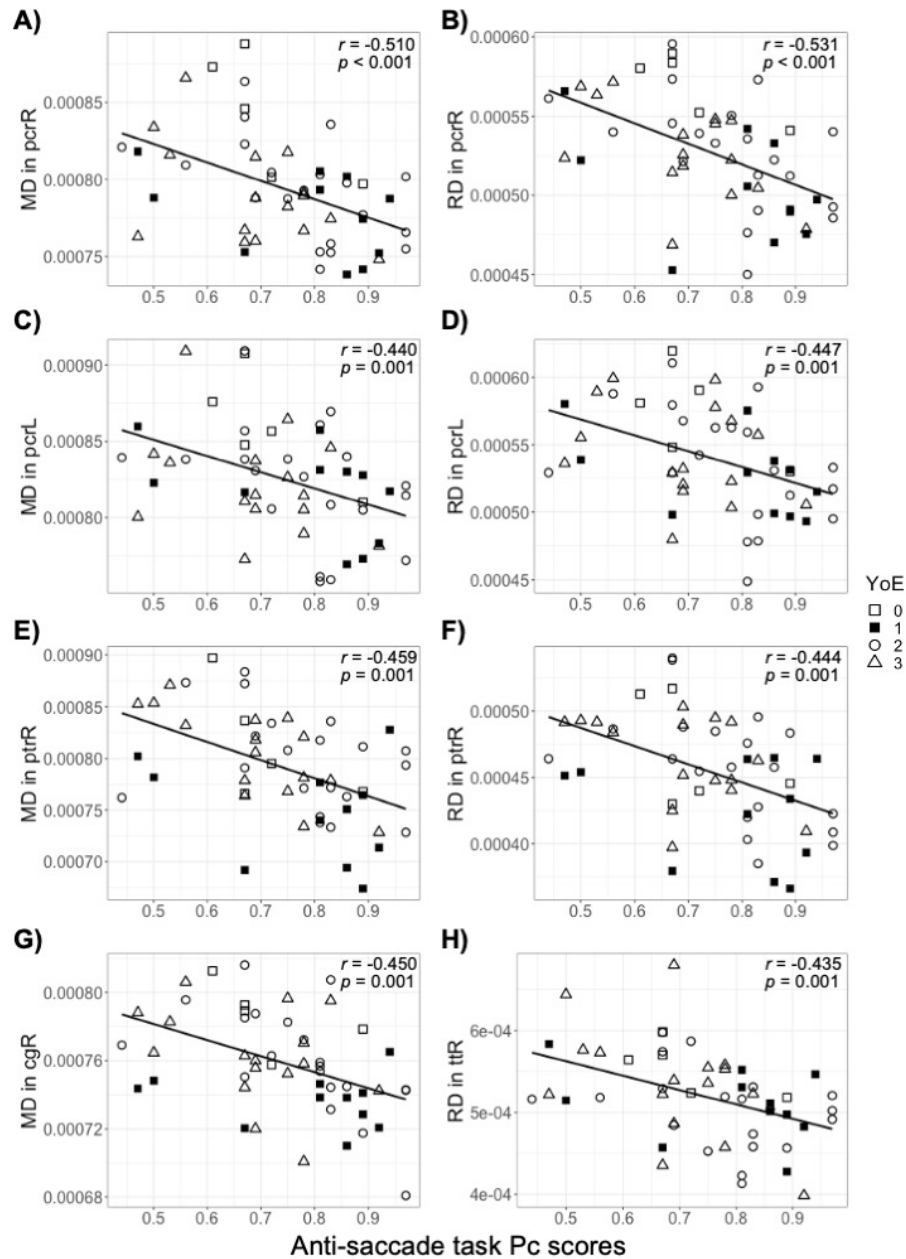
Fig. 3.6. Associations between proportion correct (Pc) scores of anti-saccade task and diffusivity metrics for the football athletes, within (**A** and **B**) the right posterior corona radiata (pcrR), (**C** and **D**) left posterior corona radiata (pcrL), (**E** and **F**) right posterior thalamic radiation (ptrR), (**G**) right cingulum (cingulate gyrus) (cgR), and (**H**) right tapetum (ttR) at *Post* (after season end).

3.6 Discussion

Using a Structural Health Monitoring protocol [32], we assessed WM microstructure, HAEs, and cognitive performance of early-to-middle adolescent collision-sport athletes across a single season. As the competition season progressed, FB and SOC participants typically exhibited WM abnormalities, which largely persisted to post-season (Fig. 3.2, 3.3, and Table 3.2). In the WM tracts with significant alterations, FA increased and MD decreased as a function of age, but such process was reversed for participants with more YoE (Fig. 3.4 and 3.3). For FB participants, exposure to HAEs exceeding 37 g was sufficient to alter the distributions of DTI changes from Pre to $In2$ (Fig, 3.5), and cognitive impairments were associated with higher MD and RD at post-season (Fig. 3.6).

The WM microstructural abnormalities developed after the start of the season and persisted into post-season Fig. 3.2 and 3.3). Whole-brain voxel-wise TBSS showed a significant decrease of FA and increase of MD from Pre to $In2$ (Table 3.2). Decreased FA typically reflects misalignment, disruption of axons, or demyelination [95, 225, 226, 255, 256], which is often associated with reduced axonal density, leading to increased MD [227–229]. Measures of FA and MD depend on the magnitudes of AD and RD; the decreased AD and increased RD from Pre to $In2$ (Table 3.2) may indicate a compromised integrity of axonal membrane and myelin [231], where the widespread increase of RD may be the primary factor driving the FA reduction and MD increase. The fewer voxels exhibiting abnormal DTI change at post-season ($Pre > Post$, Fig. 3.2A; $Post < In2$, Fig. 3.3A and 3.3B), together with the AD increase ($Post > In2$, Fig. 3.2B), supported the hypothesis of an active WM injury and repair process [78]. Here, the repair seemed to occur faster than damage due to injury, yet the WM has not been fully restored to a level comparable to the baseline (Fig. 3.2A, 3.3A and 3.3B). These observations were consistent with previous studies that detected WM abnormalities across a single season in youth [257] or high school football [158].

Years of high-school experience playing collision sports may serve as an indicator of high-risk individuals in early-to-middle adolescents for subconcussive trauma. ROI-based ANCOVA demonstrated an increase of FA and decrease of MD as a function of age (Table 3.3), which is consistent with the normal trajectory of brain development during adolescence [146, 217–220]. Participants with more YoE, however, exhibited lower FA or higher MD than those with fewer YoE (Table 3.3), suggesting that the WM maturation process can be perturbed by regular participation in collision sports over years. This is consistent with previous DTI studies that prolonged HAE exposure can accumulate abnormalities of WM microstructure and contribute to neural injury in collision-sport athletes [61, 75, 257]. These injuries can lead to dysfunction in controlling stress and emotional behaviour [258], which has long been believed to exacerbate the injury risk in adolescent athletes [259]. Therefore, adolescent collision-sport athletes with more YoE presents a priority in preventive strategies for controlling HAE exposure, which may effectively minimize risk of developing subconcussive trauma.

Interpreting the directionality of DTI changes need to be pertinent to the study design and cannot be made without paying attention to the heterogeneous analytical approaches and image processing [144, 242]. Although the whole-brain voxel-wise TBSS suggested the directionality of DTI changes predominant at group level, they do not necessarily represent the trajectory for each individual. Such profile was characterized in this study by the ROI-based analyses for significant contrasts between Pre and $In2$. Both increase and decrease of

FA were presented at the individual level, providing insights to the general trend (decreased FA) suggested by TBSS. Elevated FA was constantly observed in mTBI subjects with acute WM injury (within two weeks) [260], which may be a consequence of reduced inter-axonal space due to axonal swelling [242]. In addition, we also observed more participants exhibited decreased MD and/or RD when HAE exposure exceeded a particular dosage, which contradicted the general trend (increased MD and RD). Concurrent decrease of diffusivity metrics from pre-season to post-season has also been reported in the literature [157, 162], which may be attributed to axonal swelling or inflammation that lowers the water content in extracellular space [261]. Besides variability in analytical approaches, efforts to minimize bias and errors in every processing steps is another critical aspect in studies of mTBI and subconcussive trauma, because the magnitudes of changes are often subtle, especially for adolescent athlete cohorts who are undergoing rapid brain development [145–148]. In this study, a study-specific DTI template was constructed for spatial normalization, based on an unbiased population-specific brain atlas for early-to-middle adolescent collision-sport athletes [168, 248].

To the best of our knowledge, this is the first DTI study providing a temporal profile of HAE exposure (Fig. 3.5) that allows for examination of individual FB players during the season, which may help develop strategies to prevent the subconcussive sequelae from persisting into the post-season. Data of the 1st-case scenario represent the lowest amount of HAEs that led to a significant alteration to the distribution of DTI change, providing a subconcussive threshold at which a given FB participant may start to develop neural injury. Data of the *most-cases* scenario represent the subconcussive threshold at which most of such significant alterations were observed. Based on the profiles (Fig. 3.5), WM microstructural abnormalities were typically a consequence of accumulating either more frequent and stronger HAEs over a shorter time, or less frequent and milder HAEs over a longer time (Fig. 3.5). We previously showed that PTA was not a sufficient measure to predict cognitive deficits [64]. Here, we showed that the pattern of HAE exposure over the season, including both the frequency (number of HAE) and magnitude (cumulative PTA) in a given time, should be monitored for predicting WM microstructural deficits. A previous studies that utilized a 10 g threshold found an average of 50 HAEs/week would lead to physiological deficits in post-season measured by fMRI [30, 64]. Here, at a 20 g threshold, we demonstrated that HAEs exceeding 37 g were sufficient to alter the distributions of DTI changes, and the threshold did not significantly vary over time. Our finding augmented previous DTI work by Jang et al. that every HAE (> 20 g) seemed to accumulate WM microstructural abnormalities [74, 89], but HAEs exceeding 37 g can meaningfully accumulate neural injury that may persist to post-season. These findings extended our understanding of high-load HAE exposure, which was previously shown to meaningfully affect cerebrovascular reactivity [78] and lead to metabolic disturbances [76, 241].

We identified WM microstructural abnormalities correlated with poorer performance in cognitive assessments. In FB participants, lower scores of anti-saccade task at post-season correlated with higher MD and RD, primarily within the WM tracts of posterior brain regions and the right cingulum (cingulate gyrus; Fig. 3.6). Notably, posterior thalamic radiation fibers connect thalamus with the posterior parietal lobe, an area involved in performing anti-saccade task [262, 263]. Cingulum fibers connect to the posterior cingulate gyrus, which is prominent for cognitive functions such as working memory and attention [264]. Interestingly, participants with more YoE also demonstrated higher MD within the right cingulum

(cingulate gyrus; Fig. 3.6), suggesting these individuals may be at higher risks of cognitive impairments. We only observed one significant correlation between DTI and ImPACT scores for SOC participants, which may be a false-positive finding given the many correlation analyses performed. Overall, these findings identified neurological pathways that may explain the connection between subconcussive HAEs and cognitive impairments.

This study has several limitations. Because we did not evaluate male soccer athletes, population bias can exist, and it remains to be explored which of these changes may exist in athletes playing other sports. No temporal profile of DTI and HAE exposure was provided for SOC participants as we did for FB (Fig. 3.5), because the sample size was too small (N = 13) to allow ROI-based Chi-square tests being performed. ImPACT has been shown to bear relatively high false-positive rates [74, 89] and variable reliability [90, 91], warranting caution when interpreting the outcomes. FDR procedure was used in ROI-based ANCOVA and Chi-square tests to adjust multiple comparisons, which can lead to more false-positive findings. The associations with cognitive measures still bears replication in a subsequent sample, even though the FB dataset is larger than many studies of this type, and a stringent FWE procedure was carried out. The datasets of this work haven't utilized more advanced diffusion imaging techniques developed and applied in studying collision sports, including kurtosis imaging [265, 266], multi-shell imaging [239, 240] and neurite orientation dispersion and density imaging [239, 267, 268]. It is expected that the ongoing development of diffusion MRI will advance understanding of TBI and concussion in collision sports, therefore facilitating improved care of cognitive and brain health for these athletes.

3.7 Conclusion

Concerns in recent years regarding the brain and cognitive health of adolescent collision-sport athletes are supported by this work. The WM microstructural abnormalities developed during the competition season can persist after the season ended, and based on correlations with cognitive measures, the abnormal WM microstructure could affect these athletes performance and particularly with regard to attention control, making them more vulnerable to future sports-related injury. Such adverse effect may be prevented by controlling the extent of HAE exposure during the season, especially for those with more years of experience. Such actions may help resume the normal WM development pattern for adolescents and ensure their cognitive health.

3.8 Acknowledgments

4. FUTURE DIRECTIONS

4.1 Monitoring Volumetric Trajectory

The grey matter labels (Fig. 2.3) may be used to monitor the volumetric trajectory of the cohort of adolescent collision-sport athletes. One explanation of the results in Fig. 2.4B is that the adolescent collision-sport athletes had morphological characteristics that deviated from healthy adolescents of similar age bracket, represented by the $NIHPD_{13.0-18.5}$ template. In addition, adolescents (age 13–17) demonstrated non-linear decrease in certain subcortical volumes, as was shown in a lifespan study of healthy adolescents [116] It would then comprise a meaningful exploration to see whether the characteristics and trajectories of the subcortical volumes are different in adolescent collision-sport athletes, compared to those observed in the healthy subjects of Narvacan et al.'s study [116].

Before data analysis, it is critical to obtain accurate segmentation of subcortical volumes for each subject. Three grey matter labeling protocols were involved when running *recon-all* in Freesurfer [269] to segment the PNG T1 template, and each of the protocols resulted in different number of labels. Desikan-Killiany protocol [177] resulted in 35 ROIs per hemisphere (Fig. 2.3), and is commonly used in literature [270]. Desikan-Killiany-Tourville protocol [178] resulted in 31 ROIs per hemisphere, 4 fewer than the Desikan-Killiany protocol (banksSTS, corpus callosum, frontal pole, and temporal pole) (Fig. 4.1), and Destrieux protocol [179] resulted in 74 ROIs per hemisphere, the most among the three protocols (Fig. 4.2). Manual editing on the labels is needed, preferably by a certified neuroradiologist, to ensure each brain region was correctly segmented. Following the editing, accuracy of segmentation can be evaluated using Dice Similarity Coefficient [271]:

$$\frac{2 \times \text{True Positive}}{2 \times \text{True Positive} + \text{False Positive} + \text{False Negative}}$$

Besides accuracy, segmentation should have high precision and labeling efficiency [272]. Label fusion strategies, such as major vote [271], take multiple atlases into account, which effectively avoids bias from a single atlas and produces consistent segmentation. To implement these strategies, an integrated computational framework (e.g. Fig. 2.1) can allow labeling to be performed at large scale and at the fastest speed.
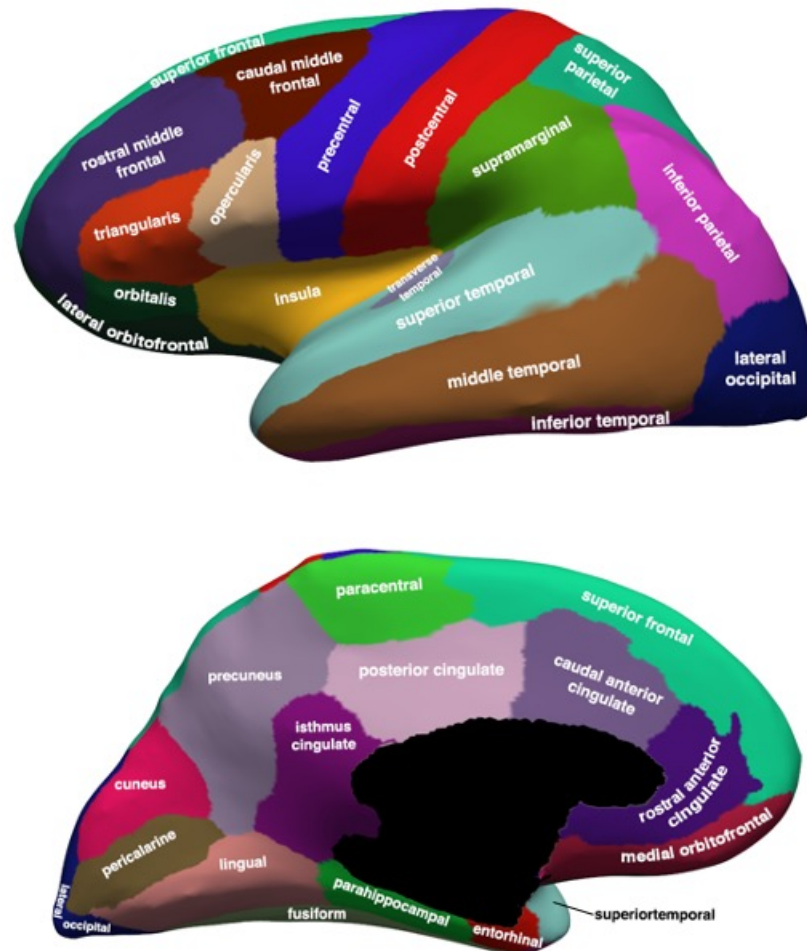
Fig. 4.1. Lateral (top) and medial (bottom) views of PNG Desikan-Killiany-Tourville Grey Matter Atlas.
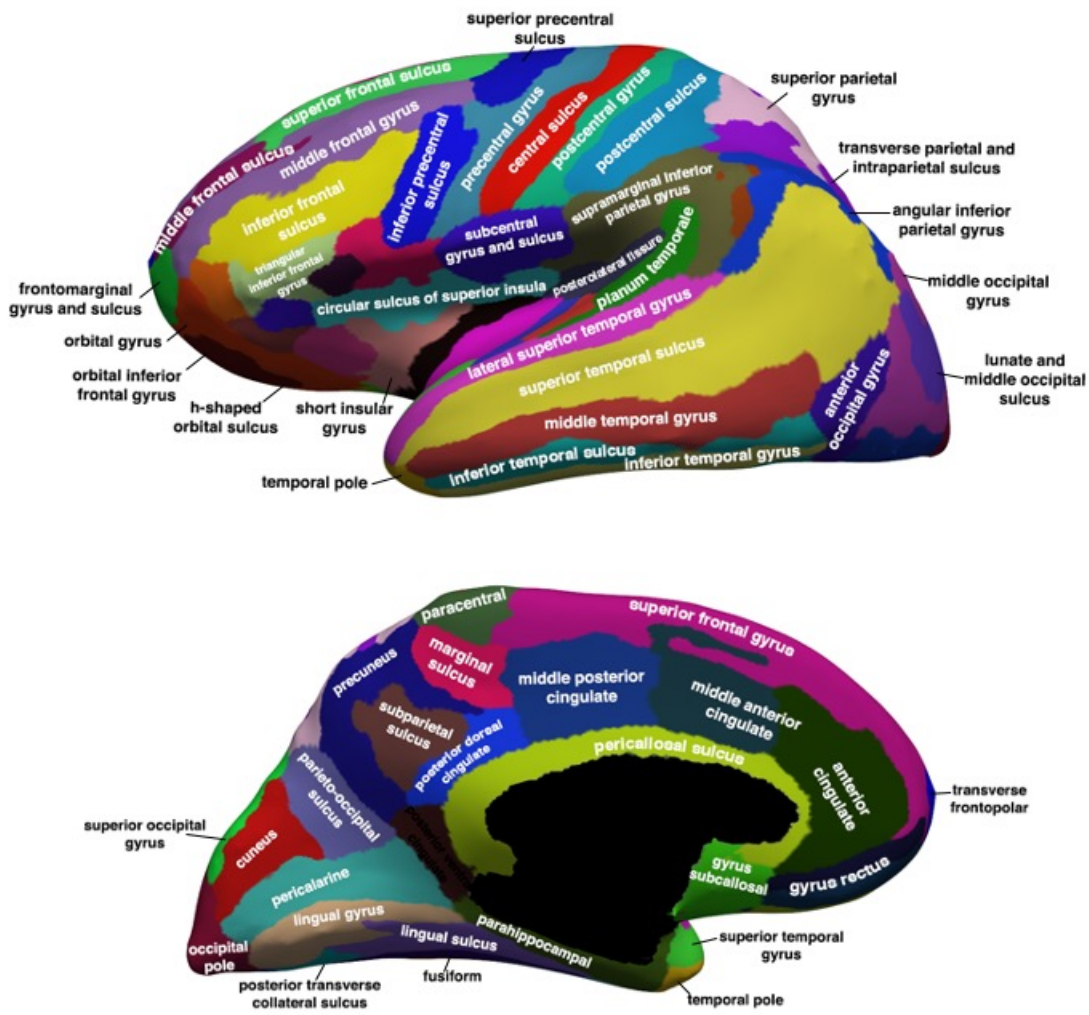
Fig. 4.2. Lateral (top) and medial (bottom) views of PNG Destrieux Grey Matter Atlas.

4.2   Diffusion Kurtosis Imaging

Diffusion Kurtosis Imaging (DKI) is an advanced diffusion MRI technique that probes the extent of water diffusion deviated from a normal Gaussian distribution. In reality, patterns of water diffusion in brain may be non-Gaussian, due to the complex cellular environment of white matter and different pathological conditions; therefore, DKI provides a more sensitive representation of potential underlying change due to mTBI than the traditional tensor model [273]. A few studies have employed DKI to investigate sport-related concussion in adolescent and/or collegiate football athletes [156, 239, 240], but so far, to the best of our knowledge, no study has investigated the effect of repetitive head impacts on adolescent brain using DKI.

To obtain estimates of diffusion kurtosis, the acquired DWI must have at least two nonzero b-values and 15 distinct gradient directions, see Appendix B for a derivation. In general, diffusion kurtosis tends to increase with increased diffusion heterogeneity, and can be altered by water exchange and diffusion barriers [274]. Voxels with high values of diffusion kurtosis indicates larger extent of deviation of water diffusion from Gaussian distribution [275], suggesting complexity of diffusion in the extracellular space. For example, increased axial kurtosis (K_{ax}) indicates "axonal beading" that occur after axonal injury, where accumulations of proteins occur along an axon after calcium influx [276].

A bespoke preprocessing pipeline for obtaining DKI metrics has been streamlined based on the PNG longitudinal database (Fig. 4.3). There are two sets of data, one set comprising four $b=0$ and thirty $b=1000$ 3D DWI volumes, and the other comprising four $b=0$ and thirty $b=2000$. After converting into NIfTI formats (*dcm2nii*), all the DWI data undergo corrections for motion and eddy current (*eddy*) [277], followed by brain extraction (*bet*). Of note, it is recommended to use FSL *eddy* [277], the latest tool in replacement of the previous *eddy_current*, for simultaneously correcting motion artifacts and geometric distortions induced by eddy current, which can also detect and replace outlier slices with signal dropout (*eddy -repol*) [278]. Next, rigid body registrations are performed to align the two DWI data sets for each individual (*flirt*). An average is computed from the eight $b=0$ volumes (*fslsplit*, *fslmaths*), and a new 4D DWI file is created (*fslmerge*), in which the volumes are merged in the order of $b=0$, $b=1000$, and $b=2000$. A text file containing diffusion direction vectors (in the same order as the new DWI file) are also created. Finally, the new 4D DWI volumes, together with the text files, are taken as inputs of fed into Diffusion Kurtosis Estimator (DKE, version 2.6) [279] to obtain DKI metrics, including K_{ax}, K_{mean}, and K_{rad} (see Appendix B).

In DKE processing, a $3 \times 3 \times 3$ outlier removal median filter is applied to voxels that violated the constraints [279], which may produce erroneous estimates in major fiber tracts. By default, a "strong filtering" is applied to remove voxels that violate any of the constraints; the alternative "weak filtering" only remove voxels that violate ≥ 15 constraints. An example of strong and weak filtering is illustrated in Fig. 4.4. For outputs of low quality from the default strong filtering pipeline, reprocessing using weak filtering can be considered, but for both cases, rigorous quality assessments are required to make sure the DKI data can proceed for analyses.
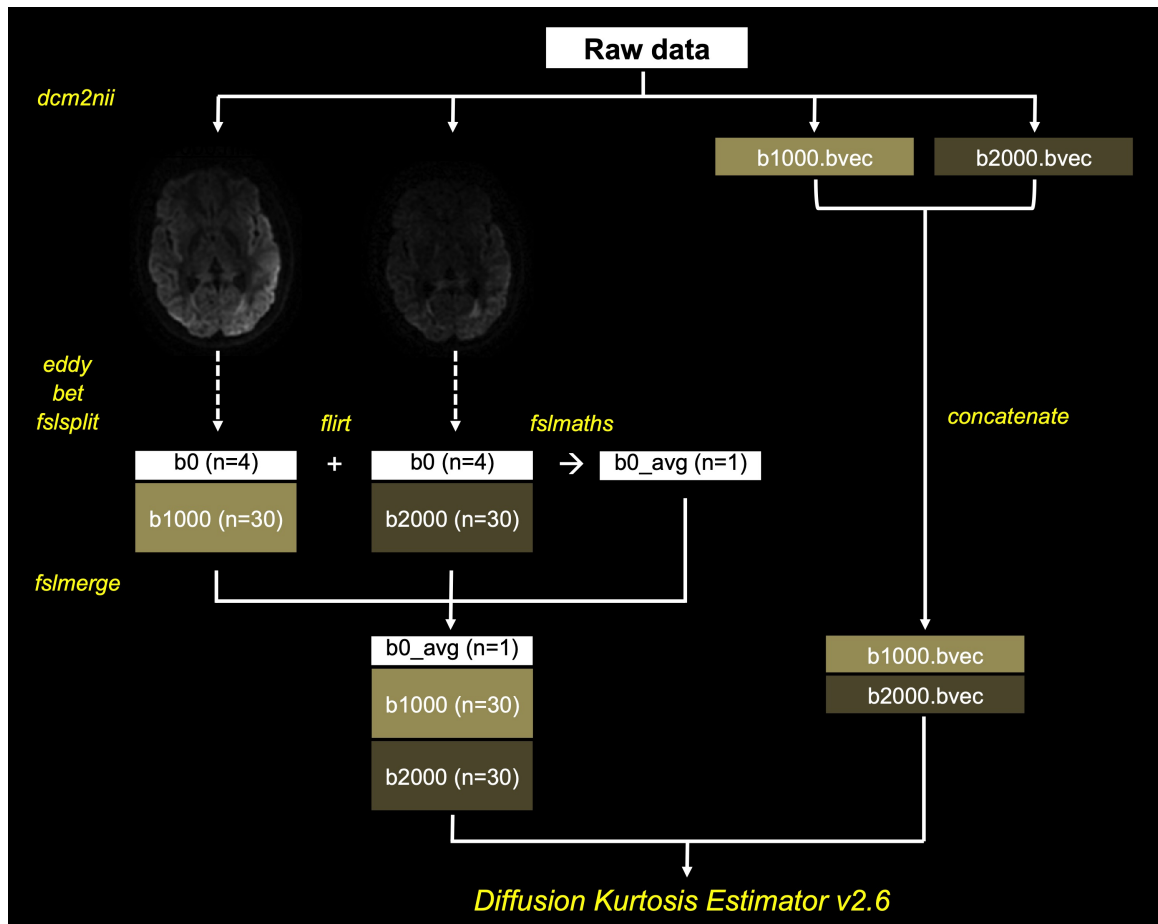
Fig. 4.3. Preprocessing pipeline for estimating DKI metrics using Diffusion Kurtosis Estimator [279].
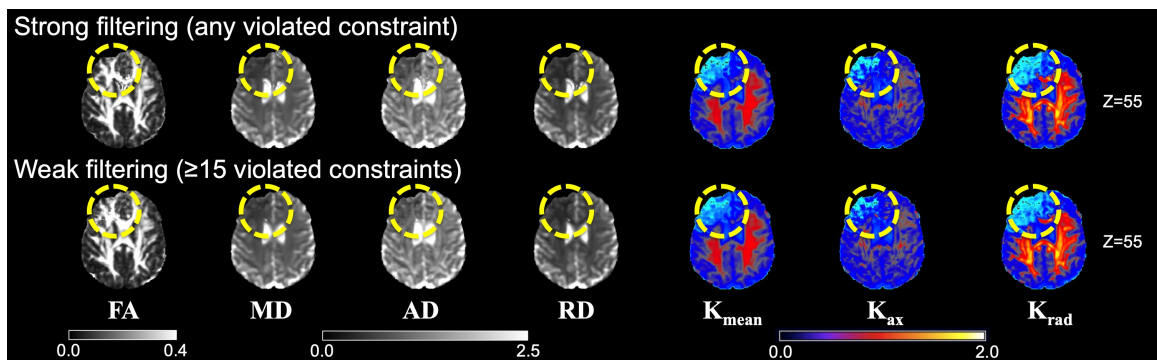
Fig. 4.4. Illustration of the outputs from strong and weak filtering in Diffusion Kurtosis Estimator [279]. In the highlighted region (yellow circle), weak filtering did not resolve the low quality of estimating kurtosis metrics.

4.3 Retrospective Harmonization

To investigate WM microstructure of adolescent collision-sport athletes at large scale, the DWI data acquired from different sites and with varying parameters need to be harmonized. As is outlined in Section 1.3, diffusion MRI measures are prone to different scanners [106], changes in TE [107–109, 113], and other confounding factors such as vendor, bandwidth, and interaction between coil and signal-to-noise ratio [107]. The longitudinal DWI data at PNG was complicated by an increase in TE of $\tilde{1}7$ms in scanning protocol since the 2015–2016 competition season, and by the migration from InnerVision Imaging Center to the new Engineering MRI Facility in March 2017. Although the reliability of aggregating DTI measures from the two sites was supported by a study of 24 traveling subjects [280], the study was based on a standardized protocol (TE=100ms) and did not address aggregating DWI data acquired with different TE. To date, many harmonization techniques for diffusion MRI have been proposed, and a thorough review can be found in [281]. This section will focus on two types of harmonization techniques and introduce one public dataset where the techniques can be developed and validated.

Harmonizing Parametric Maps: ComBat and ComBat-based Techniques

ComBat (a.k.a. Combined association test) is a statistical tool initially developed to correct for batch effect in gene expression analysis [282]. In recent years, ComBat has gained popularity in harmonizing MRI data [111, 283, 284], by removing variability introduced by sites and scanners in parametric maps, and meanwhile preserving biological variability.

Let y_{ijk} denote the observed DTI measure of site i, subject j, and region k [111]:

$$y_{ijk} = f_k(X_{ij}) + \gamma_{ik} + \delta_{ik}e_{ijk}$$

where

$$f_k(X_{ij}) = \hat{\alpha}_k + X_{ij}\hat{\beta}_k$$

In the linear function $f_k(X_{ij})$, $\hat{\alpha}_k$ is the intercept of the observed DTI measure, X_{ij} is a vector of biologically relevant covariates (e.g. age and sex), and $\hat{\beta}_k$ are the regression coefficients of X_{ij}. γ_{ik} and δ_{ik} are the site-effect parameters, where γ_{ik} is the mean of site effects and has a Gaussian distribution, and δ_{ik} is the variance of site effects and has an inverse gamma distribution. The two site-effect parameters are estimated empirically (denoted as γ_{ik}^* and δ_{ik}^*). The error term, e_{ijk}, is assumed to be normally distributed. In the final step, Bayesian analysis is applied to correct harmonization by its prior distributions. The ComBat harmonization for y_{ijk} is expressed as [111]:

$$y_{ijk}^{\text{ComBat}} = \frac{y_{ijk} - f_k(X_{ij}) - \gamma_{ik}^*}{\delta_{ik}^*} + f_k(X_{ij})$$

ComBat provides a flexible framework where non-linear or non-parametric methods can be incorporated to account for complexities of empirical data in different conditions. ComBat-GAM is one of such modified techniques, which utilizes Generalized Additive Model (GAM) and has been proposed to adjust for the nonlinear age effects in cortical and sub-cortical structures. Specifically, $f_k(X_{ij})$ is substituted by a non-linear function of covariates age x, sex z, and intracranial volume w [285]:

$$f_k(x_{ij}, z_{ij}, w_{ij}) = a_k + f(x_{ij}) + b_k * z_{ij} + c_k * w_{ij}$$

which leads to ComBat-GAM [285]:

$$y_{ijk}^{\text{ComBat-GAM}} = \frac{y_{ijk} - f_k(x_{ij}, z_{ij}, w_{ij}) - \gamma_{ik}^*}{\delta_{ik}^*} + f_k(x_{ij}, z_{ij}, w_{ij})$$

Another ComBat-based technique is called CovBat (a.k.a. Correcting covariance batch effects), which has been proposed to harmonize regional measures of cortical thickness by considering the covariance of scanner effects [286]:

$$y_{ijk}^{\text{CovBat}} = e_{ijk}^{\text{CovBat}} + \hat{\alpha}_k + X_{ij}\hat{\beta}_k$$

e_{ijk}^{CovBat} is the CovBat-adjusted residual based on the ComBat-adjusted residuals [286]:

$$\boldsymbol{e}_{ij}^{\text{ComBat}} = (e_{ij1}^{\text{ComBat}}, e_{ij2}^{\text{ComBat}}, ..., e_{ijk}^{\text{ComBat}})^T$$

where

$$e_{ijk}^{\text{ComBat}} = \frac{y_{ijk} - f_k(X_{ij}) - \gamma_{ik}^*}{\delta_{ik}^*}$$

Assuming that the covariance matrices of $\boldsymbol{e}_{ij}^{\text{ComBat}}$ are different across scanners, principle component analysis is employed on the covariance matrix of the full-data to reduce dimensions and capture the main variability. For details, see [286].

In the future, it is expected that ComBat and ComBat-based techniques can be applied to harmonize parametric maps of DWI data at voxel level. However, it is also worth noting that because these techniques take parametric maps as inputs, harmonization may be prone to cases where brain images exhibit structural alterations or pathological conditions [285], and where assumptions on parametric prior distributions are violated [112].

Harmonizing DWI: Rotation Invariant Spherical Harmonics (RISH)

Unlike techniques that harmonize parametric maps, rotation invariant spherical harmonics (RISH) [113] is a model-free approach that directly tackle DWI signal. RISH was proposed by Mirzaalian et al. [113] and has demonstrated good performance in harmonizing multi-site DWI data in parcellated brain regions [114]. Recently, Karayumak et al. [112] improved RISH to account for different acquisition parameters and be implemented at voxel level. The mathematical formulation of RISH has been well documented in [112, 281]. In brief, RISH features are obtained by representing DWI signal with a set of spherical harmonics basis functions, and harmonization is achieved by scaling the RISH features at each harmonic order from target site to reference site, where the scaling is based on the RISH feature templates, at each harmonic order, that are learned from the subset of subjects [112].

There are several technical issues for RISH harmonization. In principle, the DWI acquisition parameters cannot be too different; for example, different number of diffusion-encoding directions may lead to different set of harmonic orders and complicate the scaling process. To ensure good scaling, the RISH feature templates should be learned from at least 20 subjects who are ideally scanned at both sites ("travelling subjects"), which limits its applicability to datasets with fewer subjects and without travelling subject. Although subset of age- and sex-matched subjects can be used, the learned templates potentially introduce larger deformation and misregistration in the scaling process [287]. A population-specific DTI template (e.g. Fig. 2.2B) may serve as a common space for the learned templates without traveling subject, but this warrants evaluation in the future.

The Adolescent Brain Cognitive Development (ABCD) Study

The ABCD Study (`https://abcdstudy.org/`), by far the largest longitudinal study of brain development and child health in the United States, presents an ideal database for investigating data harmonization techniques. The Study has recruited over 11,500 children ages 9-10, collected at 21 research sites across the country, using the major MR scanner platforms (GE, Siemens, Philips). Neuroimaging data of the ABCD Study include high-resolution structural MRI, advanced diffusion MRI, resting-state and task-based fMRI.

It is anticipated that the ABCD Study will facilitate our scanner harmonization efforts at PNG. Over the past eleven years, PNG has collected over 1,800 MRI datasets from more than 550 participants, including both collision and non-collision sport athletes. The neuroimaging datasets include structural MRI, diffusion MRI, fMRI, and MRS. When harmonizing these datasets, the focus would be to preserve the multiple levels of information in the data, so as to allow tracking and modeling the dynamic process of neural injury and repair in adolescent brain. Having access to the ABCD Study Release 3.0 data will facilitate investigations for the upgrade from a GE Signa HDx 3T to a GE MR750 3T scanner at Purdue, and additional factors to be considered include different sites, head coil designs, longitudinal brain developmental trajectories, practice effects in task-based fMRI, image quality, etc. To avoid outcome-based publication and researcher bias, our analytic approaches can first be proposed as a Registered Report (`https://cos.io/rr/`).

4.4 Neurocognitive Prediction

Understanding how intelligence relates to brain structure during adolescence is an important topic in cognitive neuroscience. In 2019, a group of researchers initiated the ABCD Neurocognitive Prediction Challenge (`https://sibis.sri.com/abcd-np-challenge/`). Participating teams of the Challenge proposed algorithms that predict the residualized fluid intelligence scores of children ages 9–10, using the structural MRI data. We proposed a novel framework that applied 3D convolutional neural networks (ConvNets) to predict individual fluid intelligence scores, and our work won the 4th place at the final leaderboard. Our findings demonstrated that machine learning can be applied in the domains of neuroimaging and cognitive neuroscience, reveal insights about brain development and child health, and ultimately help us better unravel the relations between brain and behavior. A documentation of the proposed framework can be found at Appendix C.

The proposed 3D ConvNets framework can be translated to the PNG longitudinal database, which incorporates neurocognitive tests of verbal memory, visual memory, visual motor speed, reaction time, impulse control, and tests of working memory (see Section 1.2). It is worthwhile to explore the different grey matter labels in the PNG atlases, namely the Desikan-Killiany atlas (Fig. 2.3), Desikan-Killiany-Tourville atlas (Fig. 4.1), and Destrieux atlas (Fig. 4.2), to see what brain regions contribute to intelligence prediction. Again, a good predictive outcome critically depends on rigorous evaluations on the brain segmentations [272] (see Section 4.1), and the proposed framework can be continuously validated and improved in the future.

REFERENCES

[1] M. A. McCrea, *Mild Traumatic Brain Injury and Postconcussion Syndrome: The New Evidence Base for Diagnosis and Treatment.* New York: Oxford University Press, 2008.

[2] E. S. Sussman, A. V. Pendharkar, A. L. Ho, and J. Ghajar, "Mild traumatic brain injury and concussion: terminology and classification," *Handbook of Clinical Neurology*, vol. 158, pp. 21–24, 2018.

[3] G. Teasdale and B. Jennett, "Assessment of coma and impaired consciousness. A practical scale," *Lancet*, vol. 2, no. 7872, pp. 81–84, 1974.

[4] F. Servadei, G. Teasdale, and G. Merry, "Defining Acute Mild Head Injury in Adults: A Proposal Based on Prognostic Factors, Diagnosis, and Management," *J Neurotrauma*, vol. 18, no. 7, pp. 657–664, 2002.

[5] J. Bruns and W. A. Hauser, "The epidemiology of traumatic brain injury: a review." *Epilepsia*, vol. 44, no. s10, pp. 2–10, 2003.

[6] J. J. Bazarian, J. McClung, M. N. Shah, Y. T. Cheng, W. Flesher, and J. Kraus, "Mild traumatic brain injury in the United States, 1998-2000," *Brain Injury*, vol. 19, no. 2, pp. 85–91, 2005.

[7] J. D. Cassidy, L. J. Carroll, P. M. Peloso, J. Borg, H. von Holst, L. Holm, J. Kraus, V. G. Coronado, and WHO Collaborating Centre Task Force on Mild Traumatic Brain Injury, "Incidence, risk factors and prevention of mild traumatic brain injury: results of the WHO Collaborating Centre Task Force on Mild Traumatic Brain Injury." *J Rehabil Med*, no. 43 Suppl, pp. 28–60, 2004.

[8] J. A. Langlois, W. Rutland-Brown, and M. M. Wald, "The epidemiology and impact of traumatic brain injury: a brief overview," *J Head Trauma Rehabil*, vol. 21, no. 5, pp. 375–378, 2006.

[9] J. Orchard, T. Wood, H. Seward, and A. Broad, "Comparison of injuries in elite senior and junior Australian football," *J Sci Med Sport*, vol. 1, no. 2, pp. 83–88, 1998.

[10] J. C. Maroon, M. Field, M. Lovell, M. Collins, and J. Bost, "The evaluation of athletes with cerebral concussion," *Clin Neurosurg*, vol. 49, pp. 319–332, 2002.

[11] C. C. Giza, J. S. Kutcher, S. Ashwal, J. Barth, T. S. Getchius, G. A. Gioia, G. S. Gronseth, K. Guskiewicz, S. Mandel, G. Manley, D. B. McKeag, D. J. Thurman, and R. Zafonte, "Summary of evidence-based guideline update: evaluation and management of concussion in sports: report of the Guideline Development Subcommittee of the American Academy of Neurology," *Neurology*, vol. 80, no. 24, pp. 2250–2257, 2013.

[12] E. L. Yuh, G. W. Hawryluk, and G. T. Manley, "Imaging concussion: a review," *Neurosurgery*, vol. 75 Suppl 4, pp. 50–63, 2014.

[13] D. J. Thurman, C. M. Branche, and J. E. Sniezek, "The epidemiology of sports-related traumatic brain injuries in the United States: recent developments," *J Head Trauma Rehabil*, vol. 13, no. 2, pp. 1–8, 1998.

[14] M. Field, M. W. Collins, M. R. Lovell, and J. Maroon, "Does age play a role in recovery from sports-related concussion? A comparison of high school and collegiate athletes." *J Pediatr*, vol. 142, no. 5, pp. 546–553, 2003.

[15] M. McCrea, T. Hammeke, G. Olsen, P. Leo, and K. Guskiewicz, "Unreported concussion in high school football players: implications for prevention," *Clin J Sport Med*, vol. 14, no. 1, pp. 13–17, 2004.

[16] I. J. Williamson and D. Goodman, "Converging evidence for the under-reporting of concussions in youth ice hockey," *Br J Sports Med*, vol. 40, no. 2, pp. 128–132, 2006.

[17] M. E. Halstead and K. D. Walter, "American Academy of Pediatrics. Clinical report–sport-related concussion in children and adolescents," *Pediatrics*, vol. 126, no. 3, pp. 597–615, 2010.

[18] W. P. r. Meehan, R. C. Mannix, M. J. O'Brien, and M. W. Collins, "The prevalence of undiagnosed concussions in athletes," *Clin J Sport Med*, vol. 23, no. 5, pp. 339–342, 2013.

[19] C. M. Baugh, P. T. Kiernan, E. Kroshus, D. H. Daneshvar, P. H. Montenigro, A. C. McKee, and R. A. Stern, "Frequency of head-impact-related outcomes by position in NCAA division I collegiate football players," *J Neurotrauma*, vol. 32, no. 5, pp. 314–326, 2015.

[20] P. McCrory, W. Meeuwisse, J. Dvořák, M. Aubry, J. Bailes, S. Broglio, R. C. Cantu, D. Cassidy, R. J. Echemendia, R. J. Castellani, G. A. Davis, R. Ellenbogen, C. Emery, L. Engebretsen, N. Feddermann-Demont, C. C. Giza, K. M. Guskiewicz, S. Herring, G. L. Iverson, K. M. Johnston, J. Kissick, J. Kutcher, J. J. Leddy, D. Maddocks, M. Makdissi, G. T. Manley, M. McCrea, W. P. Meehan, S. Nagahiro, J. Patricios, M. Putukian, K. J. Schneider, A. Sills, C. H. Tator, M. Turner, and P. E. Vos, "Consensus statement on concussion in sport-the 5th international conference on concussion in sport held in Berlin, October 2016." *Br J Sports Med*, vol. 51, no. 11, pp. 838–847, 2017.

[21] G. J. Larrabee, "Neuropsychological Outcome, Post Concussion Symptoms, and Forensic Considerations in Mild Closed Head Trauma," *Semin Clin Neuropsychiatry*, vol. 2, no. 3, pp. 196–206, 1997.

[22] World Health Organization, "International Statistical Classification of Disease and Related Health Problems 10th Revision (ICD-10 Version:2016): postconcussional syndrome." [Online]. Available: http://apps.who.int/classifications/icd10/browse/2016/en

[23] M. P. Alexander, "Mild traumatic brain injury: pathophysiology, natural history, and clinical management," *Neurology*, vol. 45, no. 7, pp. 1253–1260, 1995.

[24] P. S. Satz, M. S. Alfano, R. F. Light, H. F. Morgenstern, K. F. Zaucha, R. F. Asarnow, and S. Newton, "Persistent Post-Concussive Syndrome: A proposed methodology and literature review to determine the effects, if any, of mild head and other bodily injury," *J Clin Exp Neuropsychol*, vol. 21, no. 5, pp. 620–628, 1999.

[25] S. McCullagh and A. Feinstein, "Outcome after mild traumatic brain injury: an examination of recruitment bias," *J Neurol Neurosurg Psychiatry*, vol. 74, no. 1, pp. 39–43, 2003.

[26] J. Kamins, E. Bigler, T. Covassin, L. Henry, S. Kemp, J. J. Leddy, A. Mayer, M. Mc-Crea, M. Prins, K. J. Schneider, T. C. McLeod, R. Zemek, and C. C. Giza, "What is the physiological time to recovery after concussion? A systematic review," *British Journal of Sports Medicine*, vol. 51, no. 12, pp. 935–940, 2017.

[27] S. Kashluba, J. E. Casey, and C. Paniak, "Evaluating the utility of ICD-10 diagnostic criteria for postconcussion syndrome following mild traumatic brain injury," *J Int Neuropsychol Soc*, vol. 12, no. 1, pp. 111–118, 2006.

[28] American Psychiatric Association, *Diagnostic and statistical manual of mental disorders (5th ed.)*. Washington, DC: American Psychiatric Association, 2013.

[29] J. E. Bailes, A. L. Petraglia, B. I. Omalu, E. Nauman, and T. Talavage, "Role of subconcussion in repetitive mild traumatic brain injury." *Journal of Neurosurgery*, vol. 119, no. 5, pp. 1235–1245, 2013.

[30] E. A. Nauman and T. M. Talavage, "Subconcussive trauma," *Handbook of Clinical Neurology*, vol. 158, pp. 245–255, 2018.

[31] B. E. Gavett, R. A. Stern, and A. C. McKee, "Chronic Traumatic Encephalopathy: A Potential Late Effect of Sport-Related Concussive and Subconcussive Head Trauma," *Clinics in Sports Medicine*, vol. 30, no. 1, pp. 179–188, 2011.

[32] T. M. Talavage, E. A. Nauman, and L. J. Leverenz, "The role of medical imaging in the recharacterization of mild traumatic brain injury using youth sports as a laboratory," *Frontiers in Neurology*, vol. 6, p. 273, 2016.

[33] B. E. Hagel, I. B. Pless, C. Goulet, R. W. Platt, and Y. Robitaille, "Effectiveness of helmets in skiers and snowboarders: case-control and case crossover study," *BMJ*, vol. 330, no. 7486, p. 281, 2005.

[34] J. S. Torg, J. Truex R., T. C. Quedenfeld, A. Burstein, A. Spealman, and r. Nichols C., "The National Football Head and Neck Injury Registry. Report and conclusions 1978," *Journal of the American Medical Association*, vol. 241, no. 14, pp. 1477–1479, 1979.

[35] K. Strimbu and J. A. Tavel, "What are biomarkers?" *Current Opinion in HIV and AIDS*, vol. 5, no. 6, pp. 463–466, 2010.

[36] K. Kawata, R. Tierney, and D. Langford, "Blood and cerebrospinal fluid biomarkers," *Handbook of Clinical Neurology*, vol. 158, pp. 217–233, 2018.

[37] A. K. Suri and M. L. Lipton, "Neuroimaging of brain trauma in sports," *Handbook of Clinical Neurology*, vol. 158, pp. 205–216, 2018.

[38] L. L. Mechtler, K. K. Shastri, and K. E. Crutchfield, "Advanced neuroimaging of mild traumatic brain injury," *Neurol Clin*, vol. 32, no. 1, pp. 31–58, 2014.

[39] C. C. Giza and D. A. Hovda, "The new neurometabolic cascade of concussion." *Neurosurgery*, vol. 75 Suppl 4, pp. S24–33, 2014.

[40] E. H. Pettus and J. T. Povlishock, "Characterization of a distinct set of intra-axonal ultrastructural changes associated with traumatically induced alteration in axolemmal permeability," *Brain Research*, vol. 722, no. 1-2, pp. 1–11, 1996.

[41] G. Barkhoudarian, D. A. Hovda, and C. C. Giza, "The Molecular Pathophysiology of Concussive Brain Injury," *Clinics in Sports Medicine*, vol. 30, no. 1, pp. 33–48, 2011.

[42] C. C. Giza and D. A. Hovda, "The Neurometabolic Cascade of Concussion," *Journal of Athletic Training*, vol. 36, no. 3, pp. 228–235, 2001.

[43] K. K. Wang, Z. Yang, T. Zhu, Y. Shi, R. Rubenstein, J. A. Tyndall, and G. T. Manley, "An update on diagnostic and prognostic biomarkers for traumatic brain injury," *Expert Review of Molecular Diagnostics*, vol. 18, no. 2, pp. 165–180, 2018.

[44] Z. Metting, N. Wilczak, L. A. Rodiger, J. M. Schaaf, and J. Van Der Naalt, "GFAP and S100B in the acute phase of mild traumatic brain injury," *Neurology*, vol. 78, no. 18, pp. 1428–1433, 2012.

[45] L. Papa, G. M. Brophy, R. D. Welch, L. M. Lewis, C. F. Braga, C. N. Tan, N. J. Ameli, M. A. Lopez, C. A. Haeussler, D. I. Mendez Giordano, S. Silvestri, P. Giordano, K. D. Weber, C. Hill-Pryor, and D. C. Hack, "Time Course and Diagnostic Accuracy of Glial and Neuronal Blood Biomarkers GFAP and UCH-L1 in a Large Cohort of Trauma Patients With and Without Mild Traumatic Brain Injury." *JAMA neurology*, vol. 73, no. 5, pp. 551–560, 2016.

[46] M. McCrea, S. P. Broglio, T. W. McAllister, J. Gill, C. C. Giza, D. L. Huber, J. Harezlak, K. L. Cameron, M. N. Houston, G. McGinty, J. C. Jackson, K. Guskiewicz, J. Mihalik, M. A. Brooks, S. Duma, S. Rowson, L. D. Nelson, P. Pasquina, T. B. Meier, and the CARE Consortium Investigators, "Association of Blood Biomarkers With Acute Sport-Related Concussion in Collegiate Athletes: Findings From the NCAA and Department of Defense CARE Consortium," *JAMA Network Open*, vol. 3, no. 1, p. e1919771, 2020.

[47] L. Papa, L. Akinyi, M. C. Liu, J. A. Pineda, J. J. Tepas, M. W. Oli, W. Zheng, G. Robinson, S. A. Robicsek, A. Gabrielli, S. C. Heaton, H. J. Hannay, J. A. Demery, G. M. Brophy, J. Layon, C. S. Robertson, R. L. Hayes, and K. K. Wang, "Ubiquitin C-terminal hydrolase is a novel biomarker in humans for severe traumatic brain injury," *Critical Care Medicine*, vol. 38, no. 1, pp. 138–144, 2010.

[48] E. F. Ellis, K. A. Willoughby, S. A. Sparks, and T. Chen, "S100B protein is released from rat neonatal neurons, astrocytes, and microglia by in vitro trauma and anti-S100 increases trauma-induced delayed neuronal injury and negates the protective effect of exogenous S100B on neurons," *Journal of Neurochemistry*, vol. 101, no. 6, pp. 1463–1470, 2007.

[49] A. K. Ottens, E. C. Golden, L. Bustamante, R. L. Hayes, N. D. Denslow, and K. K. Wang, "Proteolysis of multiple myelin basic protein isoforms after neurotrauma: Characterization by mass spectrometry," *Journal of Neurochemistry*, vol. 104, no. 5, pp. 1404–1414, 2008.

[50] Y. Li, L. Zhang, S. Kallakuri, A. Cohen, and J. M. Cavanaugh, "Correlation of mechanical impact responses and biomarker levels: A new model for biomarker evaluation in TBI," *Journal of the Neurological Sciences*, vol. 359, no. 1-2, pp. 280–286, 2015.

[51] D. K. Wright, J. Trezise, A. Kamnaksh, R. Bekdash, L. A. Johnston, R. Ordidge, B. D. Semple, A. J. Gardner, P. Stanwell, T. J. O'Brien, D. V. Agoston, and S. R. Shultz, "Behavioral, blood, and magnetic resonance imaging biomarkers of experimental mild traumatic brain injury," *Scientific Reports*, vol. 6, p. 28713, 2016.

[52] J. Gaiottino, N. Norgren, R. Dobson, J. Topping, A. Nissim, A. Malaspina, J. P. Best-wick, A. U. Monsch, A. Regeniter, R. L. Lindberg, L. Kappos, D. Leppert, A. Petzold, G. Giovannoni, and J. Kuhle, "Increased Neurofilament Light Chain Blood Levels in Neurodegenerative Neurological Diseases," *PLoS One*, vol. 8, no. 9, p. e75091, 2013.

[53] P. Shahim, A. Politis, A. van der Merwe, B. Moore, Y.-Y. Chou, D. L. Pham, J. A. Butman, R. Diaz-Arrastia, J. M. Gill, D. L. Brody, H. Zetterberg, K. Blennow, and L. Chan, "Neurofilament light as a biomarker in traumatic brain injury," *Neurology*, 2020. [Online]. Available: https://n.neurology.org/content/early/2020/07/08/WNL. 0000000000009983

[54] R. Rubenstein, B. Chang, P. Davies, A. K. Wagner, C. S. Robertson, and K. K. Wang, "A Novel, Ultrasensitive Assay for Tau: Potential for Assessing Traumatic Brain Injury in Tissues and Biofluids," *J Neurotrauma*, vol. 32, no. 5, pp. 342–352, 2015.

[55] R. Rubenstein, D. R. Sharma, B. Chang, N. Oumata, M. Cam, L. Vaucelle, M. F. Lindberg, A. Chiu, T. Wisniewski, K. K. W. Wang, and L. Meijer, "Novel Mouse Tauopathy Model for Repetitive Mild Traumatic Brain Injury: Evaluation of Long-Term Effects on Cognition and Biomarker Levels After Therapeutic Inhibition of Tau Phosphorylation," *Frontiers in Neurology*, vol. 10, p. 124, 2019.

[56] M. McCrea, T. Meier, D. Huber, A. Ptito, E. Bigler, C. T. Debert, G. Manley, D. Menon, J.-K. Chen, R. Wall, K. J. Schneider, and T. McAllister, "Role of advanced neuroimaging, fluid biomarkers and genetic testing in the assessment of sport-related concussion: a systematic review," *British Journal of Sports Medicine*, vol. 51, no. 12, pp. 919–929, 2017.

[57] J. P. Posti, I. Hossain, R. S. K. Takala, H. Liedes, V. Newcombe, J. Outtrim, A. J. Katila, J. Frantzén, H. Ala-Seppälä, J. P. Coles, A. Kyllönen, H.-R. Maanpää, J. Tallus, P. J. Hutchinson, M. van Gils, D. K. Menon, O. Tenovuo, and T. Investigators, "Glial Fibrillary Acidic Protein and Ubiquitin C-Terminal Hydrolase-L1 Are Not Specific Biomarkers for Mild CT-Negative Traumatic Brain Injury," *Journal of Neurotrauma*, vol. 34, no. 7, pp. 1427–1438, 2017. [Online]. Available: https://doi.org/10.1089/neu.2016.4442

[58] J. R. Huie, R. Diaz-Arrastia, J. K. Yue, M. D. Sorani, A. M. Puccio, D. O. Okonkwo, G. T. Manley, A. R. Ferguson, O. M. Adeoye, N. Badjatia, K. D. Boase, Y. Bodien-Guller, M. R. Bullock, R. M. Chesnut, J. D. Corrigan, K. L. Crawford, R. Diaz-Arrastia, S. S. Dikmen, A.-C. Duhaime, R. G. Ellenbogen, F. Ezekiel, V. R. Feeser, J. T. Giacino, D. P. Goldman, L. Gonzales, S. P. Gopinath, R. P. Gullapalli, J. C. Hemphill, G. A. Hotz, J. H. Kramer, H. Levin, C. J. Lindsell, J. Machamer, C. Madden, A. J. Markowitz, A. Martin, B. E. Mathern, T. W. McAllister, M. A. McCrea, R. E. Merchant, F. Noel, D. P. Perl, A. M. Puccio, M. Rabinowitz, C. S. Robertson, J. Rosand, A. M. Sander, G. Satris, D. M. Schnyer, S. A. Seabury, P. Sergot, M. Sherer, D. M. Stein, M. B. Stein, S. R. Taylor, N. R. Temkin, A. W. Toga, L. C. Turtzo, P. M. Vespa, K. K. Wang, R. Zafonte, and Z. Zhang, "Testing a Multivariate Proteomic Panel for Traumatic Brain Injury Biomarker Discovery: A TRACK-TBI Pilot Study," *J Neurotrauma*, vol. 36, no. 1, pp. 100–110, 2018.

[59] S. N. Niogi, P. Mukherjee, J. Ghajar, C. Johnson, R. A. Kolster, R. Sarkar, H. Lee, M. Meeker, R. D. Zimmerman, G. T. Manley, and B. D. McCandliss, "Extent of microstructural white matter injury in postconcussive syndrome correlates with impaired cognitive reaction time: A 3T diffusion tensor imaging study of mild traumatic brain injury," *American Journal of Neuroradiology*, vol. 29, no. 5, pp. 967–973, 2008.

[60] E. Chamard, M. Lassonde, L. Henry, J. Tremblay, Y. Boulanger, L. De Beaumont, and H. Théoret, "Neurometabolic and microstructural alterations following a sports-related concussion in female athletes," *Brain Injury*, vol. 27, no. 9, pp. 1038–46, 2013.

[61] M. L. Lipton, N. Kim, M. E. Zimmerman, M. Kim, W. F. Stewart, C. A. Branch, and R. B. Lipton, "Soccer heading is associated with white matter microstructural and cognitive abnormalities," *Radiology*, vol. 268, no. 3, pp. 850–857, 2013.

[62] V. N. Poole, K. Abbas, T. E. Shenk, E. L. Breedlove, K. M. Breedlove, M. E. Robinson, L. J. Leverenz, E. A. Nauman, T. M. Talavage, and U. Dydak, "MR Spectroscopic Evidence of Brain Injury in the Non-Diagnosed Collision Sport Athlete," *Developmental Neuropsychology*, vol. 39, no. 6, pp. 459–473, 2014.

[63] S. Bari, D. O. Svaldi, I. Jang, T. E. Shenk, V. N. Poole, T. Lee, U. Dydak, J. V. Rispoli, E. A. Nauman, and T. M. Talavage, "Dependence on subconcussive impacts of brain metabolism in collision sport athletes: an MR spectroscopic study," *Brain Imaging and Behavior*, vol. 13, no. 3, pp. 735–749, 2019.

[64] T. M. Talavage, E. A. Nauman, E. L. Breedlove, U. Yoruk, A. E. Dye, K. E. Morigaki, H. Feuer, and L. J. Leverenz, "Functionally-Detected Cognitive Impairment in High School Football Players without Clinically-Diagnosed Concussion," *Journal of Neurotrauma*, vol. 31, no. 4, pp. 327–338, 2014. [Online]. Available: https://doi.org/10.1089/neu.2010.1512

[65] K. Abbas, T. E. Shenk, V. N. Poole, E. L. Breedlove, L. J. Leverenz, E. A. Nauman, T. M. Talavage, and M. E. Robinson, "Alteration of default mode network in high school football athletes due to repetitive subconcussive mild traumatic brain injury: a resting-state functional magnetic resonance imaging study." *Brain Connectivityonnectivity*, vol. 5, no. 2, pp. 91–101, 2015.

[66] J. B. Andre, "Arterial Spin Labeling Magnetic Resonance Perfusion for Traumatic Brain Injury: Technical Challenges and Potentials," *Top Magn Reson Imaging*, vol. 24, no. 5, pp. 275–287, 2015.

[67] L. Moore, "Sagamore Parkway bridge closes one lane from April to August," 2019. [Online]. Available: https://www.jconline.com/story/news/2019/03/25/sagamore-parkway-bridge-into-west-lafayette-closes-one-lane-summer/3267506002/

[68] M. C. H. Hui and D. Yau, "Major bridge development in Hong Kong, China-past, present and future," *Frontiers of Architecture and Civil Engineering in China*, vol. 5, no. 4, p. 405414, 2011.

[69] A. G. Gross, "A New Theory on the Dynamics of Brain Concussion and Brain Injury," *Journal of Neurosurgery*, vol. 15, no. 5, pp. 548–561, 1958.

[70] Z.-H. Liang and D.-Z. Yin, "Preventive Treatment of Traditional Chinese Medicine As Antistress and Antiaging Strategy," *Rejuvenation Research*, vol. 13, no. 2-3, pp. 248–252, 2009.

[71] P. Unschuld, *Huang Di Nei Jing Su Wen: Nature, Knowledge, Imagery in an Ancient Chinese Medical Text*. Berkeley: University of California Press, 2003.

[72] D. W. McRobbie, E. A. Moore, M. J. Graves, and M. R. Prince, *MRI - from picture to proton*. Cambridge: Cambridge University Press, 2003.

[73] D. Nishimura, *Principles of magnetic resonance imaging*. Stanford, CA: Stanford University Press, 1996.

[74] E. A. Nauman, K. M. Breedlove, E. L. Breedlove, T. M. Talavage, M. E. Robinson, and L. J. Leverenz, "Post-season neurophysiological deficits assessed by ImPACT and fMRI in athletes competing in American football," *Developmental Neuropsychology*, vol. 40, no. 2, pp. 85–91, 2015.

[75] I. Y. Chun, X. Mao, E. L. Breedlove, L. J. Leverenz, E. A. Nauman, and T. M. Talavage, "DTI Detection of Longitudinal WM Abnormalities Due to Accumulated Head Impacts," *Developmental Neuropsychology*, vol. 40, no. 2, pp. 92–97, 2015.

[76] D. O. Svaldi, E. C. McCuen, C. Joshi, M. E. Robinson, Y. Nho, R. Hannemann, E. A. Nauman, L. J. Leverenz, and T. M. Talavage, "Cerebrovascular reactivity changes in asymptomatic female athletes attributable to high school soccer participation," *Brain Imaging and Behavior*, vol. 11, no. 1, pp. 98–112, 2017.

[77] D. O. Svaldi, C. Joshi, E. C. McCuen, J. P. Music, R. Hannemann, L. J. Leverenz, E. A. Nauman, and T. M. Talavage, "Accumulation of high magnitude acceleration events predicts cerebrovascular reactivity changes in female high school soccer athletes," *Brain Imaging and Behavior*, 2018.

[78] I. Jang, I. Y. Chun, J. R. Brosch, S. Bari, Y. Zou, B. R. Cummiskey, T. A. Lee, R. J. Lycke, V. N. Poole, T. E. Shenk, D. O. Svaldi, G. G. Tamer, U. Dydak, L. J. Leverenz, E. A. Nauman, and T. M. Talavage, "Every hit matters: White matter diffusivity changes in high school football athletes are correlated with repetitive head acceleration event exposure," *NeuroImage: Clinical*, vol. 24, p. 101930, 2019.

[79] B. W. Benson, G. M. Hamilton, W. H. Meeuwisse, P. McCrory, and J. Dvorak, "Is protective equipment useful in preventing concussion? A systematic review of the literature." *British Journal of Sports Medicine*, vol. 43 Suppl 1, pp. i56–67, 2009.

[80] D. W. Smith, J. E. Bailes, J. A. Fisher, J. Robles, R. C. Turner, and J. D. Mills, "Internal jugular vein compression mitigates traumatic axonal injury in a rat model by reducing the intracranial slosh effect," *Clin Neurosurg*, vol. 70, no. 3, pp. 740–746, 2012.

[81] J. G. Hobbs, J. S. Young, and J. E. Bailes, "Sports-related concussions: diagnosis, complications, and current management strategies," *Neurosurgical Focus*, vol. 40, no. 4, p. E5, 2016.

[82] E. L. Breedlove, M. Robinson, T. M. Talavage, K. E. Morigaki, U. Yoruk, K. O'Keefe, J. King, L. J. Leverenz, J. W. Gilger, and E. A. Nauman, "Biomechanical correlates of symptomatic and asymptomatic neurophysiological impairment in high school football," *Journal of Biomechanics*, vol. 45, no. 7, pp. 1265–1272, 2012.

[83] R. Jadischke, D. C. Viano, N. Dau, A. I. King, and J. McCarthy, "On the accuracy of the Head Impact Telemetry (HIT) System used in football helmets," *Journal of Biomechanics*, vol. 46, no. 13, pp. 2310–2315, 2013.

[84] B. Cummiskey, D. Schiffmiller, T. M. Talavage, L. Leverenz, J. J. Meyer, D. Adams, and E. A. Nauman, "Reliability and accuracy of helmet-mounted and head-mounted devices used to measure head accelerations," *Proceedings of the Institution of Mechanical Engineers, Part P: Journal of Sports Engineering and Technology*, vol. 231, no. 2, pp. 144–153, 2017.

[85] P. Tagliabue, "Tackling concussions in sports," *Neurosurgery*, vol. 53, no. 4, p. 796, 2004.

[86] M. R. Lovell, M. W. Collins, G. L. Iverson, M. Field, J. C. Maroon, R. Cantu, K. Podell, J. W. Powell, M. Belza, and F. H. Fu, "Recovery from mild concussion in high school athletes," *Journal of Neurosurgery*, vol. 98, no. 2, pp. 296–301, 2009.

[87] M. R. Lovell and M. W. Collins, "Neuropsychological assessment of the college football player," *J Head Trauma Rehabil*, vol. 13, no. 2, pp. 9–26, 1998.

[88] M. W. Collins, S. H. Grindel, M. R. Lovell, D. E. Dede, D. J. Moser, B. R. Phalin, S. Nogle, M. Wasik, D. Cordry, M. K. Daugherty, S. F. Sears, G. Nicolette, P. Indelicato, and D. B. McKeag, "Relationship between concussion and neuropsychological performance in college football players," *Journal of the American Medical Association*, vol. 282, no. 10, pp. 964–970, 1999.

[89] K. M. Breedlove, E. L. Breedlove, M. Robinson, V. N. Poole, J. R. King, P. Rosenberger, M. Rasmussen, T. M. Talavage, L. J. Leverenz, and E. A. Nauman, "Detecting Neurocognitive and Neurophysiological Changes as a Result of Subconcussive Blows Among High School Football Athletes," *Athletic Training & Sports Health Care*, vol. 6, no. 3, pp. 119–127, 2014.

[90] J. Resch, A. Driscoll, N. McCaffrey, C. Brown, M. S. Ferrara, S. Macciocchi, T. Baumgartner, and K. Walpert, "ImPact test-retest reliability: Reliably unreliable?" *Journal of Athletic Training*, vol. 48, no. 4, pp. 506–511, 2013.

[91] R. Elbin, V. Fazio-Sumrok, M. N. Anderson, N. R. D'Amico, A. Said, A. Grossel, P. Schatz, D. Lipinski, and M. Womble, "Evaluating the suitability of the Immediate Post-Concussion Assessment and Cognitive Testing (ImPACT) computerized neurocognitive battery for short-term, serial assessment of neurocognitive functioning," *Journal of Clinical Neuroscience*, vol. 62, pp. 138–141, 2019. [Online]. Available: https://www.sciencedirect.com/science/article/pii/S0967586818317296

[92] I. Pollack, L. B. Johnson, and P. R. Knaff, "Running memory span." *J Exp Psychol*, vol. 57, no. 3, pp. 137–146, 1959.

[93] P. E. Hallett, "Primary and secondary saccades to goals defined by instructions." *Vision research*, vol. 18, no. 10, pp. 1279–1296, 1978.

[94] F. Donders, "On the speed of mental processes," *Acta Psychologica*, vol. 30, pp. 412–431, 1969.

[95] C. Beaulieu, "The basis of anisotropic water diffusion in the nervous system - a technical review," *NMR Biomed*, vol. 15, no. 7-8, pp. 435–455, 2002.

[96] E. O. Stejskal and J. E. Tanner, "Spin diffusion measurements: Spin echoes in the presence of a time-dependent field gradient," *The Journal of Chemical Physics*, vol. 42, no. 1, pp. 288–292, 1965.

[97] P. Mukherjee, J. I. Berman, S. W. Chung, C. P. Hess, and R. G. Henry, "Diffusion tensor MR imaging and fiber tractography: Theoretic underpinnings," *Am J Neuroradiol*, vol. 29, no. 4, pp. 632–641, 2008.

[98] S. Chanraud, N. Zahr, E. V. Sullivan, and A. Pfefferbaum, "MR diffusion tensor imaging: A window into white matter integrity of the working brain," *Neuropsychology Review*, vol. 20, no. 2, pp. 209–225, 2010.

[99] A. Pfefferbaum and E. V. Sullivan, "Disruption of brain white matter microstructure by excessive intracellular and extracellular fluid in alcoholism: Evidence from diffusion tensor imaging," *Neuropsychopharmacology*, vol. 30, no. 2, pp. 423–432, 2005.

[100] S. M. Smith, M. Jenkinson, H. Johansen-Berg, D. Rueckert, T. E. Nichols, C. E. Mackay, K. E. Watkins, O. Ciccarelli, M. Z. Cader, P. M. Matthews, and T. E. Behrens, "Tract-based spatial statistics: voxelwise analysis of multi-subject diffusion data," *Neuroimage*, vol. 31, no. 4, pp. 1487–1505, 2006.

[101] M. Bach, F. B. Laun, A. Leemans, C. M. Tax, G. J. Biessels, B. Stieltjes, and K. H. Maier-Hein, "Methodological considerations on tract-based spatial statistics (TBSS)," *NeuroImage*, vol. 100, pp. 358–369, 2014.

[102] P. Mukherjee, S. W. Chung, J. I. Berman, C. P. Hess, and R. G. Henry, "Diffusion tensor MR imaging and fiber tractography: Technical considerations," *Am J Neuroradiol*, vol. 29, no. 5, pp. 843–852, 2008.

[103] C. Thomas, F. Q. Ye, M. O. Irfanoglu, P. Modi, K. S. Saleem, D. A. Leopold, and C. Pierpaoli, "Anatomical accuracy of brain connections derived from diffusion MRI tractography is inherently limited," *Proceedings of the National Academy of Sciences*, vol. 111, no. 46, pp. 16 574–16 579, 2014.

[104] D. S. Tuch, T. G. Reese, M. R. Wiegell, N. Makris, J. W. Belliveau, and V. J. Wedeen, "High angular resolution diffusion imaging reveals intravoxel white matter fiber heterogeneity," *Magn Reson Med*, vol. 48, no. 4, pp. 577–582, 2002.

[105] C. P. Hess and P. Mukherjee, "Visualizing White Matter Pathways in the Living Human Brain: Diffusion Tensor Imaging and Beyond," *Neuroimaging Clinics of North America*, vol. 17, no. 4, pp. 407–426, 2007.

[106] A. S. Kivrak, Y. Paksoy, C. Erol, M. Koplay, S. Özbek, and F. Kara, "Comparison of apparent diffusion coefficient values among different MRI platforms: A multicenter phantom study," *Diagn Interv Radiol*, vol. 19, no. 6, pp. 433–437, 2013.

[107] C. Timmermans, D. Smeets, J. Verheyden, V. Terzopoulos, V. Anania, P. M. Parizel, and A. Maas, "Potential of a statistical approach for the standardization of multicenter diffusion tensor data: A phantom study," *Journal of Magnetic Resonance Imaging*, vol. 49, no. 4, pp. 955–965, 2019.

[108] W. Qin, C. S. Yu, F. Zhang, X. Y. Du, H. Jiang, Y. X. Yan, and K. C. Li, "Effects of echo time on diffusion quantification of brain white matter at 1.5T and 3.0T," *Magn Reson Med*, 2009.

[109] J. Veraart, D. S. Novikov, and E. Fieremans, "TE dependent Diffusion Imaging (TEdDI) distinguishes between compartmental T2 relaxation times," *NeuroImage*, 2018.

[110] D. S. Novikov, V. G. Kiselev, and S. N. Jespersen, "On modeling," *Magn Reson Med*, vol. 79, no. 6, pp. 3172–3193, 2018.

[111] J.-P. Fortin, D. Parker, B. Tunç, T. Watanabe, M. A. Elliott, K. Ruparel, D. R. Roalf, T. D. Satterthwaite, R. C. Gur, R. E. Gur, R. T. Schultz, R. Verma, and R. T. Shinohara, "Harmonization of multi-site diffusion tensor imaging data," *NeuroImage*, vol. 161, pp. 149–170, 2017.

[112] S. Cetin Karayumak, S. Bouix, L. Ning, A. James, T. Crow, M. Shenton, M. Kubicki, and Y. Rathi, "Retrospective harmonization of multi-site diffusion MRI data acquired with different acquisition parameters." *NeuroImage*, vol. 184, pp. 180–200, 2019.

[113] H. Mirzaalian, A. de Pierrefeu, P. Savadjiev, O. Pasternak, S. Bouix, M. Kubicki, C.-F. Westin, M. E. Shenton, and Y. Rathi, "Harmonizing Diffusion MRI Data Across Multiple Sites and Scanners." *Medical image computing and computer-assisted intervention : MICCAI ... International Conference on Medical Image Computing and Computer-Assisted Intervention*, vol. 9349, pp. 12–19, 2015.

[114] H. Mirzaalian, L. Ning, P. Savadjiev, O. Pasternak, S. Bouix, O. Michailovich, S. Karmacharya, G. Grant, C. E. Marx, R. A. Morey, L. A. Flashman, M. S. George, T. W. McAllister, N. Andaluz, L. Shutter, R. Coimbra, R. D. Zafonte, M. J. Coleman, M. Kubicki, C. F. Westin, M. B. Stein, M. E. Shenton, and Y. Rathi, "Multi-site harmonization of diffusion MRI data in a registration framework," *Brain Imaging and Behavior*, 2018.

[115] A. C. Evans, A. L. Janke, D. L. Collins, and S. Baillet, "Brain templates and atlases." *NeuroImage*, vol. 62, no. 2, pp. 911–922, 2012.

[116] K. Narvacan, S. Treit, R. Camicioli, W. Martin, and C. Beaulieu, "Evolution of deep gray matter volume across the human lifespan," *Human Brain Mapping*, vol. 38, no. 8, pp. 3771–3790, 2017.

[117] W. Van Hecke, A. Leemans, and L. Emsell, "DTI Analysis Methods: Voxel-Based Analysis," in *Diffusion Tensor Imaging: A Practical Handbook*, W. V. Hecke, L. Emsell, and S. Sunaert, Eds. Springer New York LLC, 2016, pp. 183–203.

[118] H. Ling and J. Hardy, "Neurological consequences of traumatic brain injuries in sports," *Molecular and Cellular Neuroscience*, vol. 66, pp. 114–122, 2015.

[119] E. A. Nauman, T. M. Talavage, and P. S. Auerbach, "Mitigating the Consequences of Subconcussive Head Injuries." *Annual review of biomedical engineering*, 2020.

[120] S. Zhang and K. Arfanakis, "Role of standardized and study-specific human brain diffusion tensor templates in inter-subject spatial normalization," *Journal of Magnetic Resonance Imaging*, vol. 37, no. 2, pp. 372–381, 2013.

[121] F. G. Ashby, *Statistical analysis of fMRI data.*, 1st ed. Cambridge: The MIT Press, 2011.

[122] J. Talairach and P. Tournoux, *Co-planar stereotaxic atlas of the human brain: 3-dimensional proportional system: an approach to cerebral imaging.* New York: Thieme, 1988.

[123] G. Grabner, A. L. Janke, M. M. Budge, D. Smith, J. Pruessner, and D. L. Collins, "Symmetric atlasing and model based segmentation: an application to the hippocampus in older adults." *Med Image Comput Comput Assist Interv*, vol. 9, no. Pt 2, pp. 58–66, 2006.

[124] L. Fan, H. Li, J. Zhuo, Y. Zhang, J. Wang, L. Chen, Z. Yang, C. Chu, S. Xie, A. R. Laird, P. T. Fox, S. B. Eickhoff, C. Yu, and T. Jiang, "The Human Brainnetome Atlas: A New Brain Atlas Based on Connectional Architecture," *Cerebral Cortex*, vol. 26, no. 8, pp. 3508–3526, 2016.

[125] S. Zhang and K. Arfanakis, "Evaluation of standardized and study-specific diffusion tensor imaging templates of the adult human brain: Template characteristics, spatial normalization accuracy, and detection of small inter-group FA differences," *NeuroImage*, vol. 172, pp. 40–50, 2018.

[126] T. Rohlfing, N. M. Zahr, E. V. Sullivan, and A. Pfefferbaum, "The SRI24 multichannel atlas of normal adult human brain structure," *Human Brain Mapping*, vol. 31, no. 5, pp. 798–819, 2010.

[127] R. P. Cabeen, M. E. Bastin, and D. H. Laidlaw, "A Comparative evaluation of voxel-based spatial mapping in diffusion tensor imaging," *NeuroImage*, vol. 146, pp. 100–112, 2017.

[128] D. A. Dickie, S. D. Shenkin, D. Anblagan, J. Lee, M. B. Cabez, D. Rodriguez, J. P. Boardman, A. Waldman, D. E. Job, and J. M. Wardlaw, "Whole Brain Magnetic Resonance Image Atlases: A Systematic Review of Existing Atlases and Caveats for Use in Population Imaging," *Frontiers in Neuroinformatics*, vol. 11, p. 1, 2017.

[129] T. L. Jernigan and P. Tallal, "Late childhood changes in brain morphology observable with MRI," *Developmental Medicine & Child Neurology*, vol. 32, no. 5, pp. 379–385, 1990.

[130] T. Paus, A. Zijdenbos, K. Worsley, D. Collins, J. Blumenthal, J. Giedd, J. Rapoport, and A. Evans, "Structural Maturation of Neural Pathways in Children and Adolescents: In Vivo Study," *Science*, vol. 283, no. 5409, pp. 1908–1911, 1999.

[131] A. Pfefferbaum, D. H. Mathalon, E. V. Sullivan, J. M. Rawles, R. B. Zipursky, and K. O. Lim, "A Quantitative Magnetic Resonance Imaging Study of Changes in Brain Morphology from Infancy to Late Adulthood," *Archives of Neurology*, vol. 51, no. 9, pp. 874–887, 1994.

[132] J. Richards and W. Xie, "Brains for All the Ages: Structural Neurodevelopment in Infants and Children from a Life-Span Perspective," *Adv Child Dev Behav*, vol. 48, pp. 1–52, 2015.

[133] B. B. Avants, J. T. Duda, E. Kilroy, K. Krasileva, K. Jann, B. T. Kandel, N. J. Tustison, L. Yan, M. Jog, R. Smith, Y. Wang, M. Dapretto, and D. J. Wang, "The pediatric template of brain perfusion," *Scientific data*, vol. 2, p. 150003, 2015.

[134] V. Fonov, A. C. Evans, K. Botteron, C. R. Almli, R. C. McKinstry, and D. L. Collins, "Unbiased average age-appropriate atlases for pediatric studies," *NeuroImage*, vol. 54, no. 1, pp. 313–327, 2011.

[135] N. Gogtay, J. N. Giedd, L. Lusk, K. M. Hayashi, D. Greenstein, A. C. Vaituzis, T. F. Nugent, D. H. Herman, L. S. Clasen, A. W. Toga, J. L. Rapoport, and P. M. Thompson, "Mapping adolescent brain change reveals dynamic wave of accelerated gray matter loss in very early-onset schizophrenia," *PNAS*, vol. 98, no. 20, pp. 11 650–11 655, 2004.

[136] C. E. Sanchez, J. E. Richards, and C. R. Almli, "Age-specific MRI templates for pediatric neuroimaging," *Developmental Neuropsychology*, vol. 37, pp. 379–399, 2012.

[137] D. Wu, T. Ma, C. Ceritoglu, Y. Li, J. Chotiyanonta, Z. Hou, J. Hsu, X. Xu, T. Brown, M. I. Miller, and S. Mori, "Resource atlases for multi-atlas brain segmentations with multiple ontology levels based on T1-weighted MRI," *NeuroImage*, vol. 125, pp. 120–130, 2016.

[138] T. Zhao, X. Liao, V. S. Fonov, Q. Wang, W. Men, Y. Wang, S. Qin, S. Tan, J. H. Gao, A. Evans, S. Tao, Q. Dong, and Y. He, "Unbiased age-specific structural brain atlases for Chinese pediatric population," *NeuroImage*, vol. 189, pp. 55–70, 2019.

[139] W. Van Hecke, A. Leemans, C. A. Sage, L. Emsell, J. Veraart, J. Sijbers, S. Sunaert, and P. M. Parizel, "The effect of template selection on diffusion tensor voxel-based analysis results," *NeuroImage*, vol. 55, no. 2, pp. 566–573, 2011.

[140] M. Bach, F. B. Laun, A. Leemans, C. M. Tax, G. J. Biessels, B. Stieltjes, and K. H. Maier-Hein, "Methodological considerations on tract-based spatial statistics (TBSS)," *NeuroImage*, vol. 100, pp. 358–369, 2014.

[141] B. L. Bartnik-Olson, B. Holshouser, H. Wang, M. Grube, K. Tong, V. Wong, and S. Ashwal, "Impaired neurovascular unit function contributes to persistent symptoms after concussion: a pilot study," *Journal of neurotrauma*, vol. 31, no. 17, pp. 1497–1506, 2014.

[142] T. A. Maugans, C. Farley, M. Altaye, J. Leach, and K. M. Cecil, "Pediatric sports-related concussion produces cerebral blood flow alterations," *Pediatrics*, vol. 129, no. 1, pp. 28–37, 2012.

[143] K. J. Nilsson, H. G. Flint, Y. Gao, L. Kendrick, S. Cutchin, R. Pentecost, and K. Pardue, "Repetitive Head Impacts in Youth Football: Description and Relationship to White Matter Structure," *Sports Health*, vol. 11, no. 6, pp. 507–513, 2019.

[144] B. M. Asken, S. T. DeKosky, J. R. Clugston, M. S. Jaffee, and R. M. Bauer, "Diffusion tensor imaging (DTI) findings in adult civilian, military, and sport-related mild traumatic brain injury (mTBI): a systematic critical review," *Brain Imaging and Behavior*, vol. 12, no. 2, pp. 585–612, 2018.

[145] A. Giorgio, K. E. Watkins, M. Chadwick, S. James, L. Winmill, G. Douaud, N. De Stefano, P. M. Matthews, S. M. Smith, H. Johansen-Berg, and A. C. James, "Longitudinal changes in grey and white matter during adolescence," *NeuroImage*, vol. 49, pp. 94–103, 2010.

[146] C. Lebel and C. Beaulieu, "Longitudinal Development of Human Brain Wiring Continues from Childhood into Adulthood," *Journal of Neuroscience*, vol. 31, no. 30, pp. 10 937–10 947, 2011.

[147] C. Lebel, S. N. Mattson, E. P. Riley, K. L. Jones, C. M. Adnams, P. A. May, S. Y. Bookheimer, M. J. O'Connor, K. L. Narr, E. Kan, Z. Abaryan, and E. R. Sowell, "A longitudinal study of the long-term consequences of drinking during pregnancy: Heavy in utero alcohol exposure disrupts the normal processes of brain development," *Journal of Neuroscience*, vol. 32, no. 44, pp. 15 243–15 251, 2012.

[148] D. J. Simmonds, M. N. Hallquist, M. Asato, and B. Luna, "Developmental stages and sex differences of white matter and behavioral development through adolescence: A longitudinal diffusion tensor imaging (DTI) study," *NeuroImage*, vol. 92, pp. 356–368, 2014.

[149] L. Babcock, W. Yuan, J. Leach, T. Nash, and S. Wade, "White matter alterations in youth with acute mild traumatic brain injury," *Journal of Pediatric Rehabilitation Medicine*, vol. 8, no. 4, pp. 285–296, 2015.

[150] J. J. Bazarian, T. Zhu, B. Blyth, A. Borrino, and J. H. Zhong, "Subject-specific changes in brain white matter on diffusion tensor imaging after sports-related concussion," *Magnetic Resonance Imaging*, vol. 30, no. 2, pp. 171–180, 2012.

[151] K. Oishi, A. Faria, H. Jiang, X. Li, K. Akhter, J. Zhang, J. T. Hsu, M. I. Miller, P. C. M. van Zijl, M. Albert, C. G. Lyketsos, R. Woods, A. W. Toga, G. B. Pike, P. Rosa-Neto, A. Evans, J. Mazziotta, and S. Mori, "Atlas-based whole brain white matter analysis using large deformation diffeomorphic metric mapping: application to normal elderly and Alzheimer's disease participants," *NeuroImage*, vol. 46, no. 2, pp. 486–499, 2009.

[152] B. Whitcher, D. S. Tuch, J. J. Wisco, A. G. Sorensen, and L. Wang, "Using the wild bootstrap to quantify uncertainty in diffusion tensor imaging," *Human Brain Mapping*, vol. 29, no. 3, pp. 346–362, 2008.

[153] M. Borich, N. Makan, L. Boyd, and N. Virji-Babul, "Combining Whole-Brain Voxel-Wise Analysis with In Vivo Tractography of Diffusion Behavior after Sports-Related Concussion in Adolescents: A Preliminary Report," *Journal of Neurotrauma*, vol. 30, no. 14, pp. 1243–1249, 2013.

[154] S. Mori, K. Oishi, H. Jiang, L. Jiang, X. Li, K. Akhter, K. Hua, A. V. Faria, A. Mahmood, R. Woods, A. W. Toga, G. B. Pike, P. R. Neto, A. Evans, J. Zhang, H. Huang, M. I. Miller, P. van Zijl, and J. Mazziotta, "Stereotaxic white matter atlas based on diffusion tensor imaging in an ICBM template," *NeuroImage*, vol. 40, no. 2, pp. 570–582, 2008.

[155] E. M. Davenport, C. T. Whitlow, J. E. Urban, M. A. Espeland, Y. Jung, D. A. Rosenbaum, G. A. Gioia, A. K. Powers, J. D. Stitzel, and J. A. Maldjian, "Abnormal White Matter Integrity Related to Head Impact Exposure in a Season of High School Varsity Football," *Journal of Neurotrauma*, vol. 31, no. 19, pp. 1617–1624, 2014.

[156] E. M. Davenport, K. Apkarian, C. T. Whitlow, J. E. Urban, J. H. Jensen, E. Szuch, M. A. Espeland, Y. Jung, D. A. Rosenbaum, G. A. Gioia, A. K. Powers, J. D. Stitzel, and J. A. Maldjian, "Abnormalities in diffusional kurtosis metrics related to head impact exposure in a season of high school varsity football," *Journal of Neurotrauma*, vol. 33, no. 23, pp. 2133–2146, 2016.

[157] K. B. Foss, W. Yuan, J. Diekfuss, J. Leach, W. Meehan, C. DiCesare, G. Solomon, D. Schneider, J. MacDonald, J. Dudley, N. Cortes, R. Galloway, M. Halstead, G. Walker, and G. Myer, "Relative Head Impact Exposure and Brain White Matter Alterations After a Single Season of Competitive Football: A Pilot Comparison of Youth Versus High School Football," *Clin J Sport Med*, vol. 29, pp. 442–450, 2019.

[158] S. J. Kuzminski, M. D. Clark, M. A. Fraser, C. C. Haswell, R. A. Morey, C. Liu, K. R. Choudhury, K. M. Guskiewicz, and J. R. Petrella, "White Matter Changes Related to Subconcussive Impact Frequency during a Single Season of High School Football," *American Journal of Neuroradiology*, vol. 39, no. 2, pp. 245–251, 2018.

[159] A. R. Mayer, J. M. Ling, Z. Yang, A. Pena, R. A. Yeo, and S. Klimaj, "Diffusion abnormalities in pediatric mild traumatic brain injury." *Journal of Neuroscience*, vol. 32, no. 50, pp. 17 961–17 969, 2012.

[160] G. D. Myer, W. Yuan, K. B. Foss, D. Smith, M. Altaye, A. Reches, J. Leach, A. W. Kiefer, J. C. Khoury, M. Weiss, S. Thomas, C. Dicesare, J. Adams, P. J. Gubanich, A. Geva, J. F. Clark, W. P. Meehan, J. P. Mihalik, and D. Krueger, "The effects of external jugular compression applied during head impact exposure on longitudinal changes in brain neuroanatomical and neurophysiological biomarkers: A preliminary investigation," *Frontiers in Neurology*, vol. 7, p. 74, 2016a.

[161] G. D. Myer, W. Yuan, K. B. Foss, S. Thomas, D. Smith, J. Leach, A. W. Kiefer, C. Dicesare, J. Adams, P. J. Gubanich, K. Kitchen, D. K. Schneider, D. Braswell, D. Krueger, and M. Altaye, "Analysis of head impact exposure and brain microstructure response in a season-long application of a jugular vein compression collar: A prospective, neuroimaging investigation in American football," *British Journal of Sports Medicine*, vol. 50, no. 20, pp. 1276–1285, 2016b.

[162] G. D. Myer, K. B. Foss, S. Thomas, R. Galloway, C. A. Dicesare, J. Dudley, B. Gadd, J. Leach, D. Smith, P. Gubanich, W. P. Meehan, M. Altaye, P. Lavin, and W. Yuan, "Altered brain microstructure in association with repetitive subconcussive head impacts and the potential protective effect of jugular vein compression: A longitudinal study of female soccer athletes," *British Journal of Sports Medicine*, vol. 53, pp. 1539–1551, 2019.

[163] E. K. Satchell, S. D. Friedman, V. Bompadre, A. Poliakov, A. Oron, and T. M. Jinguji, "Use of diffusion tension imaging in the evaluation of pediatric concussions," *Musculoskeletal Science and Practice*, vol. 42, pp. 162–165, 2019.

[164] N. Virji-Babul, M. R. Borich, N. Makan, T. Moore, K. Frew, C. A. Emery, and L. A. Boyd, "Diffusion tensor imaging of sports-related concussion in adolescents," *Pediatric Neurology*, vol. 48, no. 1, pp. 24–29, 2013.

[165] W. Yuan, K. B. Foss, S. Thomas, C. A. DiCesare, J. A. Dudley, K. Kitchen, B. Gadd, J. L. Leach, D. Smith, M. Altaye, P. Gubanich, R. T. Galloway, P. McCrory, J. E. Bailes, R. Mannix, W. P. Meehan, and G. D. Myer, "White matter alterations over the course of two consecutive high-school football seasons and the effect of a jugular compression collar: A preliminary longitudinal diffusion tensor imaging study," *Human Brain Mapping*, vol. 39, no. 1, pp. 491–508, 2018.

[166] Y. Zou, I. Jang, N. L. Vike, T. M. Talavage, and J. V. Rispoli, "Acute impacts of football competition on brain white matter microstructure in high school athletes," in *Biomedical Engineering Society 2017 Annual Meeting*, Phoenix, AZ, U.S.A., 2017.

[167] Y. Zou, T. Lee, R. J. Lycke, I. Jang, N. L. Vike, E. A. Nauman, T. M. Talavage, and J. V. Rispoli, "High-G head collisions are associated with short-term white matter microstructural deficits in high school football athletes," in *Journal of Neurotrauma*, vol. 35, Toronto, ON, Canada, 2018.

[168] Y. Zou, W. Zhu, H.-C. Yang, T. M. Talavage, and J. V. Rispoli, "Population-specific brain atlas for adolescent collision-sport athletes in Purdue Neurotrauma Group longitudinal database," 2019. [Online]. Available: https://doi.org/10.4231/XGNK-JX08

[169] R. Pordes, D. Petravick, B. Kramer, D. Olson, M. Livny, A. Roy, P. Avery, K. Blackburn, T. Wenaus, F. Würthwein, I. Foster, R. Gardner, M. Wilde, A. Blatecky, J. McGee, and R. Quick, "The open science grid," *J Phys Conf Ser*, vol. 78, p. 012057, 2007.

[170] I. Sfiligoi, D. C. Bradley, B. Holzman, P. Mhashilkar, S. Padhi, and F. Würthwein, "The pilot way to Grid resources using glideinWMS," *Proc WRI World Congr Comput Sci Inf Eng*, vol. 2, pp. 428–432, 2009.

[171] B. B. Avants, C. L. Epstein, M. Grossman, and J. C. Gee, "Symmetric diffeomorphic image registration with cross-correlation: Evaluating automated labeling of elderly and neurodegenerative brain," *Medical Image Analysis*, vol. 12, no. 1, pp. 26–41, 2008.

[172] P. Coupé, J. Manjón, M. Robles, and D. Collins, "Adaptive multiresolution non-local means filter for three-dimensional magnetic resonance image denoising," *IET Image Processing*, vol. 6, no. 5, p. 558, 2012.

[173] L. G. Nyúl, J. K. Udupa, and X. Zhang, "New variants of a method of MRI scale standardization," *IEEE Transactions on Medical Imaging*, vol. 19, no. 2, pp. 143–150, 2000.

[174] B. B. Avants, P. Yushkevich, J. Pluta, D. Minkoff, M. Korczykowski, J. Detre, and J. C. Gee, "The optimal template effect in hippocampus studies of diseased populations," *NeuroImage*, vol. 49, no. 3, p. 2457, 2010.

[175] A. Klein, J. Andersson, B. A. Ardekani, J. Ashburner, B. Avants, M. C. Chiang, G. E. Christensen, D. L. Collins, J. Gee, P. Hellier, J. H. Song, M. Jenkinson, C. Lepage, D. Rueckert, P. Thompson, T. Vercauteren, R. P. Woods, J. J. Mann, and R. V. Parsey, "Evaluation of 14 nonlinear deformation algorithms applied to human brain MRI registration," *NeuroImage*, vol. 46, no. 3, pp. 786–802, 2009.

[176] B. Fischl, "FreeSurfer," *NeuroImage*, vol. 62, no. 2, pp. 774–781, 2012.

[177] R. S. Desikan, F. Ségonne, B. Fischl, B. T. Quinn, B. C. Dickerson, D. Blacker, R. L. Buckner, A. M. Dale, R. P. Maguire, B. T. Hyman, M. S. Albert, and R. J. Killiany, "An automated labeling system for subdividing the human cerebral cortex on MRI scans into gyral based regions of interest," *NeuroImage*, vol. 31, no. 3, pp. 968–980, 2006.

[178] A. Klein and J. Tourville, "101 labeled brain images and a consistent human cortical labeling protocol," *Frontiers in Neuroscience*, vol. 6, p. 171, 2012.

[179] C. Destrieux, B. Fischl, A. Dale, and E. Halgren, "Automatic parcellation of human cortical gyri and sulci using standard anatomical nomenclature," *NeuroImage*, vol. 53, no. 1, pp. 1–15, 2010.

[180] H. Zhang, P. A. Yushkevich, D. C. Alexander, and J. C. Gee, "Deformable registration of diffusion tensor MR images with explicit orientation optimization," *Medical Image Analysis*, vol. 10, no. 5, pp. 764–785, 2006.

[181] T. E. Nichols and A. P. Holmes, "Nonparametric permutation tests for functional neuroimaging: a primer with examples," *Human Brain Mapping*, vol. 15, no. 1, pp. 1–25, 2002.

[182] S. M. Smith and T. E. Nichols, "Threshold-free cluster enhancement: addressing problems of smoothing, threshold dependence and localisation in cluster inference," *NeuroImage*, vol. 44, no. 1, pp. 83–98, 2009.

[183] S. Mori, S. Wakana, L. Nagae-Poetscher, and P. van Zijl, "MRI Atlas of Human White Matter," *American Journal of Neuroradiology*, p. 284, 2005.

[184] R Core Team, *R: A Language and Environment for Statistical Computing*, R Foundation for Statistical Computing, Vienna, Austria, 2019. [Online]. Available: https://www.r-project.org/

[185] W. Van Hecke, A. Leemans, E. D'Agostino, S. De Backer, E. Vandervliet, P. M. Parizel, and J. Sijbers, "Nonrigid coregistration of diffusion tensor images using a viscous fluid model and mutual information," *IEEE Transactions on Medical Imaging*, vol. 26, no. 11, pp. 1598–1612, 2007.

[186] G. Wu, H. Jia, Q. Wang, and D. Shen, "SharpMean: Groupwise registration guided by sharp mean image and tree-based registration," *NeuroImage*, vol. 56, no. 4, pp. 1968–1981, 2011.

[187] D. Xu, S. Mori, D. Shen, P. C. Van Zijl, and C. Davatzikos, "Spatial normalization of diffusion tensor fields," *Magn Reson Med*, vol. 50, pp. 175–182, 2003.

[188] L. Akakpo, W. C. Pierre, C. Jin, I. Londono, P. Pouliot, and G. A. Lodygensky, "User-independent diffusion tensor imaging analysis pipelines in a rat model presenting ventriculomegalia: A comparison study," *NMR in Biomedicine*, vol. 30, no. 11, 2017.

[189] H. J. Park, M. Kubicki, M. E. Shenton, A. Guimond, R. W. McCarley, S. E. Maier, R. Kikinis, F. A. Jolesz, and C. F. Westin, "Spatial normalization of diffusion tensor MRI using multiple channels," *NeuroImage*, vol. 20, no. 4, pp. 1995–2009, 2003.

[190] H. Zhang, B. B. Avants, P. A. Yushkevich, J. H. Woo, S. Wang, L. F. McCluskey, L. B. Elman, E. R. Melhem, and J. C. Gee, "High-dimensional spatial normalization of diffusion tensor images improves the detection of white matter differences: An example study using amyotrophic lateral sclerosis," *IEEE Transactions on Medical Imaging*, vol. 26, pp. 1585–1597, 2007.

[191] M. O. Irfanoglu, A. Nayak, J. Jenkins, E. B. Hutchinson, N. Sadeghi, C. P. Thomas, and C. Pierpaoli, "DR-TAMAS: Diffeomorphic Registration for Tensor Accurate Alignment of Anatomical Structures," *NeuroImage*, vol. 132, pp. 439–454, 2016.

[192] V. Douet and L. Chang, "Fornix as an imaging marker for episodic memory deficits in healthy aging and in various neurological disorders," *Frontiers in Aging Neuroscience*, vol. 6, p. 343, 2014.

[193] M. B. Carpenter and J. Sutin, *Human Neuroanatomy*, 8th ed. Baltimore: Williams & Wilkins, 1983.

[194] A. C. McKee, B. Abdolmohammadi, and T. D. Stein, "The neuropathology of chronic traumatic encephalopathy," *Handbook of Clinical Neurology*, vol. 158, pp. 297–307, 2018.

[195] R. A. Stern, D. O. Riley, D. H. Daneshvar, C. J. Nowinski, R. C. Cantu, and A. C. McKee, "Long-term Consequences of Repetitive Brain Trauma: Chronic Traumatic Encephalopathy," *PM&R*, vol. 3, no. 10, pp. S460–S467, 2011.

[196] M. A. Warner, C. M. De La Plata, J. Spence, J. Y. Wang, C. Harper, C. Moore, M. Devous, and R. Diaz-Arrastia, "Assessing spatial relationships between axonal integrity, regional brain volumes, and neuropsychological outcomes after traumatic axonal injury," *Journal of Neurotrauma*, vol. 27, no. 12, pp. 2121–2130, 2010.

[197] D. F. Tate and E. D. Bigler, "Fornix and hippocampal atrophy in traumatic brain injury," *Learning and Memory*, vol. 7, no. 6, pp. 442–446, 2000.

[198] M. E. Shenton, H. M. Hamoda, J. S. Schneiderman, S. Bouix, O. Pasternak, Y. Rathi, M. A. Vu, M. P. Purohit, K. Helmer, I. Koerte, A. P. Lin, C. F. Westin, R. Kikinis, M. Kubicki, R. A. Stern, and R. Zafonte, "A review of magnetic resonance imaging and diffusion tensor imaging findings in mild traumatic brain injury," *Brain Imaging and Behavior*, vol. 6, no. 2, pp. 137–192, 2012.

[199] Y. Jin, Y. Shi, L. Zhan, and P. M. Thompson, "Automated Multi-Atlas Labeling of the Fornix and Its Integrity In Alzheimer's Disease," in *Proceedings. IEEE International Symposium on Biomedical Imaging*, vol. 2015. Alzheimer's Disease Neuroimaging Initiative (ADNI), 2015, pp. 140–143.

[200] K. J. Jung, "Removal of partial volume averaging with free water in MR diffusion tensor imaging using inversion recovery for b0 image," *Magn Reson Imaging*, vol. 32, no. 6, pp. 619–624, 2014.

[201] S. Treit, T. Steve, D. W. Gross, and C. Beaulieu, "High resolution in-vivo diffusion imaging of the human hippocampus." *NeuroImage*, vol. 182, pp. 479–487, 2018.

[202] S. B. Vos, D. K. Jones, M. A. Viergever, and A. Leemans, "Partial volume effect as a hidden covariate in DTI analyses," *NeuroImage*, vol. 55, no. 4, pp. 1566–1576, 2011.

[203] M. Picciotto, "Analytical transparency and reproducibility in human neuroimaging studies," *Journal of Neuroscience*, vol. 38, no. 14, pp. 3375–3376, 2018.

[204] R. A. Poldrack, C. I. Baker, J. Durnez, K. J. Gorgolewski, P. M. Matthews, M. R. Munafò, T. E. Nichols, J. B. Poline, E. Vul, and T. Yarkoni, "Scanning the horizon: Towards transparent and reproducible neuroimaging research," *Nature Reviews Neuroscience*, vol. 18, no. 2, pp. 115–126, 2017.

[205] W. Van Hecke, A. Leemans, S. De Backer, B. Jeurissen, P. M. Parizel, and J. Sijbers, "Comparing isotropic and anisotropic smoothing for voxel-based DTI analyses: A simulation study," *Human Brain Mapping*, vol. 31, no. 1, pp. 98–114, 2010.

[206] M. Cercignani, M. Bozzali, G. Iannucci, G. Comi, and M. Filippi, "Intra-voxel and inter-voxel coherence in patients with multiple sclerosis assessed using diffusion tensor MRI," *Journal of Neurology*, vol. 249, no. 7, pp. 875–883, 2002.

[207] E. Sbardella, F. Tona, N. Petsas, and P. Pantano, "DTI Measurements in Multiple Sclerosis: Evaluation of Brain Damage and Clinical Implications," *Multiple Sclerosis International*, p. 671730, 2013.

[208] E. McCuen, D. Svaldi, K. Breedlove, N. Kraz, B. Cummiskey, E. L. Breedlove, J. Traver, K. F. Desmond, R. E. Hannemann, E. Zanath, A. Guerra, L. Leverenz, T. M. Talavage, and E. A. Nauman, "Collegiate women's soccer players suffer greater cumulative head impacts than their high school counterparts," *Journal of Biomechanics*, vol. 48, no. 13, pp. 3720–3723, 2015.

[209] S. P. Broglio, J. T. Eckner, and J. S. Kutcher, "Field-based measures of head impacts in high school football athletes," *Current Opinion in Pediatrics*, vol. 24, no. 6, pp. 702–708, 2012.

[210] S. P. Broglio and K. M. Guskiewicz, "Concussion in sports: The sideline assessment," *Sports Health*, vol. 1, no. 5, pp. 361–369, 2009.

[211] M. Luciana, H. M. Conklin, C. J. Hooper, and R. S. Yarger, "The development of nonverbal working memory and executive control processes in adolescents," *Child Dev*, vol. 76, no. 3, pp. 697–712, 2005.

[212] B. Luna, K. E. Garver, T. A. Urban, N. A. Lazar, and J. A. Sweeney, "Maturation of cognitive processes from late childhood to adulthood," *Child Dev*, vol. 75, no. 5, pp. 1357–1372, 2004.

[213] C. D. Ladouceur, J. S. Peper, E. A. Crone, and R. E. Dahl, "White matter development in adolescence: The influence of puberty and implications for affective disorders," *Developmental Cognitive Neuroscience*, vol. 2, no. 1, pp. 36–54, 2012.

[214] R. K. Lenroot, N. Gogtay, D. K. Greenstein, E. M. Wells, G. L. Wallace, L. S. Clasen, J. D. Blumenthal, J. Lerch, A. P. Zijdenbos, A. C. Evans, P. M. Thompson, and J. N. Giedd, "Sexual dimorphism of brain developmental trajectories during childhood and adolescence," *Neuroimage*, vol. 36, no. 4, pp. 1065–1073, 2007.

[215] M. R. Asato, R. Terwilliger, J. Woo, and B. Luna, "White matter development in adolescence: a DTI study," *Cereb Cortex*, vol. 20, no. 9, pp. 2122–2131, 2010.

[216] M. Ashtari, K. L. Cervellione, K. M. Hasan, J. Wu, C. McIlree, H. Kester, B. A. Ardekani, D. Roofeh, P. R. Szeszko, and S. Kumra, "White matter development during late adolescence in healthy males: a cross-sectional diffusion tensor imaging study," *NeuroImage*, vol. 35, no. 2, pp. 501–510, 2007.

[217] N. Barnea-Goraly, V. Menon, M. Eckert, L. Tamm, R. Bammer, A. Karchemskiy, C. C. Dant, and A. L. Reiss, "White matter development during childhood and adolescence: a cross-sectional diffusion tensor imaging study," *Cereb Cortex*, vol. 15, no. 12, pp. 1848–1854, 2005.

[218] S. K. Krogsrud, A. Fjell, C. K. Tamnes, H. Grydeland, L. Mork, P. Due-Tonnessen, A. Bjornerud, C. Sampaio-Baptista, J. Andersson, H. Johansen-Berg, and K. B. Walhovd, "Changes in white matter microstructure in the developing brain-A longitudinal diffusion tensor imaging study of children from 4 to 11 years of age," *NeuroImage*, vol. 124, pp. 473–486, 2016.

[219] T. Paus, "Growth of white matter in the adolescent brain: myelin or axon?" *Brain Cogn*, vol. 72, no. 1, pp. 26–35, 2010.

[220] V. J. Schmithorst and W. H. Yuan, "White matter development during adolescence as shown by diffusion MRI," *Brain Cogn*, vol. 72, no. 1, pp. 16–25, 2010.

[221] I. K. Koerte, J. Hufschmidt, M. Muehlmann, A. P. Lin, and M. E. Shenton, *Frontiers in Neuroscience Advanced Neuroimaging of Mild Traumatic Brain Injury*. Boca Raton, FL: CRC Press/Taylor and Francis Group (c) 2016 by Taylor & Francis Group, LLC., 2016. [Online]. Available: https://www-ncbi-nlm-nih-gov.ucsf.idm.oclc.org/books/NBK326714/

[222] T. W. McAllister, J. C. Ford, L. A. Flashman, A. Maerlender, R. M. Greenwald, J. G. Beckwith, R. P. Bolander, T. D. Tosteson, J. H. Turco, R. Raman, and S. Jain, "Effect of head impacts on diffusivity measures in a cohort of collegiate contact sport athletes," *Neurology*, vol. 82, no. 1, pp. 63–69, 2014.

[223] A. Gardner, F. Kay-Lambkin, P. Stanwell, J. Donnelly, W. H. Williams, A. Hiles, P. Schofield, C. Levi, and D. K. Jones, "A Systematic Review of Diffusion Tensor Imaging Findings in Sports-Related Concussion," *Journal of Neurotrauma*, vol. 29, no. 16, pp. 2521–2538, 2012.

[224] P. J. Basser, J. Mattiello, and D. LeBihan, "MR diffusion tensor spectroscopy and imaging," *Biophys J*, vol. 66, no. 1, pp. 259–267, 1994.

[225] S. Mori and J. Zhang, "Principles of diffusion tensor imaging and its applications to basic neuroscience research," *Neuron*, vol. 51, no. 5, pp. 527–539, 2006.

[226] B. Jeurissen, A. Leemans, J. D. Tournier, D. K. Jones, and J. Sijbers, "Investigating the prevalence of complex fiber configurations in white matter tissue with diffusion magnetic resonance imaging," *Human Brain Mapping*, vol. 34, no. 11, pp. 2747–2766, 2013.

[227] N. R. Galloway, K. A. Tong, S. Ashwal, U. Oyoyo, and A. Obenaus, "Diffusion-weighted imaging improves outcome prediction in pediatric traumatic brain injury," *J Neurotrauma*, vol. 25, no. 10, pp. 1153–1162, 2008.

[228] E. A. Wilde, Z. Chu, E. D. Bigler, J. V. Hunter, M. A. Fearing, G. Hanten, M. R. Newsome, R. S. Scheibel, X. Li, and H. S. Levin, "Diffusion tensor imaging in the corpus callosum in children after moderate to severe traumatic brain injury," *J Neurotrauma*, vol. 23, no. 10, pp. 1412–1426, 2006.

[229] J. R. Wozniak and K. O. Lim, "Advances in white matter imaging: a review of in vivo magnetic resonance methodologies and their applicability to the study of development and aging," *Neurosci Biobehav Rev*, vol. 30, no. 6, pp. 762–774, 2006.

[230] S. K. Song, S. W. Sun, W. K. Ju, S. J. Lin, A. H. Cross, and A. H. Neufeld, "Diffusion tensor imaging detects and differentiates axon and myelin degeneration in mouse optic nerve after retinal ischemia," *NeuroImage*, vol. 20, pp. 1714–1722, 2003.

[231] P. J. Winklewski, A. Sabisz, P. Naumczyk, K. Jodzio, E. Szurowska, and A. Szarmach, "Understanding the physiopathology behind axial and radial diffusivity changes-what do we Know?" *Frontiers in Neurology*, vol. 9, p. 92, 2018.

[232] C. L. Mac Donald, K. Dikranian, P. Bayly, D. Holtzman, and D. Brody, "Diffusion tensor imaging reliably detects experimental traumatic axonal injury and indicates approximate time of injury," *Journal of Neuroscience*, vol. 27, pp. 11 869–11 876, 2007.

[233] C. D. Chong and T. J. Schwedt, "White Matter Damage and Brain Network Alterations in Concussed Patients: A Review of Recent Diffusion Tensor Imaging and Resting-State Functional Connectivity Data," *Current Pain and Headache Reports*, vol. 19, no. 5, p. 485, 2015.

[234] M. L. Lipton, E. Gellella, C. Lo, T. Gold, B. A. Ardekani, K. Shifteh, J. A. Bello, and C. A. Branch, "Multifocal White Matter Ultrastructural Abnormalities in Mild Traumatic Brain Injury with Cognitive Disability: A Voxel-Wise Analysis of Diffusion Tensor Imaging," *Journal of Neurotrauma*, vol. 25, no. 11, pp. 1335–1342, 2008.

[235] G. T. Voelbel, H. M. Genova, N. D. Chiaravalotti, and M. J. Hoptman, "Diffusion tensor imaging of traumatic brain injury review: Implications for neurorehabilitation," *Neurorehabilitation*, vol. 31, no. 3, pp. 281–293, 2012.

[236] K. L. Xiong, Y. S. Zhu, and W. G. Zhang, "Diffusion tensor imaging and magnetic resonance spectroscopy in traumatic brain injury: a review of recent literature," *Brain Imaging and Behavior*, vol. 8, no. 4, pp. 487–496, 2014.

[237] E. M. Davenport, J. E. Urban, F. Mokhtari, E. L. Lowther, J. D. Van Horn, C. G. Vaughan, G. A. Gioia, C. T. Whitlow, J. D. Stitzel, and J. A. Maldjian, "Subconcussive impacts and imaging findings over a season of contact sports," *Concussion*, vol. 1, no. 4, p. CNC19, 2016.

[238] L. Mainwaring, K. M. Ferdinand Pennock, S. Mylabathula, and B. Z. Alavie, "Subconcussive head impacts in sport: A systematic review of the evidence," *International Journal of Psychophysiology*, vol. 132, pp. 39–54, 2018.

[239] M. A. Lancaster, D. V. Olson, M. A. McCrea, L. D. Nelson, A. A. LaRoche, and L. T. Muftuler, "Acute white matter changes following sport-related concussion: A serial diffusion tensor and diffusion kurtosis tensor imaging study," *Human Brain Mapping*, vol. 37, no. 11, pp. 3821–3834, 2016.

[240] M. A. Lancaster, T. B. Meier, D. V. Olson, M. A. McCrea, L. D. Nelson, and L. T. Muftuler, "Chronic differences in white matter integrity following sport-related concussion as measured by diffusion MRI: 6-Month follow-up," *Human Brain Mapping*, vol. 39, no. 11, pp. 4276–4289, 2018.

[241] D. O. Svaldi, C. Joshi, E. C. McCuen, J. P. Music, R. Hannemann, L. J. Leverenz, E. A. Nauman, and T. M. Talavage, "Accumulation of high magnitude acceleration events predicts cerebrovascular reactivity changes in female high school soccer athletes," *Brain Imaging and Behavior*, vol. 14, pp. 164–174, 2020.

[242] D. K. Schneider, R. Galloway, J. J. Bazarian, J. A. Diekfuss, J. Dudley, J. L. Leach, R. Mannix, T. M. Talavage, W. Yuan, and G. D. Myer, "Diffusion tensor imaging in athletes sustaining repetitive head impacts: A systematic review of prospective studies," *Journal of Neurotrauma*, vol. 36, no. 20, pp. 2831–2849, 2019.

[243] T. A. Lee, R. J. Lycke, P. J. Lee, C. M. Cudal, K. J. Torolski, S. E. Bucherl, N. Leiva-Molano, P. S. Auerbach, T. M. Talavage, and E. A. Nauman, "Distribution of Head Acceleration Events Varies by Position and Play Type in North American Football," *Clin J Sport Med*, vol. [Epub ahea, 2020.

[244] N. Leiva-Molano, R. Rolley, T. Lee, K. McIver, G. Sankaran, J. Meyer, D. E. Adams, E. L. Breedlove, T. Talavage, and E. A. Nauman, "Evaluation of Impulse Attenuation by Football Helmets in the Frequency Domain." *J Biomech Eng*, 2020.

[245] K. G. McIver, G. N. Sankaran, P. Lee, S. Bucherl, N. Leiva, T. M. Talavage, L. Leverenz, and E. A. Nauman, "Impact attenuation of male and female lacrosse helmets using a modal impulse hammer," *Journal of Biomechanics*, vol. 95, p. 109313, 2019.

[246] B. Cummiskey, G. N. Sankaran, K. G. McIver, D. Shyu, J. Markel, T. M. Talavage, L. Leverenz, J. J. Meyer, D. Adams, and E. A. Nauman, "Quantitative evaluation of impact attenuation by football helmets using a modal impulse hammer," *Proceedings of the Institution of Mechanical Engineers, Part P: Journal of Sports Engineering and Technology*, vol. 233, no. 2, pp. 301–311, 2019.

[247] K. M. Breedlove, E. Breedlove, E. Nauman, T. G. Bowman, and M. R. Lininger, "The ability of an aftermarket helmet add-on device to reduce impact-force accelerations during drop tests," *Journal of Athletic Training*, vol. 52, pp. 802–808, 2017.

[248] Y. Zou, W. Zhu, H.-C. Yang, Y. Zhu, Y. Tong, T. M. Talavage, and J. V. Rispoli, "Develop Population-specific Brain Atlas with High-throughput High-performance Computingle," in *Proceedings of the 25th Annual Meeting of the Organization for Human Brain Mapping*, Rome, Italy, 2019.

[249] T. S. Redick, E. A. Wiemers, and R. W. Engle, "The role of proactive interference in working memory training and transfer," *Psychological Research*, 2019.

[250] R. Engle and M. Kane, "Executive attention, working memory capacity, and a two-factor theory of cognitive control," *The Psychology of Learning and Motivation*, vol. 44, pp. 145–199, 2004.

[251] T. S. Redick, Z. Shipstead, M. E. Meier, J. J. Montroy, K. L. Hicks, N. Unsworth, M. J. Kane, D. Z. Hambrick, and R. W. Engle, "Cognitive predictors of a common multitasking ability: Contributions from working memory, attention control, and fluid intelligence," *J Exp Psychol Gen*, vol. 145, pp. 1473–1492, 2016.

[252] B. Webb, D. Humphreys, and M. Heath, "Oculomotor Executive Dysfunction during the Early and Later Stages of Sport-Related Concussion Recovery," *Journal of Neurotrauma*, vol. 35, no. 16, pp. 1874–1881, 2018.

[253] E. A. Wiemers and T. S. Redick, "Task manipulation effects on the relationship between working memory and go/no-go task performance," *Consciousness and Cognition*, vol. 71, pp. 39–58, 2019.

[254] W. Chang, J. Cheng, J. Allaire, Y. Xie, and J. McPherson, "Shiny: Web Application Framework for R," 2019. [Online]. Available: https://cran.r-project.org/package= shiny

[255] D. K. Jones, T. R. Knosche, and R. Turner, "White matter integrity, fiber count, and other fallacies: the do's and don'ts of diffusion MRI," *Neuroimage*, vol. 73, pp. 239–254, 2013.

[256] R. Kumar, R. K. Gupta, M. Husain, C. Chaudhry, A. Srivastava, S. Saksena, and R. K. Rathore, "Comparative evaluation of corpus callosum DTI metrics in acute mild and moderate traumatic brain injury: Its correlation with neuropsychometric test," *Brain Injury*, vol. 23, pp. 675–685, 2009.

[257] N. Bahrami, D. Sharma, S. Rosenthal, E. M. Davenport, J. E. Urban, B. Wagner, Y. Jung, C. G. Vaughan, G. A. Gioia, J. D. Stitzel, C. T. Whitlow, and J. A. Maldjian, "Subconcussive Head Impact Exposure and White Matter Tract Changes over a Single Season of Youth Football," *Radiology*, vol. 281, no. 3, pp. 919–926, 2016.

[258] N. Z. Gungor and D. Paré, "Functional Heterogeneity in the Bed Nucleus of the Stria Terminalis." *The Journal of neuroscience : the official journal of the Society for Neuroscience*, vol. 36, no. 31, pp. 8038–49, 2016. [Online]. Available: http://www.ncbi.nlm.nih.gov/pubmed/27488624

[259] J. M. Williams and M. B. Andersen, "Psychosocial antecedents of sport injury: Review and critique of the stress and injury model'," *Journal of Applied Sport Psychology*, vol. 10, no. 1, pp. 5–25, 1998.

[260] C. Eierud, R. C. Craddock, S. Fletcher, M. Aulakh, B. King-Casas, D. Kuehl, and S. M. Laconte, "Neuroimaging after mild traumatic brain injury: Review and meta-analysis," *NeuroImage: Clinical*, vol. 4, pp. 283–294, 2014.

[261] S. N. Niogi and P. Mukherjee, "Diffusion tensor imaging of mild traumatic brain injury," *J Head Trauma Rehabil*, vol. 25, pp. 241–255, 2010.

[262] W. P. Medendorp, H. C. Goltz, and T. Vilis, "Remapping the remembered target location for anti-saccades in human posterior parietal cortex." *Journal of neurophysiology*, vol. 94, no. 1, pp. 734–740, 2005.

[263] D. P. Munoz and S. Everling, "Look away: the anti-saccade task and the voluntary control of eye movement." *Nature reviews. Neuroscience*, vol. 5, no. 3, pp. 218–228, 2004.

[264] I. H. Choo, D. Y. Lee, J. S. Oh, J. S. Lee, D. S. Lee, I. C. Song, J. C. Youn, S. G. Kim, K. W. Kim, J. H. Jhoo, and J. I. Woo, "Posterior cingulate cortex atrophy and regional cingulum disruption in mild cognitive impairment and Alzheimer's disease." *Neurobiology of aging*, vol. 31, no. 5, pp. 772–779, 2010.

[265] R. J. Echemendia, J. M. Bruce, W. Meeuwisse, P. Comper, M. Aubry, and M. Hutchison, "Long-term reliability of ImPACT in professional ice hockey," *Clinical Neuropsychologist*, vol. 30, no. 2, pp. 328–337, 2016.

[266] L. B. Mayers and T. S. Redick, "Clinical utility of ImPACT assessment for post-concussion return-to-play counseling: Psychometric issues," *Journal of Clinical and Experimental Neuropsychology*, 2012.

[267] S. Chung, E. Fieremans, X. Wang, N. E. Kucukboyaci, C. J. Morton, J. Babb, P. Amorapanth, F.-Y. A. Foo, D. S. Novikov, S. R. Flanagan, J. F. Rath, and Y. W. Lui, "White Matter Tract Integrity: An Indicator of Axonal Pathology after Mild Traumatic Brain Injury," *Journal of Neurotrauma*, vol. 35, no. 8, pp. 1015–1020, 2017.

[268] N. J. Gong, S. Kuzminski, M. Clark, M. Fraser, M. Sundman, K. Guskiewicz, J. R. Petrella, and C. Liu, "Microstructural alterations of cortical and deep gray matter over a season of high school football revealed by diffusion kurtosis imaging," *Neurobiology of Disease*, vol. 119, pp. 79–87, 2018.

[269] B. Fischl, D. H. Salat, E. Busa, M. Albert, M. Dieterich, C. Haselgrove, A. Van Der Kouwe, R. Killiany, D. Kennedy, S. Klaveness, A. Montillo, N. Makris, B. Rosen, and A. M. Dale, "Whole brain segmentation: Automated labeling of neuroanatomical structures in the human brain," *Neuron*, vol. 33, no. 3, pp. 341–355, 2002.

[270] M. Baxi, M. A. Di Biase, A. E. Lyall, S. Cetin-Karayumak, J. Seitz, L. Ning, N. Makris, D. Rosene, M. Kubicki, and Y. Rathi, "Quantifying Genetic and Environmental Influence on Gray Matter Microstructure Using Diffusion MRI," *Cerebral Cortex*, 2020.

[271] S. K. Zhou, *Medical Image Recognition, Segmentation and Parsing: Machine Learning and Multiple Object Approaches.* Elsevier Inc., 2016.

[272] A. Fenster and B. Chiu, "Evaluation of segmentation algorithms for medical imaging," *Annual International Conference of the IEEE Engineering in Medicine and Biology - Proceedings*, vol. 7, pp. 7186–7189, 2005.

[273] A. J. Steven, J. Zhuo, and E. R. Melhem, "Diffusion Kurtosis Imaging: An Emerging Technique for Evaluating the Microstructural Environment of the Brain," *American Journal of Roentgenology*, vol. 202, no. 1, pp. W26–W33, 2013.

[274] J. H. Jensen, J. A. Helpern, A. Ramani, H. Lu, and K. Kaczynski, "Diffusional kurtosis imaging: The quantification of non-Gaussian water diffusion by means of magnetic resonance imaging," *Magn Reson Med*, vol. 53, no. 6, pp. 1432–1440, 2005.

[275] E. S. Hui, M. M. Cheung, L. Qi, and E. X. Wu, "Towards better MR characterization of neural tissues using directional diffusion kurtosis analysis," *NeuroImage*, vol. 42, pp. 122–134, 2008.

[276] D. Kilinc, G. Gallo, and K. A. Barbee, "Mechanical membrane injury induces axonal beading through localized activation of calpain," *Experimental Neurology*, vol. 219, no. 2, pp. 553–561, 2009.

[277] J. L. R. Andersson and S. N. Sotiropoulos, "An integrated approach to correction for off-resonance effects and subject movement in diffusion MR imaging," *NeuroImage*, vol. 125, pp. 1063–1078, 2016a.

[278] J. L. R. Andersson, M. S. Graham, E. Zsoldos, and S. N. Sotiropoulos, "Incorporating outlier detection and replacement into a non-parametric framework for movement and distortion correction of diffusion MR images." *NeuroImage*, vol. 141, pp. 556–572, 2016b.

[279] A. Tabesh, J. H. Jensen, B. A. Ardekani, and J. A. Helpern, "Estimation of tensors and tensor-derived measures in diffusional kurtosis imaging," *Magn Reson Med*, vol. 65, no. 3, pp. 823–836, 2011.

[280] I. Jang, S. Bari, Y. Zou, N. L. Vike, P. Kashyap, and T. M. Talavage, "Test-Retest and Between-Site Reliability in a Multisite Diffusion Tensor Imaging Study," in *Proceedings of the Annual Meeting of ISMRM*, Paris, 2018.

[281] M. S. Pinto, R. Paolella, T. Billiet, P. Van Dyck, P.-J. Guns, B. Jeurissen, A. Ribbens, A. J. den Dekker, and J. Sijbers, "Harmonization of Brain Diffusion MRI: Concepts and Methods," *Frontiers in Neuroscience*, vol. 14, p. 396, 2020.

[282] W. E. Johnson, C. Li, and A. Rabinovic, "Adjusting batch effects in microarray expression data using empirical Bayes methods," *Biostatistics*, vol. 8, no. 1, pp. 118–127, 2007.

[283] J. P. Fortin, N. Cullen, Y. I. Sheline, W. D. Taylor, I. Aselcioglu, P. A. Cook, P. Adams, C. Cooper, M. Fava, P. J. McGrath, M. McInnis, M. L. Phillips, M. H. Trivedi, M. M. Weissman, and R. T. Shinohara, "Harmonization of cortical thickness measurements across scanners and sites," *NeuroImage*, vol. 167, pp. 104–120, 2018.

[284] D. M. Nielson, F. Pereira, C. Y. Zheng, N. Migineishvili, J. A. Lee, A. G. Thomas, and P. A. Bandettini, "Detecting and harmonizing scanner differences in the ABCD study - annual release 1.0," *bioRxiv*, p. 309260, 2018. [Online]. Available: http://biorxiv.org/content/early/2018/05/02/309260.abstract

[285] R. Pomponio, G. Erus, M. Habes, J. Doshi, D. Srinivasan, E. Mamourian, V. Bashyam, I. M. Nasrallah, T. D. Satterthwaite, Y. Fan, L. J. Launer, C. L. Masters, P. Maruff, C. Zhuo, H. Völzke, S. C. Johnson, J. Fripp, N. Koutsouleris, D. H. Wolf, R. Gur, R. Gur, J. Morris, M. S. Albert, H. J. Grabe, S. M. Resnick, R. N. Bryan, D. A. Wolk, R. T. Shinohara, H. Shou, and C. Davatzikos, "Harmonization of large MRI datasets for the analysis of brain imaging patterns throughout the lifespan," *NeuroImage*, vol. 208, p. 116450, 2020. [Online]. Available: http://www.sciencedirect.com/science/article/pii/S1053811919310419

[286] A. A. Chen, J. C. Beer, N. J. Tustison, P. A. Cook, R. T. Shinohara, and H. Shou, "Removal of Scanner Effects in Covariance Improves Multivariate Pattern Analysis in Neuroimaging Data," *bioRxiv*, p. 858415, 2020. [Online]. Available: http://biorxiv.org/content/early/2020/02/04/858415.abstract

[287] S. Koppers, L. Bloy, J. I. Berman, C. M. Tax, J. C. Edgar, and D. Merhof, "Spherical Harmonic Residual Network for Diffusion Signal Harmonization," in *Mathematics and Visualization*, no. 226249, 2019, pp. 173–182.

A. USER MANUAL FOR PURDUE NEUROTRAUMA GROUP BRAIN ATLASES

Purdue Neurotrauma Group Adolescent Collision-Sport Athletes Brain Atlas

User Manual
v.3.1

(Updated: 30 July 2020)

Acknowledgments

Table of Contents

1. **Overview**
   a. Summary
   b. List of files
   c. How to display the image files
2. **Labels for the PNG Desikan-Killiany Grey Matter Atlas (PNG215_aparc_aseg.nii.gz)**
3. **Labels for the PNG White Matter Atlas (PNG215_wmparc.nii.gz)**

Overview

Summary

We developed a population-specific brain atlas target adolescent collision-sport (American football, soccer) athletes, based on the MRI scans from the longitudinal database of Purdue Neurotrauma Group. The brain atlas was developed in an effort to facilitate multimodal neuroimaging studies, specifically to minimize bias introduced in spatial normalization, improve sensitivity of voxel-wise statistical analysis, and therefore better clarify the mechanisms that lead to traumatic brain injury in adolescent athletes, which is one of our long-term commitments to this vulnerable population. Image processing software including FSL, ANTs, and Freesurfer were used to create the templates (T1-weighted and DTI) and semantic labels (cortical and white matter parcellations). To scale and speed up the atlas creation, we established a high-throughput high-performance computing workflow which integrated Open Science Grid and Purdue Community Clusters.

List of files

PNG215_t1w_brain.nii.gz	A T1-weighted template, based on the images from 215 early-to-middle adolescent collision-sport athletes. The template has the dimension of 256×256×256 and is not in ICBM-152 space.
PNG215_t1w_brain_mask.nii.gz	A binary mask based on the T1-weighted template.
PNG64_fa_ANTs.nii.gz	A DTI template, based on the FA maps of 64 early-to-middle adolescent football athletes in a single competition season. The template has the dimension of 256×256×256 and is in the same space as the T1-weighted template.
PNG215_aparc_aseg.nii.gz	T1-based semantic labels of cortical parcellations, according to the Desikan-Killiany labelling protocol. The labels are in the same space as the T1-weighted template, with the dimension of 256×256×256.
PNG215_wmparc.nii.gz	T1-based semantic labels of white matter parcellations. The labels are in the same space as the T1-weighted template, with the dimension of 256×256×256.
PNG215_freesurfer_labels.txt	Labels for the cortical and white matter parcellations, in plain text format.

How to display the image files

First of all, it is assumed that you have some working knowledge of Linux command line, which would be generally helpful for operating the image files. The image files (templates and labels) are in NIfTI format (https://nifti.nimh.nih.gov/). The following tools are recommended to display NIfTI files:

- FSLeyes: FSL image viewer (version 5.0.10 onwards)
  https://fsl.fmrib.ox.ac.uk/fsl/fslwiki/FSLeyes
- mrview: MRtrix image viewer
  https://mrtrix.readthedocs.io/en/latest/reference/commands/mrview.html
- MRIcron: a cross-platform NIfTI format image viewer
  https://www.nitrc.org/projects/mricron

Alternatively, the NIfTI files can be converted to MGH/MGZ format (https://surfer.nmr.mgh.harvard.edu/fswiki/FsTutorial/MghFormat) and be viewed using freeview, the FreeSurfer image viewer:
https://surfer.nmr.mgh.harvard.edu/fswiki/FreeviewGuide/FreeviewGeneralUsage/FreeviewQuickStart

Labels for the PNG215_aparc_aseg.nii.gz

order	label	StructName
0	0	background
1	2	Left-Cerebral-White-Matter
2	3	Left-Cerebral-Cortex
3	4	Left-Lateral-Ventricle
4	5	Left-Inf-Lat-Vent
5	7	Left-Cerebellum-White-Matter
6	8	Left-Cerebellum-Cortex
7	10	Left-Thalamus-Proper
8	11	Left-Caudate
9	12	Left-Putamen
10	13	Left-Pallidum
11	14	3rd-Ventricle
12	15	4th-Ventricle
13	16	Brain-Stem
14	17	Left-Hippocampus
15	18	Left-Amygdala
16	24	CSF
17	26	Left-Accumbens-area
18	28	Left-VentralDC
19	30	Left-vessel
20	31	Left-choroid-plexus
21	41	Right-Cerebral-White-Matter
22	43	Right-Lateral-Ventricle
23	44	Right-Inf-Lat-Vent
24	46	Right-Cerebellum-White-Matter
25	47	Right-Cerebellum-Cortex
26	49	Right-Thalamus-Proper
27	50	Right-Caudate
28	51	Right-Putamen
29	52	Right-Pallidum
30	53	Right-Hippocampus
31	54	Right-Amygdala
32	58	Right-Accumbens-area
33	60	Right-VentralDC
34	62	Right-vessel
35	63	Right-choroid-plexus
36	77	WM-hypointensities
37	85	Optic-Chiasm
38	251	CC_Posterior
39	252	CC_Mid_Posterior
40	253	CC_Central

order	label	StructName
41	254	CC_Mid_Anterior
42	255	CC_Anterior
43	1000	ctx-lh-unknown
44	1001	ctx-lh-bankssts
45	1002	ctx-lh-caudalanteriorcingulate
46	1003	ctx-lh-caudalmiddlefrontal
47	1005	ctx-lh-cuneus
48	1006	ctx-lh-entorhinal
49	1007	ctx-lh-fusiform
50	1008	ctx-lh-inferiorparietal
51	1009	ctx-lh-inferiortemporal
52	1010	ctx-lh-isthmuscingulate
53	1011	ctx-lh-lateraloccipital
54	1012	ctx-lh-lateralorbitofrontal
55	1013	ctx-lh-lingual
56	1014	ctx-lh-medialorbitofrontal
57	1015	ctx-lh-middletemporal
58	1016	ctx-lh-parahippocampal
59	1017	ctx-lh-paracentral
60	1018	ctx-lh-parsopercularis
61	1019	ctx-lh-parsorbitalis
62	1020	ctx-lh-parstriangularis
63	1021	ctx-lh-pericalcarine
64	1022	ctx-lh-postcentral
65	1023	ctx-lh-posteriorcingulate
66	1024	ctx-lh-precentral
67	1025	ctx-lh-precuneus
68	1026	ctx-lh-rostralanteriorcingulate
69	1027	ctx-lh-rostralmiddlefrontal
70	1028	ctx-lh-superiorfrontal
71	1029	ctx-lh-superiorparietal
72	1030	ctx-lh-superiortemporal
73	1031	ctx-lh-supramarginal
74	1032	ctx-lh-frontalpole
75	1033	ctx-lh-temporalpole
76	1034	ctx-lh-transversetemporal
77	1035	ctx-lh-insula
78	2000	ctx-rh-unknown
79	2001	ctx-rh-bankssts
80	2002	ctx-rh-caudalanteriorcingulate
81	2003	ctx-rh-caudalmiddlefrontal
82	2005	ctx-rh-cuneus
83	2006	ctx-rh-entorhinal

order	label	StructName
84	2007	ctx-rh-fusiform
85	2008	ctx-rh-inferiorparietal
86	2009	ctx-rh-inferiortemporal
87	2010	ctx-rh-isthmuscingulate
88	2011	ctx-rh-lateraloccipital
89	2012	ctx-rh-lateralorbitofrontal
90	2013	ctx-rh-lingual
91	2014	ctx-rh-medialorbitofrontal
92	2015	ctx-rh-middletemporal
93	2016	ctx-rh-parahippocampal
94	2017	ctx-rh-paracentral
95	2018	ctx-rh-parsopercularis
96	2019	ctx-rh-parsorbitalis
97	2020	ctx-rh-parstriangularis
98	2021	ctx-rh-pericalcarine
99	2022	ctx-rh-postcentral
100	2023	ctx-rh-posteriorcingulate
101	2024	ctx-rh-precentral
102	2025	ctx-rh-precuneus
103	2026	ctx-rh-rostralanteriorcingulate
104	2027	ctx-rh-rostralmiddlefrontal
105	2028	ctx-rh-superiorfrontal
106	2029	ctx-rh-superiorparietal
107	2030	ctx-rh-superiortemporal
108	2031	ctx-rh-supramarginal
109	2032	ctx-rh-frontalpole
110	2033	ctx-rh-temporalpole
111	2034	ctx-rh-transversetemporal
112	2035	ctx-rh-insula

Labels for the PNG White Matter Atlas (PNG215_wmparc.nii.gz)

order	label	StructName
0	0	background
1	2	Left-Cerebral-White-Matter
2	4	Left-Lateral-Ventricle
3	5	Left-Inf-Lat-Vent
4	7	Left-Cerebellum-White-Matter
5	8	Left-Cerebellum-Cortex
6	10	Left-Thalamus-Proper
7	11	Left-Caudate
8	12	Left-Putamen
9	13	Left-Pallidum
10	14	3rd-Ventricle
11	15	4th-Ventricle
12	16	Brain-Stem
13	17	Left-Hippocampus
14	18	Left-Amygdala
15	24	CSF
16	26	Left-Accumbens-area
17	28	Left-VentralDC
18	30	Left-vessel
19	31	Left-choroid-plexus
20	41	Right-Cerebral-White-Matter
21	43	Right-Lateral-Ventricle
22	44	Right-Inf-Lat-Vent
23	46	Right-Cerebellum-White-Matter
24	47	Right-Cerebellum-Cortex
25	49	Right-Thalamus-Proper
26	50	Right-Caudate
27	51	Right-Putamen
28	52	Right-Pallidum
29	53	Right-Hippocampus
30	54	Right-Amygdala
31	58	Right-Accumbens-area
32	60	Right-VentralDC
33	62	Right-vessel
34	63	Right-choroid-plexus
35	77	WM-hypointensities
36	85	Optic-Chiasm
37	251	CC_Posterior
38	252	CC_Mid_Posterior
39	253	CC_Central
40	254	CC_Mid_Anterior
41	255	CC_Anterior
42	1000	ctx-lh-unknown

order	label	StructName
43	1001	ctx-lh-bankssts
44	1002	ctx-lh-caudalanteriorcingulate
45	1003	ctx-lh-caudalmiddlefrontal
46	1005	ctx-lh-cuneus
47	1006	ctx-lh-entorhinal
48	1007	ctx-lh-fusiform
49	1008	ctx-lh-inferiorparietal
50	1009	ctx-lh-inferiortemporal
51	1010	ctx-lh-isthmuscingulate
52	1011	ctx-lh-lateraloccipital
53	1012	ctx-lh-lateralorbitofrontal
54	1013	ctx-lh-lingual
55	1014	ctx-lh-medialorbitofrontal
56	1015	ctx-lh-middletemporal
57	1016	ctx-lh-parahippocampal
58	1017	ctx-lh-paracentral
59	1018	ctx-lh-parsopercularis
60	1019	ctx-lh-parsorbitalis
61	1020	ctx-lh-parstriangularis
62	1021	ctx-lh-pericalcarine
63	1022	ctx-lh-postcentral
64	1023	ctx-lh-posteriorcingulate
65	1024	ctx-lh-precentral
66	1025	ctx-lh-precuneus
67	1026	ctx-lh-rostralanteriorcingulate
68	1027	ctx-lh-rostralmiddlefrontal
69	1028	ctx-lh-superiorfrontal
70	1029	ctx-lh-superiorparietal
71	1030	ctx-lh-superiortemporal
72	1031	ctx-lh-supramarginal
73	1032	ctx-lh-frontalpole
74	1033	ctx-lh-temporalpole
75	1034	ctx-lh-transversetemporal
76	1035	ctx-lh-insula
77	2000	ctx-rh-unknown
78	2001	ctx-rh-bankssts
79	2002	ctx-rh-caudalanteriorcingulate
80	2003	ctx-rh-caudalmiddlefrontal
81	2005	ctx-rh-cuneus
82	2006	ctx-rh-entorhinal
83	2007	ctx-rh-fusiform
84	2008	ctx-rh-inferiorparietal
85	2009	ctx-rh-inferiortemporal
86	2010	ctx-rh-isthmuscingulate
87	2011	ctx-rh-lateraloccipital

order	label	StructName
88	2012	ctx-rh-lateralorbitofrontal
89	2013	ctx-rh-lingual
90	2014	ctx-rh-medialorbitofrontal
91	2015	ctx-rh-middletemporal
92	2016	ctx-rh-parahippocampal
93	2017	ctx-rh-paracentral
94	2018	ctx-rh-parsopercularis
95	2019	ctx-rh-parsorbitalis
96	2020	ctx-rh-parstriangularis
97	2021	ctx-rh-pericalcarine
98	2022	ctx-rh-postcentral
99	2023	ctx-rh-posteriorcingulate
100	2024	ctx-rh-precentral
101	2025	ctx-rh-precuneus
102	2026	ctx-rh-rostralanteriorcingulate
103	2027	ctx-rh-rostralmiddlefrontal
104	2028	ctx-rh-superiorfrontal
105	2029	ctx-rh-superiorparietal
106	2030	ctx-rh-superiortemporal
107	2031	ctx-rh-supramarginal
108	2032	ctx-rh-frontalpole
109	2033	ctx-rh-temporalpole
110	2034	ctx-rh-transversetemporal
111	2035	ctx-rh-insula
112	3001	wm-lh-bankssts
113	3002	wm-lh-caudalanteriorcingulate
114	3003	wm-lh-caudalmiddlefrontal
115	3005	wm-lh-cuneus
116	3006	wm-lh-entorhinal
117	3007	wm-lh-fusiform
118	3008	wm-lh-inferiorparietal
119	3009	wm-lh-inferiortemporal
120	3010	wm-lh-isthmuscingulate
121	3011	wm-lh-lateraloccipital
122	3012	wm-lh-lateralorbitofrontal
123	3013	wm-lh-lingual
124	3014	wm-lh-medialorbitofrontal
125	3015	wm-lh-middletemporal
126	3016	wm-lh-parahippocampal
127	3017	wm-lh-paracentral
128	3018	wm-lh-parsopercularis
129	3019	wm-lh-parsorbitalis
130	3020	wm-lh-parstriangularis
131	3021	wm-lh-pericalcarine
132	3022	wm-lh-postcentral

order	label	StructName
133	3023	wm-lh-posteriorcingulate
134	3024	wm-lh-precentral
135	3025	wm-lh-precuneus
136	3026	wm-lh-rostralanteriorcingulate
137	3027	wm-lh-rostralmiddlefrontal
138	3028	wm-lh-superiorfrontal
139	3029	wm-lh-superiorparietal
140	3030	wm-lh-superiortemporal
141	3031	wm-lh-supramarginal
142	3032	wm-lh-frontalpole
143	3033	wm-lh-temporalpole
144	3034	wm-lh-transversetemporal
145	3035	wm-lh-insula
146	4001	wm-rh-bankssts
147	4002	wm-rh-caudalanteriorcingulate
148	4003	wm-rh-caudalmiddlefrontal
149	4005	wm-rh-cuneus
150	4006	wm-rh-entorhinal
151	4007	wm-rh-fusiform
152	4008	wm-rh-inferiorparietal
153	4009	wm-rh-inferiortemporal
154	4010	wm-rh-isthmuscingulate
155	4011	wm-rh-lateraloccipital
156	4012	wm-rh-lateralorbitofrontal
157	4013	wm-rh-lingual
158	4014	wm-rh-medialorbitofrontal
159	4015	wm-rh-middletemporal
160	4016	wm-rh-parahippocampal
161	4017	wm-rh-paracentral
162	4018	wm-rh-parsopercularis
163	4019	wm-rh-parsorbitalis
164	4020	wm-rh-parstriangularis
165	4021	wm-rh-pericalcarine
166	4022	wm-rh-postcentral
167	4023	wm-rh-posteriorcingulate
168	4024	wm-rh-precentral
169	4025	wm-rh-precuneus
170	4026	wm-rh-rostralanteriorcingulate
171	4027	wm-rh-rostralmiddlefrontal
172	4028	wm-rh-superiorfrontal
173	4029	wm-rh-superiorparietal
174	4030	wm-rh-superiortemporal
175	4031	wm-rh-supramarginal
176	4032	wm-rh-frontalpole
177	4033	wm-rh-temporalpole

order	label	StructName
178	4034	wm-rh-transversetemporal
179	4035	wm-rh-insula
180	5001	Left-UnsegmentedWhiteMatter
181	5002	Right-UnsegmentedWhiteMatter

B. DERIVING DIFFUSION KURTOSIS FROM DWI SIGNAL

The DKI approximation is a essentially a Taylor expansion (Maclaurin series) of $ln[S(\mathbf{n}, b)]$ in power of b, which is given as [274]:

$$ln\Big[\frac{S(\mathbf{n}, b)}{S_0}\Big] \approx -bD(\mathbf{n}) + \frac{1}{6}b^2\bar{D}^2 K(\mathbf{n})$$

where

$$D(\mathbf{n}) = \sum_{i,j=1}^{3} n_i n_j D_{ij}, \quad K(\mathbf{n}) = \frac{D^2}{D(\mathbf{n})^2} \sum_{i,j,k,l=1}^{3} n_i n_j n_k n_l W_{ijkl}$$

D_{ij} are the elements of the 3-dimension rank-2 diffusion tensor $\mathbf{D}$, and W_{ijkl} are the elements of the 3-dimension rank-4 kurtosis tensor $\mathbf{W}$. Both $\mathbf{D}$ and $\mathbf{W}$ are fully symmetric, and therefore the number of independent components are 6 and 15 respectively. In order to solve the signal attenuation equation, at least two nonzero b-values and 15 distinct gradient directions are required.

Subsequently, $\mathbf{W}$ can be orthogonally transformed by:

$$\tilde{W}_{ijkl} = \sum_{i',j',k',l'=1}^{3} R_{ii'} R_{jj'} R_{kk'} R_{ll'} W_{i'j'k'l'}$$

with $\tilde{W}_{ijkl}$ being the elements of $\mathbf{W}$ in the rotated frame R, in which R_{ij} is the j-th component of the eigenvector corresponding to λ_i in $\mathbf{D}$. Now, we can define:

$$\mathrm{K}_i = \frac{\mathrm{MD}^2}{\lambda_i^2}\tilde{W}_{iiii}$$

and compute axial (K_{ax}), radial ($\mathrm{K}_{\mathrm{rad}}$), and mean kurtosis ($\mathrm{K}_{\mathrm{mean}}$):

$$\mathrm{K}_{\mathrm{ax}} = \mathrm{K}_1, \quad \mathrm{K}_{\mathrm{rad}} = \frac{\mathrm{K}_2 + \mathrm{K}_3}{2}, \quad \mathrm{K}_{\mathrm{mean}} = \frac{\mathrm{K}_1 + \mathrm{K}_2 + \mathrm{K}_3}{3} = \frac{1}{n}\sum_{i=1}^{n} K(\mathbf{i}).$$

In order to obtain physically and biologically plausible estimates of diffusivity and kurtosis parameters, constraints need to be satisfied. See Tabesh et al. [279] for details.

C. USING DEEP LEARNING FRAMEWORK WITH BRAIN MRI FOR NEUROCOGNITIVE PREDICTION

A version of this Appendix is available in published form at:

Note that the numbering of references only corresponds to this Appendix, which is independent from the REFERENCE section of this thesis.

Cortical and Subcortical Contributions to Predicting Intelligence Using 3D ConvNets

Yukai Zou[1,2(✉)], Ikbeom Jang[3], Timothy G. Reese[4], Jinxia Yao[1],
Wenbin Zhu[4], and Joseph V. Rispoli[1,3,5]

[1]Weldon School of Biomedical Engineering, Purdue University, West Lafayette, USA
{zou75,yao150,jrispoli}@purdue.edu
[2]College of Veterinary Medicine, Purdue University, West Lafayette, USA
[3]School of Electrical and Computer Engineering, Purdue University,
West Lafayette, USA
jang69@purdue.edu
[4]Department of Statistics, Purdue University, West Lafayette, USA
{reese18,zhu633}@purdue.edu
[5]Institute of Inflammation, Immunology and Infectious Disease, Purdue University,
West Lafayette, USA

Abstract. We present a novel framework using 3D convolutional neural networks to predict residualized fluid intelligence scores in the MICCAI 2019 Adolescent Brain Cognitive Development Neurocognitive Prediction Challenge datasets. Using gray matter segmentations from T1weighted MRI volumes as inputs, our framework identified several cortical and subcortical brain regions where the predicted errors were lower than random guessing in the validation set (mean squared error = 71.5252), and our final outcomes (mean squared error = 70.5787 in the validation set, 92.7407 in the test set) were comprised of the median scores predicted from these regions.

Keywords: Adolescence · Brain · Convolutional neural networks · Fluid intelligence · MRI

1 Introduction

Unraveling puzzles between behavior and human brain has long been an intriguing topic in cognitive neuroscience [16]. One important research question is to understand how intelligence relates to brain structure in adolescence. There is evidence showing that fluid intelligence [2], the capacity of learning and adapting to novel situations, improves rapidly during late childhood (age 8–15) and is thought to be primarily influenced by neurobiological factors [1,12]. Derived from a collection of gold standard tests, the fluid intelligence scores are continuous values with normal distribution, thus posing a very interesting challenge in machine learning: can fluid intelligence be predicted from high dimensional features, such as brain morphometry?

Carrying this idea to a broader scientific community, a group of researchers at Stanford University, UC San Diego, Vanderbilt University, and Children's National Health System initiated the MICCAI 2019 ABCD Neurocognitive Prediction Challenge. Participating teams of the Challenge proposed algorithms that predict the residualized fluid intelligence scores using T1-weighted (T1w) MRI. The original fluid intelligence scores were residualized to remove confounding factors (brain volume, data collection site, and socio-demographic variables); the residualized scores and T1w brain images of 4,154 participants (3,739 for training set, 415 for validation set) were provided, whereas the scores of 4,515 participants (test set) were predicted from their images.

In neuroimaging, several machine learning methods have been proposed for predicting single continuous values from high feature dimensionality. Wang et al. [20] proposed a sparse learning framework using a Support Vector Regression model to predict the Intelligence Quotient from structural MRI; the framework reduced dimensionality by selecting the derived gray and white matter features, and by fusing different features, the multi-kernel model achieved better performance than the single-kernel model. In 2017, Cole et al. [3] first demonstrated that by applying 3D convolutional neural networks (ConvNets), the chronological age of healthy individuals can be reliably predicted based on T1w brain images that were only minimally processed, suggesting that 3D ConvNets have strengths in high-dimensional prediction tasks and discovering potential relationships between neuroimages and behavioral outcomes [14].

Inspired by the previous work, here we propose a novel framework for the intelligence prediction task on ABCD datasets, using 3D ConvNets trained on multiple cortical and subcortical brain regions. We hypothesize that under our framework, (1) certain brain regions can predict residualized fluid intelligence scores (a.k.a. predictive regions), and (2) compared to each predictive region, the median predicted scores from multiple predictive regions contribute to a lower mean squared error (MSE). Below we describe the methods and preliminary results in detail.

2 Materials and Methods

2.1 Dataset

The ABCD Study [10] is by far the largest multisite longitudinal study of brain development and child health in the United States. The Study has recruited over 11,500 children ages 9–10 at 21 sites across the country. In February 2018, the first annual curated ABCD data (Release 1.0) were made available on NIMH Data Archive (NDA), including minimally processed brain image volumes and tabulated results of structural MRI, diffusion MRI, and fMRI (both restingstate and task-based). Non-imaging assessments were also provided, including physical and mental health, neurocognition, substance use, biospecimens, as well as culture and environment domains.

The ABCD data used in this report came from Release 1.1. For the training set (3,739 participants) and validation set (415 participants), residualized fluid intelligence scores and processed T1w MRI were provided; for the test set (4,515 participants), only the images were provided. The fluid intelligence scores were collected in NIH Toolbox Neurocognition Battery [1]. The raw T1w brain images were acquired using a 3D T1w

inversion prepared RF-spoiled gradient echo scan (1mm isotropic), with prospective motion correction [19,21].

2.2 Processing

Fluid Intelligence Scores. The fluid intelligence scores were residualized using a linear regression model, with brain volume, data collection site, age at baseline, sex at birth, race/ethnicity, highest parental education, parental income, and parental marital status as independent variables. Any participant in the training or validation set with missing values in the dependent or independent variables was excluded. After model fitting, the residuals were computed for all the participants. The R code implementing the procedure has been made available on the official website (https://sibis.sri.com/abcd-np-challenge/).

T1-Weighted (T1w) MRI. A detailed documentation of MRI processing can be found in Pfefferbaum et al.'s Data Supplement [13]. First, the raw data were transformed into NIfTI formats [8], followed by noise removal, field inhomogeneity correction, and confined to a brain mask defined by non-rigidly aligning SRI24 atlas [15] to the T1w MRI. The brain mask was refined by a majority voting approach among the outputs of a variety of neuroimaging software. Based on the refined masks, inhomogeneity correction was repeated, and the skull-stripped T1w image was segmented into gray matter, white matter, and cerebrospinal fluid. Based on the SRI24/TZO parcellation map, the gray matter tissue was further parcellated after non-rigidly aligning the T1w image to the SRI24 atlas. Afterwards, skull-stripped T1w image and corresponding gray matter segmentations were affinely mapped to the SRI24 atlas, and the results were visually inspected.

2.3 3D ConvNets Framework

A schematic illustration of the 3D ConvNets framework is shown in Fig. 1. Due to memory constraints, we proposed this framework after the attempts of feeding the whole brain into the 3D ConvNet and training volumes of multiple brain regions in a simultaneous manner. First, the whole brain volume of size ($240 \times 240 \times 240$) was trimmed down to the specific size and location of each region of interest (ROI) according to the gray matter segmentations, as summarized in Table 1. The gray matter within each ROI was taken as input of 3D ConvNet. The ConvNet contains 3 repeated blocks of: a ($3 \times 3 \times 3$) convolutional layer (with stride of 1 and an L2 regularizer of 1×10^{-4}), a 3D batch-normalization layer [9], an ELU activation function, a ($2 \times 2 \times 2$) average pooling layer (with stride of 2), and a 3D dropout layer (rate of 0.4 for the first two blocks, 0.3 for the third) [18]. The number of feature channels for the three blocks were 8, 16, and 32 respectively. The total number of parameters for the three blocks were 224, 3,472, and 13,856 respectively. For the three ROIs (left triangular part of interior frontal gyrus, left caudate nucleus, and left thalamus) that were included for the final prediction scores, the number of parameters in the last fully connected layer were 6,913, 10,977, and 4,001 respectively. The predicted scores from these ROIs were concatenated to obtain the median predicted scores, which contributed to the final scores.
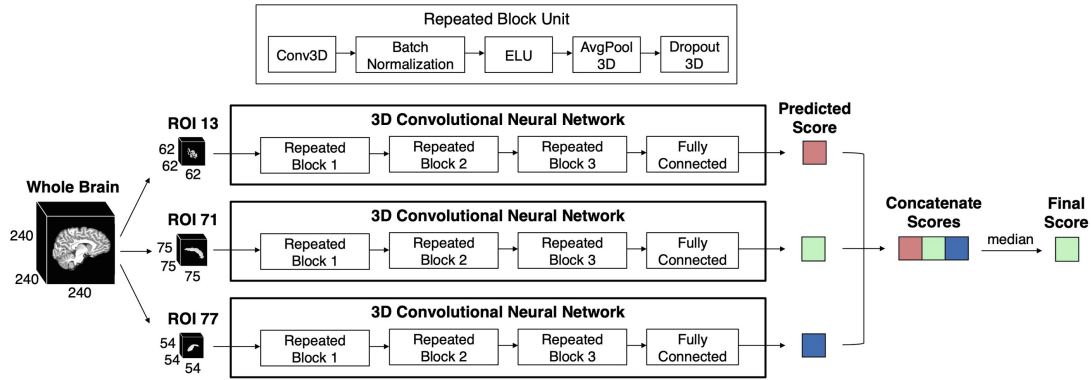
Fig. 1. Schematic illustration of the proposed 3D ConvNets framework. Only the three most predictive regions that contributed to the final submission are shown. ROI 13: left triangular part of interior frontal gyrus; ROI 71: left caudate; ROI 77: left thalamus.

2.4 Selected Brain Regions

We focused on the brain areas previously reported by Wang et al. [20] for estimating intelligence, including: bilateral transverse temporal gyri, bilateral thalamus (left is shown in Fig. 2), left parahippocampal gyrus, left hippocampus, right opercular part of inferior frontal gyrus, left anterior cingulate gyrus, right amygdala, left lingual gyrus, left superior parietal lobule, right inferior parietal lobule, left angular gyrus, left paracentral lobule, and left caudate nucleus (shown in Fig. 2). For those areas that were unilateral, we also explored their contralateral part. In addition, we explored bilateral triangular part of inferior frontal gyri (left is shown in Fig. 2). The full list of regions can be found in Table 1.

2.5 Implementation

During training, we formed batches by randomly sampling from the 3D volumes, with a batch size of 32. 3 epochs were chosen for training all the selected ROIs. The weights were trained by minimizing the MSE using the Adam optimizer [11], with a learning rate of 0.1 and constant decay of 5×10^{-5} after each epoch.

To determine ROIs that predict the scores in the validation set well, all the MSEs were compared to a "random guessing" model, which is essentially an MSE computed after assigning the mean of the residualized fluid intelligence score to each individual, and only those ROIs whose MSE was lower than the random guessing model were selected to compute the median predicted scores (final scores).

The 3D ConvNets were implemented using Keras library (v2.2.4) with Tensorflow (v1.12) as the backend in Python (v3.6) environment. The cluster consisted of 16 Intel Xeon processors, 196 GB system RAM, and two NVIDIA Tesla P100 GPUs (each with 16 GB memory). The GPUs were used independently to optimize the ConvNets; once the optimization was done, one GPU was used to evaluate the test set.

Table 1. Specific dimensions and locations of the selected brain regions in the SRI24 space [15]. L/R: left/right hemisphere.

| ROI	Brain Region	Dimensions	X		Y		Z	
			Min	Max	Min	Max	Min	Max
11	L Inferior frontal gyrus - opercular	65 × 65 × 65	41	101	105	165	102	162
12	R Inferior frontal gyrus - opercular	65 × 65 × 65	131	196	95	160	96	161
13	L Inferior frontal gyrus - triangular	62 × 62 × 62	40	102	127	189	100	162
14	R Inferior frontal gyrus - triangular	63 × 63 × 63	130	193	126	189	95	158
31	L Cingulate gyrus - anterior	83 × 83 × 83	51	134	113	196	89	172
32	R Cingulate gyrus - anterior	80 × 80 × 80	71	151	115	195	96	176
37	L Hippocampus	64 × 64 × 64	57	121	76	140	64	128
38	R Hippocampus	64 × 64 × 64	107	171	76	140	66	130
39	L Parahippocampal gyrus	83 × 83 × 83	40	123	74	157	35	118
40	R Parahippocampal gyrus	78 × 78 × 78	89	167	75	153	39	117
41	L Amygdala	41 × 41 × 41	78	119	105	146	76	117
42	R Amygdala	44 × 44 × 44	120	164	105	149	75	119
47	L Lingual gyrus	76 × 76 × 76	55	131	25	101	48	124
48	R Lingual gyrus	78 × 78 × 78	90	168	24	102	47	125
59	L Parietal lobule - superior	75 × 75 × 75	48	123	16	91	121	196
60	R Parietal lobule - superior	75 × 75 × 75	91	166	15	90	121	196
61	L Parietal lobule - inferior	56 × 56 × 56	49	105	47	103	122	178
62	R Parietal lobule - inferior	74 × 74 × 74	124	198	32	106	106	180
65	L Angular gyrus	68 × 68 × 68	40	108	19	87	104	172
66	R Angular gyrus	63 × 63 × 63	134	197	15	78	105	168
69	L Paracentral lobule	65 × 65 × 65	68	133	43	108	135	200
70	R Paracentral lobule	72 × 72 × 72	81	153	38	110	129	201
71	L Caudate nucleus	75 × 75 × 75	56	131	89	164	77	152
72	R Caudate nucleus	70 × 70 × 70	84	154	93	163	83	153
77	L Thalamus	54 × 54 × 54	74	128	81	135	88	142
78	R Thalamus	54 × 54 × 54	98	152	82	136	89	143
79	L Temporal gyrus - transverse	56 × 56 × 56	45	101	80	136	84	140
80	R Temporal gyrus - transverse	65 65 65	132	197	62	127	77	142
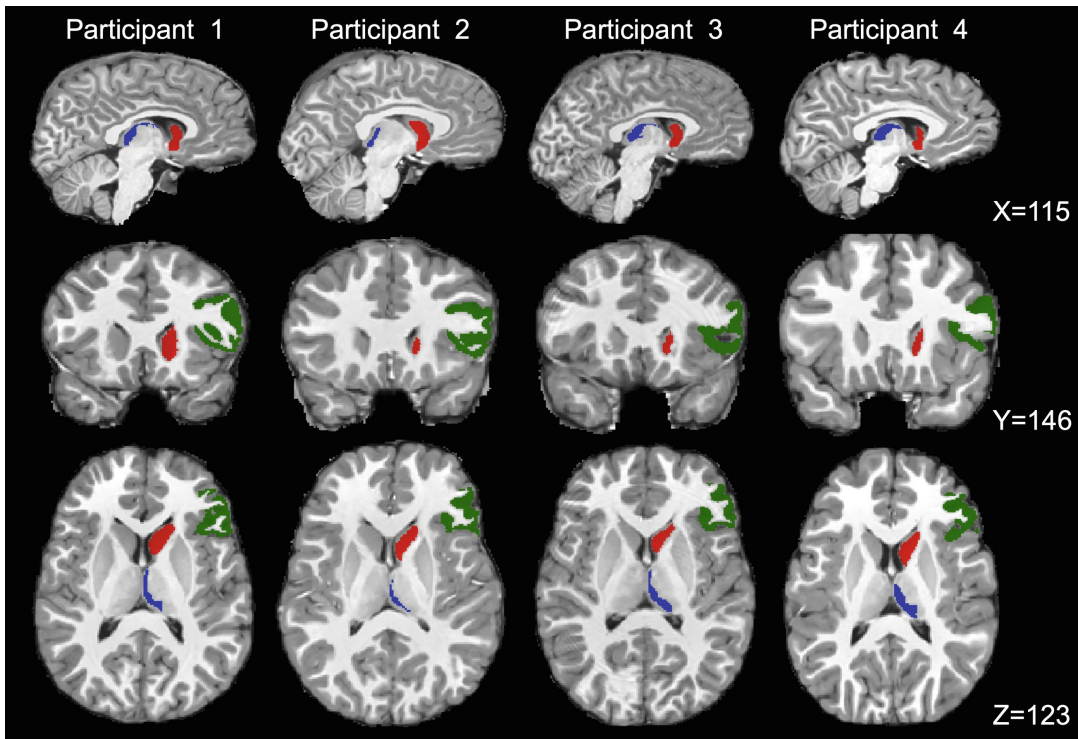
Fig. 2. Anatomical illustrations of the three most predictive ROIs among four participants. Red: left caudate nucleus (ROI 71); Green: left triangular part of interior frontal gyrus (ROI 13); Blue: left thalamus (ROI 77). (Color figure online)

3 Preliminary Results

Different number of epochs were tested, and 3 epochs were chosen for training the 28 selected brain regions (see Fig. 3). The total time used for training the 28 3D ConvNets was approximately 6 h.

For the validation set, the mean and standard deviation for the residualized fluid intelligence scores was -0.50 ± 8.47. The MSE of the random guessing model was 71.5252. Among all the prediction MSEs in validation, the three regions producing lower prediction error than the random guessing model were: left caudate nucleus (ROI 71) (MSE = 70.9454, $R^2 = 0.0451$), left triangular part of inferior frontal gyrus (ROI 13) (MSE = 71.1361, $R^2 = 0.0060$), and left thalamus (ROI 77) (MSE = 71.2036, $R^2 = 0.0068$). The median predicted scores resulted from these three ROIs produced a prediction error of 70.5787 ($R^2 = 0.0323$).

In addition, we observed that the right amygdala (ROI 42) produced a slightly lower prediction error (71.4737, $R^2 = 0.0029$) than the random guessing model, and we explored including it in our model; since the final prediction error did not improve (i.e., lower than 70.5787), we decided to exclude this ROI from our final model. The prediction errors in the validation set are summarized in Fig. 4. In the end, our proposed framework produced a prediction error of 92.7407 in the test set.
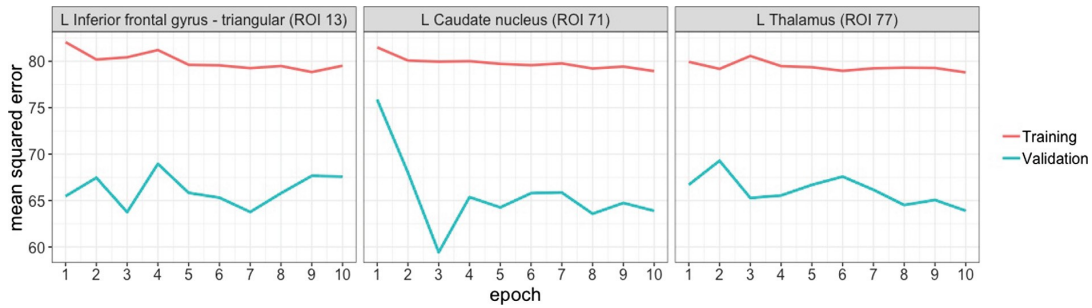
Fig. 3. Prediction errors during training (batch size=32). Results of ten epochs are shown. Left: left triangular part of inferior frontal gyrus (ROI 13); Center: left caudate nucleus (ROI 71); Right: left thalamus (ROI 77).
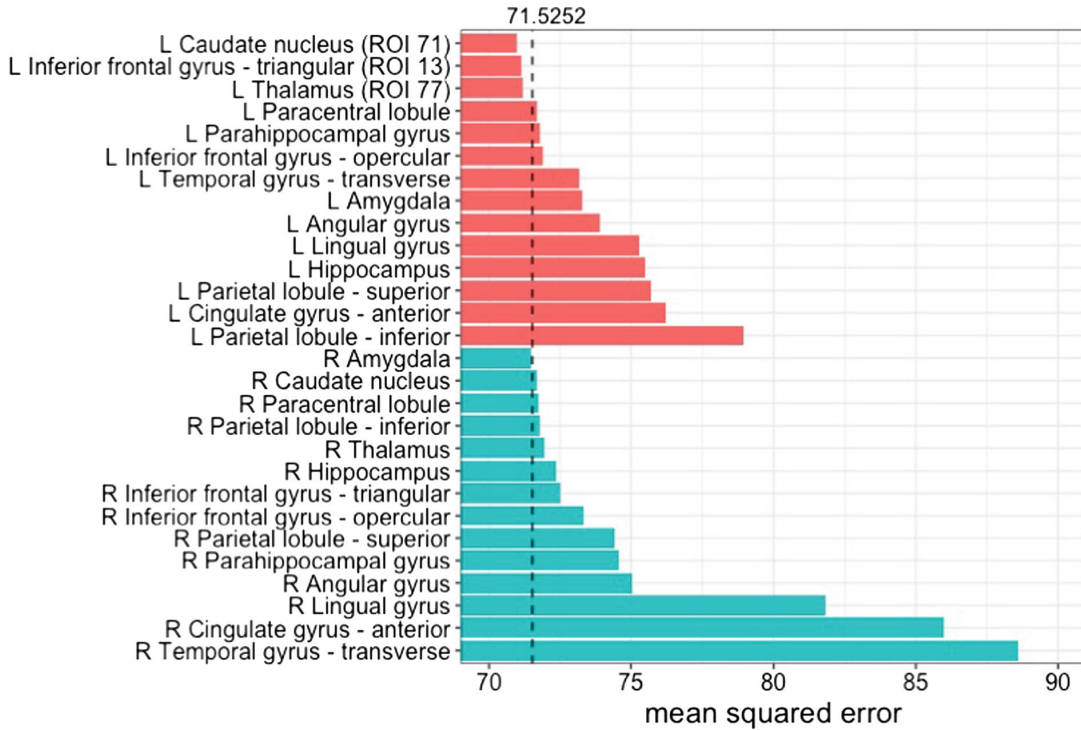

Fig. 4. Prediction errors of all the selected brain regions in the validation set, in comparison with the random guessing model (dashed line).

4 Discussion

Our proposed framework was inspired by previous work of [3] and [20]. The main idea of this framework is to take a holistic perspective of intelligence predictions obtained from multiple ROIs. Initially, we attempted to feed the whole brain into the 3D ConvNet, and we attempted to train volumes of multiple ROIs while adding a concatenating layer on the top to merge the features from each ROI; these attempts, however, failed due to the memory constraints. In addition, we observed overfitting occurred very early, which was the reason including regularizer and the dropout layer within each repeated block unit, as well as training all the models for 3 epochs only.

Overall, the proposed framework showed that the median predicted scores from the left triangular part of inferior frontal gyrus, left caudate nucleus, and left thalamus contributed to a better prediction performance, compared to both the random guessing

and to each region individually. Interestingly, the three ROIs all locate in the left hemisphere, and they have unique anatomical characteristics (see Fig. 2) and roles in cognitive functions. The triangular part of inferior frontal gyrus, also known as Brodmann area 45, is a cortical structure responsible for language processing [5]. Caudate nucleus is a subcortical structure and part of basal ganglia; it belongs to the corticostriatal circuitry and has many connections with frontal cortex and thalamus. This circuitry, particularly the caudate nucleus, contributes to goal-directed learning where the subject learns to recognize incentive perception to achieve a desirable outcome [7]. Thalamus is a subcortical structure located between the midbrain and cerebral cortex, with connections to many subcortical areas and the cerebral cortex. For a long time, thalamus was thought to be a hub that mainly relays information between different regions, but a recent study suggests that thalamus takes an active role in controlling functional cortical connectivity [17].

This research has several limitations. First, the SRI24 atlas [15] is derived from 24 participants spanning from late adolescence to late adulthood (age 19– 84). Considering that the ABCD participants are 9–10 years old, the extent of age-related changes in cortical and subcortical structures can lead to biased (sometimes even misclassified) parcellations [4]. This is the primary concern that led us to refrain from interpreting the potentially biased anatomical changes, and we strongly suggest normalizing T1w data to an age-appropriate brain atlas to reduce biases and improve interpretability [4,6]. Second, we did not examine and exclude potential outliers in the datasets; utilizing the brain tissue segmentation volumetrics [13] provided by the organizer may help the process. Nevertheless, the strength of ConvNets is that the features learnt and extracted from images are much richer than the features (e.g., brain tissue segmentation volumetrics) derived from processing pipelines. Therefore, providing raw (or minimally processed) T1w images would be beneficial in extracting anatomical features for high-dimensional prediction tasks, as is previously shown [3]. Third, we trained the 3D ConvNets only for a few selected brain regions, and it is worthwhile to fully utilize the gray matter segmentations and explore whether other brain regions contribute to intelligence prediction.

In conclusion, our proposed framework suggested several cortical and subcortical brain regions that contribute to a better prediction of residualized fluid intelligence scores, compared to random guessing. Our framework can be validated and improved in the future, and it offers a new and unique perspective for predicting fluid intelligence based on brain morphometry.

References

1. Akshoomoff, N., et al.: NIH toolbox cognition battery (CB): composite scores of crystallized, fluid, and overall cognition. Monographs of the Society for Research in Child Development (2013). https://doi.org/10.1111/mono.12038
2. Carroll, J.B.: Human Cognitive Abilities. Cambridge University Press, Cambridge(2009). https://doi.org/10.1017/cbo9780511571312
3. Cole, J.H., et al.: Predicting brain age with deep learning from raw imaging data results in a reliable and heritable biomarker. NeuroImage **163**, 115–124 (2017). https://doi.org/10.1016/j.neuroimage.2017.07.059
4. Dickie, D.A., et al.: Whole brain magnetic resonance image atlases: a systematic review of existing atlases and caveats for use in population imaging. Front. Neuroinformatics **11**, 1 (2017). https://doi.org/10.3389/fninf.2017.00001
5. Dronkers, N.F., Plaisant, O., Iba-Zizen, M.T., Cabanis, E.A.: Paul Broca's historic cases: high resolution MR imaging of the brains of Leborgne and Lelong. Brain **130**, 1432–1441 (2007). https://doi.org/10.1093/brain/awm042
6. Fonov, V., Evans, A.C., Botteron, K., Almli, C.R., McKinstry, R.C., Collins, D.L.: Unbiased average age-appropriate atlases for pediatric studies. NeuroImage **54**, 313–327 (2011). https://doi.org/10.1016/j.neuroimage.2010.07.033
7. Grahn, J.A., Parkinson, J.A., Owen, A.M.: The cognitive functions of the caudate nucleus. Prog. Neurobiol. **86**, 141–155 (2008). https://doi.org/10.1016/j.pneurobio. 2008.09.004
8. Hagler, D.J., et al.: Image processing and analysis methods for the adolescent brain cognitive development study. bioRxiv p. 457739 (2018). https://doi.org/10.1101/ 457739
9. Ioffe, S., Szegedy, C.: Batch normalization: accelerating deep network training by reducing internal covariate shift. arXiv e-prints arXiv:1502.03167 (2015)
10. Jernigan, T.: Introduction. Developmental Cognitive Neuroscience (2018). https:// doi.org/10.1016/j.dcn.2018.02.002
11. Kingma, D.P., Ba, J.L.: Adam: a method for stochastic gradient descent. In: ICLR: International Conference on Learning Representations (2015). https://arxiv.org/ pdf/1412.6980.pdf
12. Li, S.C., Lindenberger, U., Hommel, B., Aschersleben, G., Prinz, W., Baltes, P.B.: Transformations in the couplings among intellectual abilities and constituent cognitive processes across the life span. Psychol. Sci. **15**, 155–163 (2004). https://doi. org/10.1111/j.0956-7976.2004.01503003.x
13. Pfefferbaum, A., et al.: Altered brain developmental trajectories in adolescents after initiating drinking. Am. J. Psychiatry **175**, 370–380 (2018). https://doi.org/ 10.1176/appi.ajp.2017.17040469
14. Plis, S.M., et al.: Deep learning for neuroimaging: a validation study. Front. Neurosci. **8**, 229 (2014). https://doi.org/10.3389/fnins.2014.00229
15. Rohlfing, T., Zahr, N.M., Sullivan, E.V., Pfefferbaum, A.: The SRI24 multichannel atlas of normal adult human brain structure. Hum. Brain Mapp. **31**, 798–819 (2010). https://doi.org/10.1002/hbm.20906
16. Rushton, J.P., Ankney, C.D.: Brain size and cognitive ability: correlations with age, sex, social class, and race. Psychon. Bull. Rev. **3**, 21–36 (1996). https://doi. org/10.3758/BF03210739
17. Schmitt, L.I., Wimmer, R.D., Nakajima, M., Happ, M., Mofakham, S., Halassa, M.M.: Thalamic amplification of cortical connectivity sustains attentional control. Nature **545**, 219 (2017). https://doi.org/10.1038/nature22073

18. Srivastava, N., Hinton, G., Krizhevsky, A., Sutskever, I., Salakhutdinov, R.: Dropout: a simple way to prevent neural networks from overfitting. J. Mach. Learn. Res. **15**, 1929–1958 (2014)

19. Tisdall, M.D., Hess, A.T., Reuter, M., Meintjes, E.M., Fischl, B., Van Der Kouwe,A.J.: Volumetric navigators for prospective motion correction and selective reacquisition in neuroanatomical MRI. Magn. Reson. Med. **68**, 389–399 (2012). https://doi.org/10.1002/mrm.23228

20. Wang, L., Wee, C.Y., Suk, H.I., Tang, X., Shen, D.: MRI-based intelligence quotient(IQ) estimation with sparse learning. PLoS One **10**, e0117295 (2015). https://doi.org/10.1371/journal.pone.0117295

21. White, N., et al.: PROMO: real-time prospective motion correction in MRI usingimage-based tracking. Magn. Reson. Med. **63**, 91–105 (2010). https://doi.org/10.1002/mrm.22176

VITA

Yukai Zou
Curriculum Vitae

PERSONAL DETAILS

E-mail	yukaizou2012@gmail.com
LinkedIn	https://www.linkedin.com/in/yukaizou/
ResearchGate	https://www.researchgate.net/profile/Yukai_Zou2
Twitter	@YukaiZou

EDUCATION

Ph.D. Biomedical Engineering   Aug.2016 - Aug.2020
Purdue University, West Lafayette, IN, U.S.A.
    Dissertation: Developing Population-Specific Brain Atlases and Monitoring Repetitive Head Impacts for Early-to-Middle Adolescent Collision-Sport Athletes (Committee: Prof. Joseph Rispoli (PI), Prof. Riyi Shi, Prof. Thomas Talavage, Prof. Yunjie Tong
    Professional Grant Recipient, 2019
    Magoon Award for Excellence in Teaching, 2019
    Graduate Instructional Development Certificate, 2019
    Clinical and Translational Research Trainee at NIH, 2018
    Lynn Fellow, 2016

M.Sc. Biomedical Imaging   Sep.2014 - Sep.2015
UCSF, San Francisco, CA, U.S.A.
    Thesis: Microstructural integrity of brain white matter in different substance using populations: Diffusion Tensor Imaging analysis of 4 Tesla MRI data (Committee: Prof. Dieter Meyerhoff (PI), Prof. Pratik Mukherjee, Prof. Roland Henry, Prof. Nobert Schuff)

B.Sc. Applied Biology - Biotechnology (Minor in Sociology)   Sep.2009 - Feb.2014
Hong Kong Baptist University, Hong Kong, China
    Thesis: MicroRNAs Mediate Nicotinic Abuse through Activating Brain-Derived Neurotrophic Factor Pathway in Zebrafish (Committee: Prof. Ken Kin-Lam Yung (PI), Prof. Ricky Ngok-Shun Wong, Dr. Patrick Ying-Kit Yue)
    Exchange Student at Mercer University, U.S.A., Aug.2011-May.2012
    First Class Honor

RESEARCH EXPERIENCE

Graduate Research Assistant   Aug.2016 - Aug.2020
Weldon School of Biomedical Engineering, Purdue University, West Lafayette, IN, U.S.A.

- Operated 3T GE MRI scanner to collect neuroimaging data, and trained junior graduate students to become primary operators

- Processed and analysed data collected by Purdue Neurotrauma Group, performed neuroimaging database maintenance, and supervised research work of junior graduate students

- Prepared research data for publication and grant proposal, and submitted abstracts for international conferences to present the findings for community

Staff Research Associate   Oct.2015 - July.2016
Northern California Institute for Research and Education, San Francisco, CA, U.S.A.

- Performed neuroimaging database maintenance and data analysis of different substance using populations at San Francisco VA Medical Center

- Prepared research data for publication; wrote and published peer-reviewed manuscript

- Tested, troubleshooted, and streamlined pipelines for image processing and analysis

Graduate Research Assistant   Jun.2015 - Aug.2015
Department of Radiology, UCSF, San Francisco, CA, U.S.A.

- Learned neuroimaging data processing and analysis at San Francisco VA Medical Center

- Familiarized with in-house image processing pipelines, FSL toolbox, and R statistics software

- Investigated microstructural integrity of brain white matter within treatment-seeking alcoholics through retrospective analysis of diffusion and structural MRI datasets

Research Assistant   Apr.2014 - Aug.2014
Department of Biology, Hong Kong Baptist University, Hong Kong, China

- Collaborated on research projects in molecular neurosciences and biomedical engineering

- Trained undergraduate students and summer interns

- Performed laboratory maintenance and management

Student Research Assistant   May.2010 - July.2010
Department of Biology, Hong Kong Baptist University, Hong Kong, China

- Engaged in research at a molecular and cell biology laboratory under Summer Undergraduates Research Fellowship (SURF)

- Learned culturing Human Umbilical Vein Endothelial Cell for research work

- Evaluated the effects of ginsenosides on cytotoxicity and cell migration

PUBLICATIONS

[1] **Yukai Zou**, Taylor A. Lee, Roy J. Lycke, Ikbeom Jang, Nicole L. Vike, Diana O. Svaldi, Larry J. Leverenz, Thomas S. Redick, Eric A. Nauman, Thomas M. Talavage, Joseph V. Rispoli (2020), Prevent Post-Season Deficits: Monitoring White Matter Microstructure, Subconcussive Impacts, and Cognitive Performance Across a Single Season in American High School Football and Soccer Athletes. (in preparation)

[2] **Yukai Zou**, Wenbin Zhu, Ho-Ching Yang, Ikbeom Jang, Nicole L. Vike, Diana O. Svaldi, Trey E. Shenk, Victoria N. Poole, Gregory G. Tamer, Jr,, Larry J. Leverenz, Ulrike Dydak, Eric A. Nauman, Yunjie Tong, Thomas M. Talavage, Joseph V. Rispoli (2020), Development of brain atlases for early-to-middle adolescent collision-sport athletes. Scientific Reports. (in review)

[3] **Yukai Zou**, Ikbeom Jang, Timothy G. Reese, Jinxia Yao, Wenbin Zhu, Joseph V. Rispoli (2019), Cortical and Subcortical Contributions to Predicting Intelligence using 3D ConvNets. Lecture Notes in Computer Science, Vol. 11791: Adolescent Brain Cognitive Development Neurocognitive Prediction, Kilian M. Pohl, Wesley K. Thompson, Ehsan Adeli, Marius George Linguraru, eds., Cham, Springer International Publishing. `https://doi.org/10.1007/978-3-030-31901-4_21`

[4] Ikbeom Jang, Il Yong Chun, Jared R. Brosch, Sumra Bari, **Yukai Zou**, Brain R. Cummiskey, Taylor A. Lee, Roy J. Lycke, Victoria N. Poole, Trey E. Shenk, Diana O. Svaldi, Gregory G. Tamer, Jr., Ulrike Dydak, Larry J. Leverenz, Eric A. Nauman, Thomas M. Talavage (2019), Every Hit Matters: White Matter Diffusivity Changes in High School Football Athletes Are Correlated with Repetitive Head Acceleration Event Exposure. NeuroImage: Clinical. 24: 101930. `https://doi.org/10.1016/j.nicl.2019.101930`

[5] **Yukai Zou**, Donna E. Murray, Timothy C. Durazzo, Thomas P. Schmidt, Troy A. Murray, Dieter J. Meyerhoff (2018), White matter microstructural correlates of relapse in alcohol dependence, Psychiatry Research: Neuroimaging, 281:92-100. `https://doi.org/10.1016/j.pscychresns.2018.09.004`

[6] **Yukai Zou**, Donna E. Murray, Timothy C. Durazzo, Thomas P. Schmidt, Troy A. Murray, Dieter J. Meyerhoff (2017), Effects of abstinence and chronic cigarette smoking on white matter microstructure in alcohol dependence: diffusion tensor imaging at 4 Tesla, Drug and Alcohol Dependence, 175:42-50. `https://doi.org/10.1016/j.drugalcdep.2017.01.032`

[7] Yuqiang Fang, Catherine Y. Y. Iu, Cathy N. P. Lui, **Yukai Zou**, Carmen K. M. Fung, Hung Wing Li, Ning Xi, Ken K. L. Yung and King W. C. Lai (2014), Investigating dynamic structural and mechanical changes of neuroblastoma cells associated with glutamate-mediated neurodegeneration, Scientific Reports, 4: 7074. `https://doi.org/10.1038/srep07074`

[8] Qiuxian Peng, Qin Zhang, Wei Xiao, Meng Shao, Qin Fan, Hongwei Zhang, **Yukai Zou**, Xin Li, Wenxue Xu, Zhixian Mo, Hongbing Cai (2014), Protective effects of Sapindus mukorossi Gaertn against fatty liver disease induced by high fat diet in rats, Biochem Biophys Res Commun, 450(1):685-91.
`https://doi.org/10.1016/j.bbrc.2014.06.035`

CONFERENCE ABSTRACTS

[9] **Yukai Zou**, Wenbin Zhu, Ho-Ching Yang, Nicole L. Vike, Diana O. Svaldi, Trey E. Shenk, Victoria N. Poole, Gregory G. Tamer, Jr,, Larry J. Leverenz, Ulrike Dydak, Eric A. Nauman, Yunjie Tong, Thomas M. Talavage, Joseph V. Rispoli (2020), Development of an unbiased population-specific brain atlas for adolescent collision-sport athletes, 28th Intl. Soc. Mag. Res. Med. (ISMRM), Virtual Meeting. [Digital Poster]

[10] **Yukai Zou**, Wenbin Zhu, Ho-Ching Yang, Nicole L. Vike, Diana O. Svaldi, Trey E. Shenk, Victoria N. Poole, Gregory G. Tamer, Jr,, Larry J. Leverenz, Ulrike Dydak, Eric A. Nauman, Yunjie Tong, Thomas M. Talavage, Joseph V. Rispoli (2019), Unbiased population-specific brain templates for adolescent collision-sport athletes, 6th Indiana Neuroimaging Symposium, Indianapolis, IN, U.S.A. [**Data Blitz**]

[11] **Yukai Zou**, Wenbin Zhu, Ho-Ching Yang, Yu Zhu, Yunjie Tong, Thomas M. Talavage, Joseph V. Rispoli (2019), Construct a T1-weighted Brain Atlas for Adolescent Collision-sport Athletes with High-throughput High-performance Computing. Spring Reception of the Office of Interdisciplinary Graduate Program, West Lafayette, IN, U.S.A. [Multimedia E-poster]

[12] **Yukai Zou**, Taylor A. Lee, Roy J. Lycke, Ikbeom Jang, Nicole L. Vike, Eric A. Nauman, Thomas M. Talavage, Joseph V. Rispoli (2019), Head collisions and short-term white matter microstructural abnormalities in high school football athletes: how strong is strong enough? Greater Indiana SfN Annual Meeting, Indianapolis, IN, U.S.A. [Poster Presentation]

[13] Liesl Krause, Nicole Vike, **Yukai Zou**, Jana Vincent (2019), Increasing STEM Literacy Through Directed Outreach, 5th Annual Engagement and Service-Learning Summit, West Lafayette, IN, U.S.A. [Poster Presentation]

[14] **Yukai Zou**, Wenbin Zhu, Ho-Ching Yang, Yu Zhu, Yunjie Tong, Thomas M. Talavage, Joseph V. Rispoli (2019), Develop Population-specific Brain Atlas with High-throughput High-performance Computing. OHBM Annual Meeting, Rome, Italy. [Poster Presentation]

[15] Ho-Ching Yang, Jinxia Yao, James Wang, Nicole Vike, Pratik Kashyap, Sumra Bari, **Yukai Zou**, Ikbeom Jang, Jana Vincent, Taylor Lee, Xianglun Mao, Brianna Kish, Zhenhu Liang, Gregory Tamer, Eric Nauman, Thomas Talavage, Yunjie Tong (2019),

Characterizing Physiological Components of Near-Infrared Spectroscopy Signal Under Hypercapnia. OHBM Annual Meeting, Rome, Italy. [Poster Presentation]

[16] Ikbeom Jang, **Yukai Zou**, Thomas M. Talavage (2018), Automated Quality Assurance for Diffusion MR Images Using A Domain Transferred Deep Convolutional Neural Network, ISMRM Workshop on Machine Learning (Part II), Washington, DC, U.S.A. [Power Pitch; Poster Presentation]

[17] **Yukai Zou**, Taylor A. Lee, Roy J. Lycke, Ikbeom Jang, Nicole L. Vike, Eric A. Nauman, Thomas M. Talavage, Joseph V. Rispoli (2018), High-G head collisions are associated with short-term white matter microstructural deficits in high school football athletes, 3rd Joint Symposium of INS/NNS and AANS/CNS Section on Neurotrauma and Critical Care, Toronto, Ontario, Canada. [**Top 20 Finalist; Oral Blitz**]

[18] Thomas M. Talavage, Ikbeom Jang, **Yukai Zou**, Victoria N. Poole (2018), Long-term Changes in White Matter after Sports-Related Repetitive Head Impacts: an Across-Season DTI Study, 3rd Joint Symposium of INS/NNS and AANS/CNS Section on Neurotrauma and Critical Care, Toronto, Ontario, Canada. [Poster Presentation]

[19] **Yukai Zou**, Ikbeom Jang, Nicole L. Vike, Diana O. Svaldi, Larry J. Leverenz, Eric A. Nauman, Thomas M. Talavage, Joseph V. Rispoli (2017), White matter microstructural maturation in adolescent American Football athletes is affected by history of sport-participation and concussion, 26th Intl. Soc. Mag. Res. Med. (ISMRM), Paris, France. [Multimedia E-poster]

[20] Ikbeom Jang, Sumra Bari, **Yukai Zou**, Nicole L. Vike, Pratik Kashyap, Thomas M. Talavage (2017), Test-Retest and Between-Site Reliability in a Multisite Diffusion Tensor Imaging Study, 26th Intl. Soc. Mag. Res. Med. (ISMRM), Paris, France. [Multimedia E-poster]

[21] **Yukai Zou**, Ikbeom Jang, Nicole L. Vike, Thomas M. Talavage, Joseph V. Rispoli (2018), Brain white matter microstructural changes in high school athletes during one season of football competition. Spring Reception of the Office of Interdisciplinary Graduate Program, West Lafayette, IN, U.S.A. [Poster Presentation]

[22] **Yukai Zou**, Ikbeom Jang, Nicole L. Vike, Diana O. Svaldi, Larry J. Leverenz, Eric A. Nauman, Thomas M. Talavage, Joseph V. Rispoli (2018), Collision-sport participation and concussion history affects white matter maturation in adolescent athletes, Greater Indiana Society for Neuroscience Annual Meeting, West Lafayette, IN, U.S.A. [Poster Presentation]

[23] **Yukai Zou**, Ikbeom Jang, Nicole L. Vike, Thomas M. Talavage, Joseph V. Rispoli (2017), Acute Impacts of Football Competition on Brain White Matter Microstructure in High School Athletes. BMES Annual Meeting, Phoenix, AZ, U.S.A. [Poster Presentation]

[24] **Yukai Zou**, Ikbeom Jang, Nicole Vike, Victoria Poole, Trey Shenk, Diana Svaldi, Thomas Redick, Larry J. Leverenz, Eric A. Nauman, Thomas Talavage, and Joseph

Rispoli (2017), Abnormal White Matter Microstructure and Cognitions in Adolescent Athletes with Concussion History. BMES Annual Meeting, Phoenix, AZ, U.S.A. [Poster Presentation]

[25] **Yukai Zou**, Xianglun Mao, Ikbeom Jang, Nicole Vike, Diana Svaldi, Thomas Redick, Larry J. Leverenz, Eric A. Nauman, Thomas Talavage, and Joseph Rispoli (2017), Short and Long-term White Matter Microstructural Differences in Adolescent Female Soccer Athletes. BMES Annual Meeting, Phoenix, AZ, U.S.A. [Poster Presentation]

[26] **Yukai Zou**, Ikbeom Jang, Nicole L. Vike, Thomas S. Redick, Larry J. Leverenz, Eric A. Nauman, Thomas M. Talavage, Joseph V. Rispoli (2017), White matter microstructure in previously concussed adolescent athletes: implications on cognition. OHBM Annual Meeting, Vancouver, British Columbia, Canada. [Poster Presentation]

[27] **Yukai Zou**, Ikbeom Jang, Nicole L. Vike, Thomas S. Redick, Larry J. Leverenz, Eric A. Nauman, Thomas M. Talavage, Joseph V. Rispoli (2017), White matter microstructural abnormalities implicate cognitive impairments in adolescent athletes with concussion history. Spring Reception of the Office of Interdisciplinary Graduate Program, West Lafayette, IN, U.S.A. [Poster Presentation]

[28] **Yukai Zou**, Xianglun Mao, Ikbeom Jang, Nicole L. Vike, Thomas S. Redick, Thomas M. Talavage, Joseph V. Rispoli (2017), White Matter microstructure in adolescent female soccer athletes: diffusion MRI relations with years of high-school experience, concussion history, and cognitive measurements. Proc. 25th Intl. Soc. Mag. Res. Med. (ISMRM), Honolulu, HI, U.S.A. [Poster Presentation]

[29] Ikbeom Jang, **Yukai Zou**, Eric A. Nauman, Thomas M. Talavage, (2017), Diffusion Tensor Imaging Reveals Persistent Effects on White Matter Microstructure in High School Football Players with History of Sports-Related Concussion. Proc. 25th Intl. Soc. Mag. Res. Med. (ISMRM), Honolulu, HI, U.S.A. [Oral Presentation; Magna Cum Laude Award]

[30] Ikbeom Jang, Il-Yong Chun, Sumra Bari, **Yukai Zou**, Eric A. Nauman, Thomas M. Talavage, (2016), DTI Reveals Persistent Effects on White Matter in Football Players with History of Sports-Related Concussion. 4th Indiana Neuroimaging Symposium, Bloomington, IN, U.S.A. [Oral Presentation]

[31] **Yukai Zou**, Qiuxian Peng, Ken Kin-Lam Yung (2014), MicroRNAs Mediate Nicotinic Abuse through Activating Brain-Derived Neurotrophic Factor Pathway in Zebrafish, Physiology Symposium, Joint Scientific Conference of The Hong Kong Society of Neurosciences & The Biophysical Society of Hong Kong, University of Hong Kong. [Poster Presentation]

[32] Qiu-Xian Peng, Wei Liu, **Yu-Kai Zou**, Xu Han, Zhi-Xian Mo, Ken Kin-Lam Yung (2013), Magnolol against 6-Hydroxydopamine-Induced Loss of Tyrosine Hydroxylase Involves MAP Kinase Signaling Pathways in Transgenic Zebrafish and SH-SY5Y Cell

Models, Shenzhen - Hong Kong Joint Seminar on Alzheimer's Disease: Early Diagnosis, Prevention, and Mechanism, Shenzhen, China. [Oral Presentation]

ORAL PRESENTATIONS

[1] "Monitoring Brain Health of Adolescent Collision-Sport Athletes: Statistics in Neuroimaging," Statistics Graduate Student Seminar, College of Science, Purdue University, West Lafayette, IN, U.S.A. Apr 2, 2020.

[2] "Unbiased population-specific brain templates for adolescent collision-sport athletes," 6th Indiana Neuroimaging Symposium, Indianapolis, IN, U.S.A. Oct 28, 2019.

[3] "Cortical and Subcortical Contributions to Predicting Intelligence using 3D ConvNets," ABCD Neurocognitive Prediction Challenge, Medical Imaging Computing and Computer Assisted Intervention (MICCAI), Shenzhen, China, Oct 13, 2019.

[4] "High-G head collisions are associated with short-term white matter microstructural deficits in high school football athletes," Oral Blitz, 3rd Joint Symposium of INS/NNS and AANS/CNS Section on Neurotrauma and Critical Care, Toronto, ON, Canada, Aug 14, 2018.

[5] "Diffusion tensor imaging reveals perturbation of brain white matter maturation in high school football players," Summer Seminar, Weldon School of Biomedical Engineering, Purdue University, West Lafayette, IN, U.S.A., May 30, 2018.

[6] "Diffusion Tensor Imaging in Adolescent Athletes," Comparative Pathobiology and Basic Medical Science Graduate Seminar, College of Veterinary Medicine, Purdue University, West Lafayette, IN, U.S.A., March 8, 2018.

TEACHING EXPERIENCE

Purdue University   Aug.2017 - Dec.2018
Weldon School of Biomedical Engineering

- **Magoon Award for Excellence in Teaching**
  Recognized by College of Engineering
  Graduate Instructional Development Certificate
  Recognized by Teaching Academy and Center for Instructional Excellence

- **Teaching Assistant of:**
  BME 205 Biomolecular and Cellular Systems Lab (Fall 2018)
  BME 201 Biomolecules (Fall 2017)
  Activities:

Reviewed course materials and designed questions for assignments
Led lab sessions and assisting in-class discussions; held office hours for Q&A
Graded and evaluated completed assignments

Hong Kong Baptist University Sep.2013 - Nov.2013
Association of Mainland and Hong Kong Youths

- **Instructor of Cantonese Chinese**
  Taught oral speaking skills to freshman undergraduates from Mainland China

Mercer University Aug.2011 - May.2012
Academic Resource Center

- **Peer Tutor of Mandarin Chinese**
  Assisted undergraduates to improve listening, speaking, reading, and writing skills

SERVICE AND ENGAGEMENT

Senator, Graduate Student Government Aug.2018 - May.2020
Purdue University

- **Activities:**
  Participated in monthly meeting to review agenda and proposed bills
  Served as the liaison for Interdisciplinary Biomedical Sciences graduate program
  Served in Career Team to organize career fairs and professional development workshops
  Served in Grant Review and Allocation Team to review applications for conference travels,
  professional developments, graduate student organizations, and symposiums

Treasurer, Association for Magnetic Resonance Aug.2017 - July.2019
Purdue University

- **Graduate Student Organization Grant (Fall 2017, Fall 2018)**
  Awarded by Graduate Student Government
  Service Learning Grant (Spring 2018)
  Awarded by Office of Engagement

- **Activities:**
  Kept accounts, expenditures, and funds in a manner approved by the Business Office
  Prepared report to members, faculty advisor, and individuals upon request
  Worked with activities coordinator to provide budget
  Allocated travel award to support student member's conference activities

77777

Student Ambassador, International Office — Aug.2012 - Jan.2013
Hong Kong Baptist University

- **Activities:**
  Organized activities for International Office and Student Affairs
  Helped international students to adapt to Hong Kong
  Established connections with local entrepreneurs

Volunteer Worker, Wofoo Leader's Network — May.2011 - Jun.2011
Hong Kong Baptist University

- **Activities:**
  Volunteering service at rural areas in Yunnan, China
  Visited local families and organized student activities
  Taught lessons in basic sciences and geography

LEADERSHIP EXPERIENCE

Team Lead, Final Leaderboard Top 5 — Jan.2019 - Apr.2019
ABCD Neurocognitive Prediction Challenge, MICCAI
Developed a deep learning framework for predicting intelligence using imaging data

Graduate Mentor, Silver Award — Mar.2014 - Nov.2014
International Biomolecular Design Competition, Harvard University
Designed and fabricated a DNA origami-based therapeutic agent for cancer cells

Team Lead, Silver Award — Mar.2013 - Nov.2013
International Biomolecular Design Competition, Harvard University
Demonstrated a DNA origami-based biosensor for detecting amyloid-beta aggregation

Team Lead, Champion — Jan.2013
Century Club Youth Scientist Challenge Cup, Hong Kong Baptist University
Proposed a smart device for food safety assurance

Vice President — Apr.2010 - Apr.2011
Mandarin Chinese Debate Team, Hong Kong Baptist University
First Runner-up, Hong Kong 2010 Nine-University Debate Competition

HONORS AND AWARDS

2020	Trainee (Educational) Stipend Award, ISMRM
2019	Professional Grant, Purdue Graduate Student Government
2019	Travel Grant, Purdue Institute for Integrative Neuroscience
2019	Travel Grant, Purdue Graduate Student Government
2019	Magoon Award for Excellence in Teaching
2018	Joe Bourland Travel Award, Purdue University
2018	Trainee (Educational) Stipend Award, ISMRM
2017	Trainee (Educational) Stipend Award, ISMRM
2017	Travel Grant, Purdue Institute for Integrative Neuroscience
2016	Lynn Fellowship, Purdue University
2014	Talent Development Scholarship, Hong Kong Government
2013	President's Honor Roll, HKBU
2012	Dean's List, Mercer University
2011	President's Honor Roll, HKBU
2010	Summer Undergraduate Research Fellowship, HKBU